Title

Resolving lipid and peptide regulators of the noxious heat and pain receptor TRPV1

Permalink

https://escholarship.org/uc/item/0vs8d9r6

Author

Mancino, Adamo Samuele

Publication Date

2024

Peer reviewed|Thesis/dissertation

Resolving lipid and peptide regulators of the noxious heat and pain receptor TRPV1
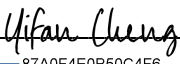
by
Adamo Mancino

DISSERTATION
Submitted in partial satisfaction of the requirements for degree of
DOCTOR OF PHILOSOPHY

in

Biophysics

in the

GRADUATE DIVISION
of the
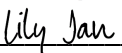UNIVERSITY OF CALIFORNIA, SAN FRANCISCO

Approved:

DocuSigned by:

Yifan Cheng
87A0F4E0B50C4F6...

Yifan Cheng

Chair

DocuSigned by:

David Julius
DocuSigned by 45C...

David Julius

Robert Stroud
DocuSigned by 413...

Robert Stroud

Lily Jan
394456D87457494...

Lily Jan

_____
Committee Members

ACKNOWLEDGEMENTS

The work presented in this dissertation was no lone effort. I came to UCSF with a background in neuroscience and electrophysiology. I had never purified a protein before in my life, let alone operated an electron microscope. Yet those skills are now second nature to me. I even wrote up something of a thesis while I was at it.

None of this would have been possible without the vast input I was fortunate to receive from all former and current members of the Cheng and Julius labs. You are such a motivated, bright, and talented bunch. You inspired me to join your team and taught me everything I know. While you all had your impact on me in some way, rest assured, I would especially like to recognize the many mentors who helped me navigate my doctoral studies – thank you, Daniel, Melinda, Jianhua, Zanlin, Wooyoung, MJ, Lin, Wendy, Raghav, Marcell, Kevin, David B., Glenn, and Li. I would also like to give special thanks to Will, the symbolic second author of this dissertation. You invited me with open arms to participate in all your projects, and working alongside you at the rig remains a highlight of my time at UCSF. Moreover, I sincerely appreciate all the guidance I received from my thesis committee – Yifan Cheng, David Julius, Bob Stroud, and Lily Jan.

I would never have pursued doctoral studies if not for the positive scientific role models I had along the way. I am especially incredibly grateful for my former colleagues from a lifetime ago in the Bowie and Sjöström labs – Ryan, Erik, Amanda, Edward, Martina, Marika, Patricia, Mark, Sandra, and Sally. You all set the bar for what a graduate student should aspire to be, and I never lost sight of your examples. In a similar vein, I would also like to acknowledge the continued support of my former professors – Per Jesper Sjöström and Derek Bowie.

Having a passion for science is essential to completing a doctorate. But you know what

goes even further? Having endless support from my family and friends back in my hometown of Montreal, cheering me on as the finish line edged ever closer. My siblings – Alicia, Alessandro, and Armando. My lifelong friends – Madalena, Jessica, Conor, Syim, and Tania. My beloved Nonna Ida and all my aunts, uncles, and cousins. My hiking companions – Max, Kath, and Victor (how I wish you were still here). My nephew and godson, Davide. By the time you can read and understand this dissertation, most of the science will probably be obsolete. Still, I hope it will spark your curiosity about the incredible world you have joined. My loving parents, Elena and Sam. You inspired me to keep pushing my limits and supported me in all my endeavors without hesitation. I would never have been able to make this monumental leap without you.

Five years in graduate school in a foreign country and on the backdrop of a global pandemic… let us say that it was not without its challenges. I am forever indebted to my support network here in the Bay Area – Wilson, Daphne, Wenqi, Christian, Maxine, Yifei, Estelle, and Nathan. And, of course, thank you, Jhovan. Though thousands of miles away from both our home countries, I never felt more at home in San Francisco than in your company.

To everyone – this degree is as much mine as it is yours, as I could not have gone this far without you. Now, onto the thesis! It might not amount to much. Still, I hope that it makes you proud all the same!

CONTRIBUTIONS

This dissertation, particularly Chapter 1, reproduces the content of one published manuscript. Its citation and author contributions are as follows:

W.R.A. conceived the project, performed cryo-EM experiments and analyzed data. A.M. performed and analyzed the electrophysiology experiments. F.R.M synthesized the brominated phosphoinositide lipids under the guidance of A.F. Y.C. and D.J. provided advice and guidance throughout. All authors contributed to manuscript preparation.

RESOLVING LIPID AND PEPTIDE REGULATORS OF THE NOXIOUS HEAT AND

PAIN RECEPTOR TRPV1

ADAMO SAMUELE MANCINO

ABSTRACT

The TRPV1 ion channel serves a critical role in sensory nerve fibers as an integrator of various painful stimuli, including noxious heat, vanilloid compounds, acids, and toxins from venomous creatures. Targeting TRPV1 has shown promising therapeutic potential, as both agonists and antagonists alike are being explored to treat pain across a variety of chronic conditions. A deeper understanding of TRPV1's activity at both structural and functional levels is essential to advancing drug discovery, which can ultimately lead to improved clinical outcomes. The two chapters of this dissertation will address fundamental, yet unresolved, questions in TRPV1 pharmacology.

For one, the precise mechanism by which lipids modulate channel activity continues to be debated. Natural products like capsaicin and resiniferatoxin are known to bind to a site within the channel known as the vanilloid binding pocket. In the absence of applied ligand, this pocket is instead occupied by a resident phosphoinositide lipid. Competition for the vanilloid binding pocket is clearly recognized as a key aspect of ligand action. Removal of this resident lipid has been speculated to underlie temperature-dependent gating as well, however this has yet to be definitively demonstrated. Moreover, the vanilloid binding pocket appears capable of accommodating other lipidic species. This includes phosphatidylinositol 4,5-bisphosphate (PIP_2), which is crucial in cellular signaling mechanisms. Despite this, the effects of PIP_2 on TRPV1 remain controversial. In Chapter 1, we investigate how both the resident lipid, along with PIP_2 and its derivatives, influence TRPV1 channel gating.

Meanwhile, venoms from tarantulas, scorpions, and other venomous species are a rich source of pharmacological agents targeting TRPV1. However, the discovery of new ligands is often complicated by the heterogeneous nature of venoms. While venoms contain specialized toxin peptides that exquisitely target key host proteins, like TRPV1, they often comprise a variety of toxins and other signaling molecules. Specific toxins can be identified through mass spectrometry of separated venom components or by sequencing nucleic acids from the animal's venom glands. While effective, these methods are resource-intensive and do not readily provide insight into the structural activity of identified toxins. In Chapter 2, we introduce a novel pipeline rooted in cryo-electron microscopy (cryo-EM) to facilitate TRPV1 toxin discovery out of crude venoms and elucidate mechanisms of action.

TABLE OF CONTENTS

LIST OF FIGURES

LIST OF TABLES

xiii

LIST OF ABBREVIATIONS

AP   Action potential

ARD   Ankyrin repeat domain

C. lividus   Cyriopagopus lividus

Cap   Capsaicin

CNS   Central nervous system

Cpz   Capsazepine

Cryo-EM   Cryogenic electron microscopy

CTD   C-terminal domain

DDM   n-dodecyl-β-D-maltopyranoside

dFSC   Directional Fourier shell correlation

DkTx   Double-knot toxin

DOPC   1,2-dioleoyl-sn-glycero-3-phosphocholine

EC50   Half maximal effective concentration

EPSP   Excitatory post-synaptic potential

HPETE   Hydroperoxyeicosatetraenoic acid

ICK   Inhibitory cystine knot

IPSP   Inhibitory post-synaptic potential

LPA   Lysophosphatidic acid

MBP   Maltose-binding protein

MPD   Membrane proximal domain

NADA   N-arachidonoyl-dopamine

PI   Phosphatidylinositol

PIP$_2$ or PI(4,5)P$_2$	Phosphatidylinositol 4,5-bisphosphate
PNS	Peripheral nervous system
POPG	1-palmitoyl-2-oleoyl-sn-glycero-3-phospho-(1'-rac-glycerol)
RTX	Resiniferatoxin
SEM	Standard error of the mean
TCEP	Tris(2-carboxyethyl) phosphine
TEV	Tobacco etch virus
TRP	Transient receptor potential
TRPV1	Transient receptor potential vanilloid subtype 1
UCSF	University of California, San Francisco
VBP	Vanilloid binding pocket
VR1	Vanilloid receptor subtype 1

LITERATURE REVIEW

Ion Channels and Their Role in the Nervous System

The nervous system is a vastly complex part of the body, essential for our ability to detect and process stimuli from the surrounding environment, and then to initiate actions in response. It can be divided into two sub-systems – the central nervous system (CNS), which includes our brain and spinal cord, and the peripheral nervous system (PNS), which makes up all the nerves that innervate the extremities of our body. The fundamental cellular building block of the nervous system, responsible for relaying information from the PNS to the CNS and back, is the neuron. It achieves this function by generating highly orchestrated electrical signals – some of which are graded and are allowed to summate on the input side, like excitatory postsynaptic potentials (EPSPs) and inhibitory postsynaptic potentials (IPSPs), whereas some are all-or-none responses designed for faithful transmission, as is the case of action potentials (APs)[1,2].

These signals can be generated due to two key properties of neurons. Firstly, there exist differences in ionic concentrations across the plasma membrane that set up electrochemical gradients. There are vastly more sodium and calcium ions outside the cell than inside, and for potassium the opposite holds, that there are more potassium ions inside the cell than outside. This occurs by design, as transporters actively pump ions so as to maintain this asymmetry. Secondly, there exist molecules in the membranes of neurons that collapse these gradients. This movement of ions has the consequence of changing the membrane potential of the neuron, giving rise to those aforementioned signals like EPSPs, IPSPs, and APs. These particular molecules are known as ion channels[1,2].

Ion channels make up a huge superfamily of proteins, numbering in the hundreds. All members serve a similar purpose, in that they act like molecular switches. They adopt, at any

given moment, one of two important functional states: 1) opened and permeable to ions or 2) closed and impermeable to ions. Within this superfamily, the voltage-gated ion channels and their relatives make up the largest family, totaling together about 143 genes in humans. All members of this family share a similar overall architecture. At the very minimum, each features a major pore-forming component, but sometimes they can be decorated with other auxiliary proteins. The pore-forming core is typically subdivided into four four-fold symmetric subunits. These four subunits typically originate from discrete polypeptide chains, but in some channels can come from one continuous amino acid stretch. Each subunit can be further dissected into three parts – a transmembrane domain, an extracellular domain, and an intracellular domain. The transmembrane domain is highly organized and is comprised of six α-helices, denoted S1 through S6, that span across the membrane. These can be further grouped into two parts: where S5 and S6 are closer to the central pore that serves ion permeation, and S1 through S4 form a bundle staggered around the pore. The extracellular domain is more restricted and consists of the loops that connect between S1-S2, S3-S4, and S5-S6. The intracellular domain is far more extensive. In addition to those other loops between S2-S3 and S4-S5, it includes the N- and C-termini, which vary wildly in size and organization from one channel to another. All four subunits come together to create an aqueous pore in an otherwise hydrophobic environment. The pore is highly stereotyped and has two major constriction points, both of which can be regulated to allow or prohibit ion permeation. Towards the extracellular side, the S5-S6 linkers come together to establish the selectivity filter, also called the upper gate. In addition to gating ion passage, the selectivity filter can discriminate the identity of the ions passing through, for example making a channel selective for sodium or non-selective to any cation. Towards the cytoplasmic side, the S6 helices define the lower gate.[3,4]

Despite having similar overall shape, the members that make up the voltage-gated channel family are all designed somewhat differently. This allows them to achieve their unique functions. One major factor that differentiates them is the stimulus required for each channel to open. Some channels respond primarily to changes in membrane potential, others to specific chemical ligands, some to changes in temperature, others to pressure, or some to a combination of all factors listed above, and some are quite simply open all the time. By having the appropriate ion channel in the appropriate neuron, the nervous system can detect the appropriate stimulus from internal and external environments and, if need be, can elicit the appropriate response. In this way, ion channels have the ability to transform simple input stimuli into more complex organismal behavior.[1–3]

TRPV1, the Noxious Heat and Pain Receptor

Transient receptor potential (TRP) channels form of a large division of the voltage-gated ion channel family. TRP channels can be further categorized into six subfamilies – TRPV, TRPC, TRPM, TRPML, TRPP, and TRPA channels. Broadly speaking, all TRP channels follow a morphology similar to what was described earlier, however each TRP subfamily has its own unique structural properties. The TRPV family, in particular, is grouped together by its ability to respond to vanilloid compounds or else by homology to said receptors. In its strictest definition, vanilloids are molecules that contain a vanillyl moiety, but have grown to encompass all ligands that act on TRPV channels. They are ubiquitous in natural products as exogenous vanilloids (i.e. exovanilloids) and were key to identifying the first mammalian TRPV channels. Endogenous vanilloids (i.e. endovanilloids), by definition, are sourced from within the human body and have been confirmed to exist in the years following the initial discovery of TRPV channels.[5]

TRPV1 was the first TRPV channel identified. It was discovered by the Julius lab out of a cDNA library generated from neurons in the dorsal root ganglion. The cloned receptor, at the time dubbed vanilloid receptor subtype 1 (VR1), was shown to activate in response to two vanilloids compounds: 1) capsaicin, found ubiquitously in chili peppers, and 2) resiniferatoxin (RTX), derived from resin spurge. It was also shown to generate current in response to temperatures exceeding 40°C. Curiously, the fact that the same labelled line becomes activated for both high temperature and capsaicin is the reason why chili peppers produce a "hot" taste sensation. Furthermore, its ligand-induced activity was found to be potentiated by acidity, as low as pH 6.3. TRPV1 was determined to be cation-non-selective, meaning it can flux both monovalent cations, like sodium and potassium, as well as divalent cations, particularly calcium. This allows it to signal via two intracellular mechanisms, through depolarization and calcium-dependent signaling cascades[6].

From this initial study, it was clear that TRPV1 was designed to respond to painful stimuli, but its role in nociception had yet to be confirmed. Tissue immunohistochemistry efforts localized TRPV1 primarily to small diameter, unmyelinated primary afferents – also called C fibers – which are typically associated with nociceptive pathways[7,8]. Activation of these fibers was found to release proinflammatory and proalgesic factors, like neurotrophins, bioactive lipids, protons, proteases, and monoamines, thereby tying TRPV1 to neurogenic inflammation[9]. Knockouts of the TRPV1 gene were associated with eliminated responses to exovanilloids, impaired detection of painful heat, and loss of thermal hypersensitivity during inflammation, though responses to noxious mechanical stimuli remained intact[10]. A second genetic ablation study concluded similarly, as mutant mice lacking TRPV1 still responded to painful stimuli but failed to develop pharmacologically-induced thermal hypersensitivity[11]. These experiments

cemented TRPV1 as the body's noxious heat and pain receptor, a role which it is now recognized to share with other ion channels.

Since the discovery of TRPV1 as the receptor for vanilloids, the list of ligands found to act on the channel has continued to grow. The first endovanilloid identified was the endocannabinoid anandamide. Anandamide was implicated in the vasodilation of blood vessels in a manner that was not actually cannabinoid receptor-dependent, but rather TRPV1-dependent. Follow-up work demonstrated that anandamide could elicit TRPV1 activity in heterologous systems, illustrating a direct effect on the channel[12]. Following the discovery of anandamide, other metabolites of its parent molecule arachidonic acid were found to activate TRPV1, including N-arachidonoyl-dopamine (i.e. NADA)[13] and 12-(S)- and 15-(S)-hydroperoxyeicosatetraenoic acid (i.e. 12S- and 15S-HPETE)[14]. The next group of molecules shown to interact with TRPV1 were phospholipids. In particular, the signaling molecule phosphatidylinositol 4,5-bisphosphate (i.e. $PI(4,5)P_2$ or PIP_2) was suggested to inhibit TRPV1, given that depletion of PIP_2 by phospholipase C and by antibody sequestration seemed to boost agonist-evoked TRPV1 currents[15]. Follow-up work has since argued that PIP_2 may actually potentiate TRPV1 activity[16] (and a possible explanation for this discrepancy will be addressed in more detail in Chapter 1 Part 2). Beyond PIP_2, it was shown that other phospholipids, for instance phosphatidylinositol (PI) and phosphatidylinositol-4-phosphate (PI_4P), could play similar inhibitory roles, in keeping with the idea that phospholipids generally maintain the channel stable in its resting state[17]. Later, the single-chained fatty acid lysophosphatidic acid (LPA), long implicated in pain signaling, was shown to have direct agonist action on TRPV1 as well[18].

While the early agonists identified were lipidic in nature, a series of inhibitory cystine

knot (ICK) peptide toxins were eventually isolated from tarantula venom that could also activate TRPV1. These became known as the vanillotoxins and were denoted VaTx1, VaTx2, and VaTx3[19]. A few years later, another form of vanillotoxin was discovered with even higher affinity for TRPV1. This property stemmed from its bivalent nature, as it was the fusion of two monovalent ICK toxins. This became known as double-knot toxin (DkTx)[20]. All these discoveries continued to paint TRPV1 as a highly polymodal receptor, capable of integrating very many stimuli – both thermal and chemical, either lipidic or peptidic in composition, and from endogenous and exogenous sources alike.

Structural Basis for TRPV1 Gating

From the cloned sequence of TRPV1, a topology model could be built and annotated (**Fig 0.1).** Similar to what we discussed earlier for voltage-gated channels in general, TRPV1 comes together as a homotetramer. Each monomer is nearly 840 amino acids in length and can be further organized into an N-terminal region, a transmembrane domain, and a C-terminal region. At the far N-terminus, six ankyrin repeats make up the ankyrin repeat domain (ARD). Between the ARD and the start of first transmembrane helix (S1) is the membrane proximal domain (MPD), which consists of the linker domain and the pre-S1 helix. The transmembrane domain consists of six transmembrane α-helices – S1 through S4 make up the voltage sensor-like domain (VSLD), whereas S5 and S6 constitute the pore domain. The extracellular linker between S5 and S6 is called the pore loop and it contains a small α-helical stretch called the pore helix. The C-terminus, compared to the N-terminus, is smaller and consists of the TRP domain immediately downstream of S6, followed then by the C-terminal domain (CTD).[21]

From the discovery of TRPV1 and its various inputs, subsequent work focused on

determining the molecular details of how TRPV1 was receptive to its many stimuli. Initial studies took advantage of the observation that the effects of certain agonists on TRPV1 were often species-dependent. Capsaicin could be used to elicit responses in human and rodent TRPV1 orthologues, but not in avian TRPV1. Exploiting this with chimeras, combined with electrophysiology and radio-ligand binding assays, it was possible to narrow down that capsaicin likely interacted with several residues between the S2 and S4 transmembrane segments, a site which became known as the vanilloid binding pocket (VBP). The same site was simultaneously identified for anandamide.[22] Subsequent publications using similar strategies corroborated the initial findings and extended them to RTX[23,24]. As for the vanillotoxins, a similar comparative species analysis revealed that frog TRPV1 was insensitive to DkTx and VaTx3. Mutagenesis and electrophysiology experiments confirmed that mutation of one residue in the S5-S6 linker could ablate DkTx responses selectively, demonstrating that vanillotoxins were likely targeting the outer pore loops[20]. Meanwhile for protons, it was clear that acidic solution could potentiate TRPV1 currents only in outside-out patches, not inside-out ones, therefore limiting the likely interaction sites to just the extracellular loops[7]. From there, it was possible to identify specific acidic residues that, when mutated, could abrogate pH-sensing altogether[25].

These ligand binding sites, first identified with functional experiments, were ultimately confirmed and fully mapped out in detail when the first full-length structures of TRPV1 were solved. Curiously, this was a watershed moment in the field of structural biology and ushered in what is now known as the "resolution revolution" enabled by cryogenic electron microscopy (cryo-EM)[26]. The first structures captured TRPV1 in its unliganded state[21] as well as its agonist-bound states[27,28]. A comparison of the different conditions revealed additional density for the vanilloids RTX and capsaicin in the VBP, which could now be visually delineated by helices S3

7

and S4 plus the S4-S5 linker of one monomer along with S6 from the adjacent monomer. Likewise, peptide density corresponding to DkTx could be seen interacting with the extracellular surface of TRPV1 adjacent to the pore helix. The vanilloids and vanillotoxins appeared to have additive effects on the permeation pathway, in that the former would tug at the S4-S5 linker to open the lower gate whereas the latter would displace the pore helices to pry open the selectivity filter. Together, these conformational changes could expand the central pore large enough to conduct ions[27]. A later study captured structures of TRPV1 exposed to pH 6. Protonation of the two glutamate residues known to be involved in acid-sensing appeared to break key salt bridges and hydrogen bond networks towards the extracellular side of TRPV1. This had the effect of reliving the constriction on the upper gate, which would translate to potentiated channel activity[29]. From even more recent structural work, it was further established that the VBP can accommodate other lipidic species, including PI, PIP_2, and LPA[30].

The molecular determinants of heat activation of TRPV1, in contrast to ligand binding, are much less clearly defined. It is clear that temperature sensitivity is intrinsic to the channel itself and not a product of its interaction with intracellular components, because it is possible to record heat-evoked currents from purified TRPV1 that is reconstituted into proteoliposomes[17]. However, in trying to determine precisely what subregion of TRPV1 confers heat sensitivity, it seems to be that many parts of the channel are implicated in the process. The intracellular bulk of TRPV1 receives a lot of experimental attention. Molecular dynamics simulations have indicated higher temperature-dependent fluctuations in the ARD at the far N terminus, more so than other areas of the protein. This was corroborated by biochemical characterization of purified ARD, which suggested that its structure might undergo conformational changes in a temperature range consistent with TRPV1 activation[31]. Also in the N-terminus, taking part of the MPD from

TRPV1 and inserting it into the channel homologue TRPV2 (another heat-sensitive channel that activates at far higher threshold temperatures, over 50°C) generated a channel whose heat gating properties trend towards those of TRPV1 more than the parent TRPV2[32]. At the other extreme of the protein, placing the complete C-terminus of TRPV1 into TRPM8 is supposed to make what was once a cold-activated receptor now activated by heat instead, albeit with notably less efficiency[33]. The same group was able to further isolate a ~25 amino acid stretch just downstream of the TRP domain that mediates this conversion[34]. In somewhat agreement with this, longer truncations of the C-terminus were shown to increasingly lower TRPV1's activation temperature threshold and make its gating transition less cooperative[35]. Besides the cytosolic domains, the extracellular parts of TRPV1 also seem to tune temperature sensitivity, particularly the pore loops between the S5 and S6 helices. Three residues scattered throughout the pore helices were identified to blunt the effect of temperature on TRP channel function when mutated, and single channel recordings of these mutations showed shorter dwell times in the open state[36]. A fourth residue in the pore loop was shown to have temperature-dependent differential water accessibility in cysteine labelling experiments[37]. An independent group studied serial deletions and exchanges of regions within the pore loops. They reported that deletion of 10 amino acids in part of the pore turret immediately after the S5 helix significantly reduced activation temperature threshold and blunted temperature responses[38]. Meanwhile, replacement of 14 amino acids immediately downstream of that initial 10 amino acid stretch with an artificial sequence ablated temperature-evoked currents altogether[39]. Adding to this, the Julius lab developed a purification construct of TRPV1 lacking 110 residues from the N-terminus, 23 residues from the pore turret, and 74 residues from the C-terminus. Despite what one could have predicted from the literature, this minimalist channel maintained similar temperature activation profiles to the wildtype

9

receptor[21]. Overall from the literature, one builds the impression that there is probably not one modular temperature sensor built into TRPV1, but that multiple areas may be involved in the process. However, the caveat even to this is that it remains difficult to distinguish between those areas that actually sense temperature and those that are simply involved in coupling thermal stimuli to the pore.

The concept of temperature sensitivity in proteins has captivated the interest of theoretical biophysicists, in addition to experimentalists. A mathematical derivation built exclusively from first principles in thermodynamics made the prediction that the acute thermal sensitivity of TRP channels is likely a consequence of their large changes in molar heat capacity as they transition from closed to open states. These large changes in molar heat capacity are suspected to originate from differential exposure of hydrophobic groups to water – or, more simply, by protein folding[40]. This framework has been implemented in a bottom-up way to build other thermally-sensitive ion channels[41]. However, it has been more challenging to test with TRPV1 specifically. Potentially in support of this idea, one study made thousands of random point mutations in TRPV1 and showed that loss of hydrophobicity was not well tolerated for heat-dependent activity, though it made no difference for capsaicin-evoked activity[42]. In another study, molecular dynamics simulations were conducted at sub- and supra-threshold temperatures for both wildtype TRPV1 and an activation-biased mutant receptor. By examining how different residues responded to temperature, a pattern of desolvation of polar and charged residues was observed to correlate with the channel opening transition[43]. One major consequence, stemming from this protein folding hypothesis of temperature gating, is that there is no necessity for one single site to serve as a temperature sensor. Thermal sensitivity can instead be scattered across multiple sites of the protein. This would help to explain why mutating different parts of TRPV1

all seem to have an impact on temperature-dependent activation[40].

The most robust elucidation of the thermal gating mechanism would probably come from a structural approach, much like what was done for ligands. However, despite witnessing many clever attempts from colleagues in the Julius and Cheng labs, the heat-activated structure remained refractory to structure-determination. The sample suffered from a range of issues – whether severe orientation bias, particle aggregation, or poor resolution – or else simply resulted in a closed-state reconstruction. A potentially important clue came from early structural work, which showed that some density always occupied the VBP, whether there was a vanilloid agonist included during grid preparation or not. This extra density in unliganded TRPV1 structures was attributed to a lipidic species and became known as the resident lipid. It was hypothesized that heat might remove this lipid as part of its activation pathway, in the same way that ligands would do[28], but the idea remained untested. Years later, the first heat-activated model of TRPV1 was eventually published. However, it came with the significant limitation that the authors needed to include capsaicin in their specimen as a sensitizing agent. Their unliganded sample at 48°C remained closed, and so their workaround was to compare a condition which was treated with 30 µM capsaicin and kept at 25°C against another treated with 30 µM capsaicin and heated to 48°C. Only in the latter case do they see a pore profile that is wide enough to conduct ions. The transition to this open state was proposed to occur in two steps. In the first, heat would induce rotations in the CTD, ARD, and VSLD that would shift the S4-S5 linker and the TRP helix, which then would tug on the S6 helices to slightly widen the lower gate. In the second step, rotations would occur in the outer pore loops that would dilate the selectivity filter. This, in turn, would couple to the S6 helices and cause them to pivot, bringing about full opening of the lower gate. The authors, inspired by the folding hypothesis of temperature activation, were also able to

map out those side chains with noticeable changes in solvent-accessible surface area. Consistent with the literature, these mapped residues were found to be located diffusely throughout the protein[44]. While this model is currently the best structural attempt to describe TRPV1 heat-dependent gating, it remains debated whether the stimulus of heat alone (as opposed to heat plus capsaicin) will follow a similar mechanism.

The Promise of TRPV1 Therapeutics

TRPV1 clearly has strong ties to nociception. While pain is often perceived as negative to the person who experiences it, it actually provides extremely important physiological feedback, as it is designed to keep us away from stimuli that are potentially injurious or lethal. In that sense, having TRPV1 react to excessive heat, acids, or venomous stings is beneficial, as it should help us to detect and avoid these[9]. That said, there is reason to suspect that TRPV1 signaling may become aberrant in conditions associated with chronic pain and inflammation, at which point it contributes to pain sensation in the absence of any painful stimulus. This includes dermatitis[45], arthritis[46], inflammatory bowel disease[47], neuropathic pain[48], even cancer[49], to name a few.

As a result, TRPV1 has emerged as a prime target in the development of novel pain therapeutics. This is especially relevant, given the backdrop of today's opioid epidemic. Because of the widespread prescription of opioid drugs to treat pain since the 1990s, the incidence of opioid use disorder has skyrocketed. Drug overdose is now the leading cause of accidental death in the United States, with opioids being the culprit in the vast majority of such cases[50]. This is because opioid drugs, while offering some of the best relief for pain, are notorious for their terrible side effects, including addictive tendencies and lethality from overdose. The opioid epidemic has therefore reinvigorated the research and clinical use of non-opioid alternatives.

While there are some great ones available, such as the non-steroidal anti-inflammatory drugs, and their side effects tend to be more benign, these drugs are not always as effective as their opioid counterparts[51,52]. This search for improved non-opioid drugs has led to TRPV1. Given its pivotal role in pain signaling and its more restricted expression pattern in nociceptive fibers, TRPV1 could be targeted to suppress pain in a way that would be both effective and lacking the same abuse potential.

It is logical to infer that, if hyperactive TRPV1 were to contribute to pain, antagonists would be the best way to achieve relief. Accordingly, most pharmaceutical investment has been directed towards the development of such antagonists. Despite this, not a single TRPV1 antagonist has successfully made it through clinical trials. The first generation of drugs failed for a few reasons. For one, there was lack of efficacy – some drugs simply did not have the lasting therapeutic effect that was anticipated. The second reason was due to many drugs inducing strong hyperthermia as a side effect. This was puzzling, as the role of TRPV1 in maintaining core body temperature was not well understood. With time, it became clearer that this effect was likely happening because there exist some TRPV1-dependent sensors in the periphery whose activity tonically stimulates cooling mechanisms. Silencing these sensors would thus suppress feedback cooling mechanisms, causing the body to erroneously develop hyperthermia. One last pitfall of the first-generation antagonists was that they sometimes led to impaired temperature sensation, so much so that it increased the risk that a patient would develop burns. To overcome these shortcomings, more recent efforts have tried to preferentially target ligand-induced activation of TRPV1 without affecting thermal sensitivity. While some preliminary antagonists have been identified that could block capsaicin-evoked, proton-evoked, and heat-evoked responses differentially, they remain to be thoroughly tested in the clinic. Furthermore, there

could exist other unidentified modality-specific antagonists out there, so the search is still underway.[9,53]

While antagonists are intuitive, it might seem paradoxical to have agonists activate TRPV1 with the intention of treating pain. However, TRPV1 agonists are being pursued in the clinic as well. The philosophy here is to dial TRPV1 activity just high enough that it brings about channel desensitization or that it silences the host nociceptor, yet not so high that causes neuropathology or lingering feelings of pain. This strategy has been used for quite some time in traditional medicine – a common example is using chili paste to treat tooth and skin pain[53]. In clinical settings, it has proven difficult to titrate the amount of agonist needed to achieve this desired effect, yet there is potential. Preliminary results from one study showed that RTX could evoke cell death of TRPV1-positive nociceptors, thus bringing prolonged pain relief to advanced cancer patients[54]. Moreover, RTX is currently in phase III clinical trials for the treatment of knee pain due to osteoarthritis.[53]

In summary, while targeting TRPV1 is still not done routinely in the clinic, this may soon change. While it looks like agonists may have more immediate use cases than antagonists, there remains great potential for both. This will hopefully provide much needed pain management strategies to replace opioid therapies and help to curb the ongoing opioid epidemic.

Figures
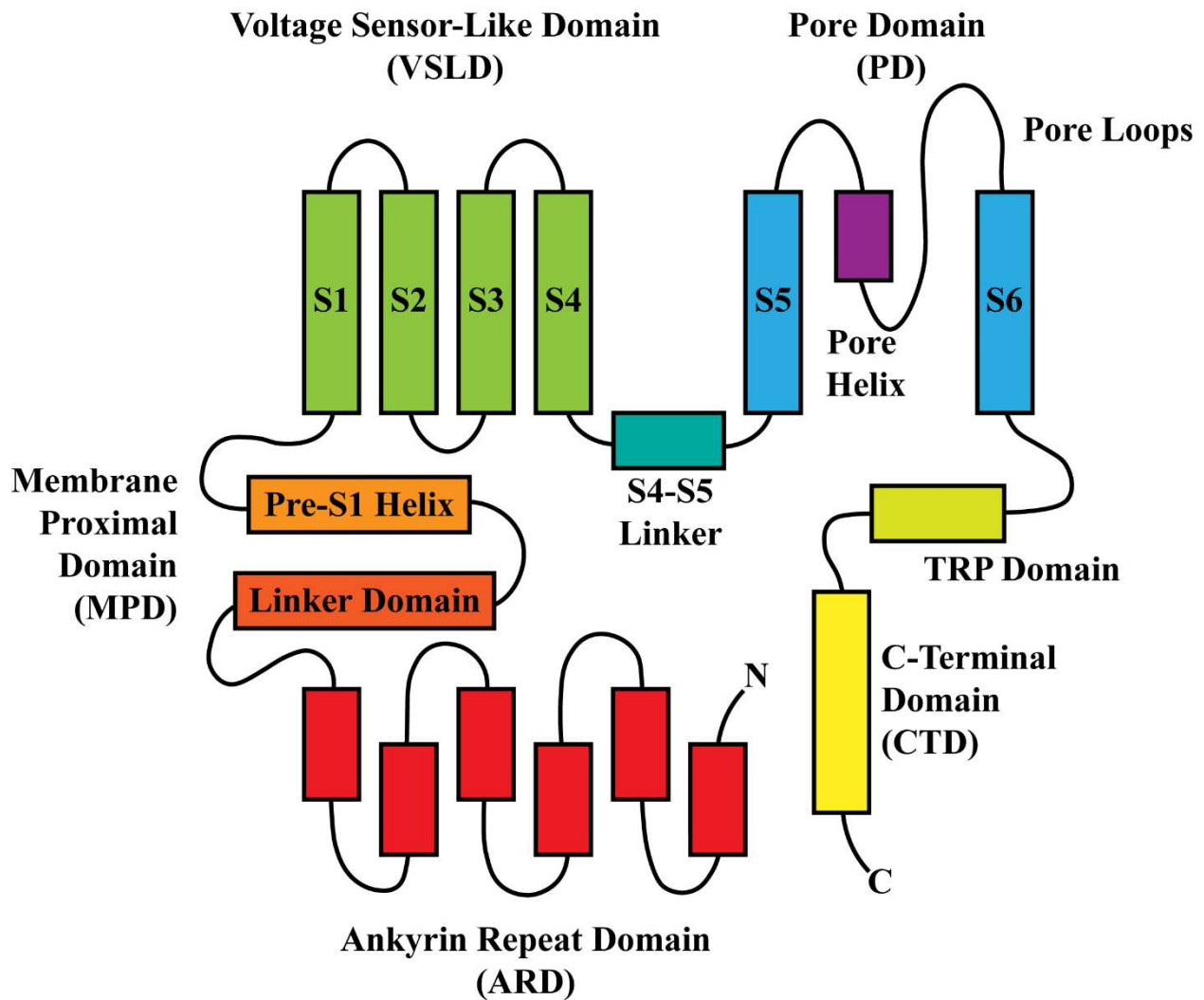
Figure 0.1 | Topology model of a single TRPV1 subunit
Topology model showing the different domains of TRPV1. Listed from the N-terminus to the C-terminus, these are: the ankyrin repeat domain (ARD); the membrane proximal domain (MPD) made up of the linker domain and pre-S1 helix; the voltage sensor-like domain (VSLD) made up of transmembrane segments S1, S2, S3 and S4; the S4-S5 linker; the pore domain (PD) made up of transmembrane segment S5, the pore loops which contains the pore helix, and S6; the TRP domain, and finally the C-terminal domain (CTD).

CHAPTER 1: MECHANISMS OF TRPV1 MODULATION BY BIOACTIVE LIPIDS

PART I

Introduction

While TRPV1 can be activated by chemical and physical stimuli alike, we know the most about how it responds to ligands. There are two main ligand-binding sites in TRPV1. Peptide toxins, which cannot easily cross the plasma membrane, bind to the extracellular surface of the channel, near the outer pore loops[19,20]. Other agonists, including the exogenous toxins capsaicin and resiniferatoxin (RTX), are smaller and more hydrophobic, allowing them to readily permeate the plasma membrane. These bind to TRPV1 in a pocket on the inner leaflet of the membrane, tucked between the voltage sensor-like domain (VSLD) and the pore domain. This site is called the vanilloid-binding pocket (VBP)[22].

What is interesting about the VBP is that it is seldom empty. Even when no agonist was applied, it was clear from cryogenic electron microscopy (cryo-EM) maps that there remained a lipidic density in the pocket. This became known as the resident lipid[28]. Early on, the resolution of published cryo-EM density maps was limiting in the resident lipid's head group region, making it difficult to assign the lipids' identity. But as data collection and processing methodologies improved, the resolution of the TRPV1 structures solved by my colleagues in the Julius and Cheng labs would more routinely reach the sub-3 Å range. As a result, it became possible to make out an inositol ring just below the VBP, establishing the resident lipid as a phosphatidylinositol (PI). The resident lipid was not visible in structures where TRPV1 was combined with capsaicin or RTX, which makes sense as they all compete for the same binding site. These observations inform a mechanism of how TRPV1 is activated by ligands. Under resting conditions, the resident lipid serves an inhibitory role, keeping the channel comfortable in its closed state. When exposed to agonists like capsaicin or RTX, which have higher affinities for

the VBP, the resident lipid would be outcompeted and thus displaced. This, combined with the newly acquired agonist-channel interactions, would trigger conformational changes which ultimately favor ion permeation[28].

While ligand action on TRPV1 is well-understood, the mechanism by which thermal activation occurs is largely unknown. There is currently no solved structure of TRPV1 exposed to heat alone, despite many attempts. The closest thing reported in the literature is a model of TRPV1 activated by 48°C but also sensitized by capsaicin[44]. While we can still gain insights about possible gating transitions from this model, it remains up for debate whether these will reflect the true mechanism of heat activation. Moreover, decades' worth of functional studies have built a consensus that no single module of TRPV1 is responsible for conferring thermal sensitivity. Instead, it seems that the role is somehow shared across parts of the N-terminus[31,32], C-terminus[33–35], and pore loops[36–39]. A more theoretical approach to understanding heat gating has tied the acute temperature sensitivity of TRP channels to large quantifiable changes in molar heat capacity and, in turn, to protein folding. In other words, according to this prediction, temperature might be causing large-scale protein folding or unfolding events, which would then drive pore opening[40]. While this study has been informative and could explain the diffuse nature of thermal gating, it remains to be confirmed by experimentation.

Just as the resident lipid is involved in chemical gating, it may possibly serve a role in thermal activation as well. Heat could possibly eject the resident lipid from the VBP, for instance by increasing membrane fluidity to allow it to exchange more readily with surrounding lipids or by disrupting key hydrophobic contacts with the channel. The loss of the resident lipid may, in turn, facilitate pore opening, mirroring what was seen with chemical agonists[28]. Interestingly, there may be precedence in the TRPV family for lipid involvement in thermal gating, as a

18

similarly-positioned lipid density that was normally present in resting structures of TRPV3 was lost in its heat-potentiated structure[55]. For this hypothesis – that heat ejects the resident lipid which leads to channel opening – to hold true, there is an intermediate assumption that likely needs to be satisfied: if the VBP were somehow to be emptied, the channel *should* be more likely to adopt an open state. With this in mind, we set out to determine the structure and assay the function of what we will call empty-pocket TRPV1 – i.e. TRPV1 where we remove the resident lipid and keep the pocket free of ligands.

Results

We devised a biochemical workflow to displace the resident lipid from the VBP and generate empty-pocket TRPV1 (**Fig 1.1**). At one point during purification, detergent-solubilized TRPV1 was immobilized to amylose resin via its maltose-binding protein tag. Here, TRPV1 was washed with detergent buffer supplemented with 5 µM capsaicin. We reasoned that capsaicin would bind to the VBP, kicking out the resident lipid in the process. The resident lipid, in turn, would undergo exchanges with the surrounding detergent buffer and be rinsed away. After that, immobilized TRPV1 was washed with copious capsaicin-free buffer. Owing to capsaicin's solubility in detergent buffer, we reasoned that this would unbind capsaicin and therefore empty the VBP. The resulting protein was then eluted from the resin and transferred into nanodiscs or liposomes depending on the experiment. At this stage, we could control the lipid composition to prevent the reintroduction of any phosphoinositide species – for the most part, we used a mixture of 55.2% molar-ratio 1,2-dioleoyl-sn-glycero-3-phosphocholine (DOPC), 36.8% 1-palmitoyl-2-oleoyl-sn-glycero-3-phospho-(1'-rac-glycerol) (POPG), and 8% cholesterol.

As a first experiment, empty-pocket TRPV1 was transferred to nanodiscs containing

DOPC, POPG, and cholesterol, and then frozen on cryo-EM grids at two temperatures, 4°C and 25°C. The data were comparable for both temperatures, so going forward only the 25°C data will be shown. The final reconstruction obtained did not feature any density in the VBP – not for the resident lipid, not for capsaicin (**Fig 1.2A**). This confirmed that our biochemical workflow was an efficient way to empty the VBP. The residues that make up the VBP were found to be re-oriented in a way consistent with ligand binding, notably that tyrosine-511 was flipped inward (**Fig 1.2A**). Upon examining the ion conduction pathway, empty-pocket TRPV1 appeared to adopt an open-like conformation. Specifically, the S6 helix transitioned from an α-helix to a π-helix, which in turn rotated isoleucine-679 away from the central axis, relieving the narrowest constriction point (**Fig 1.2B-C**). This was consistent with other published vanilloid-activated channels[27,28]. Given that the samples were prepared well below the temperature at which thermal gating would be expected (around 42°C)[6,17], the fact that TRPV1 appeared to adopt an open-like state was especially impressive.

These structural data support the hypothesis that removal of the resident lipid leads to channel opening. We next wanted to probe our empty-pocket TRPV1 sample for its function. To do so, we followed protocols established by former members of the Julius lab to transfer purified TRPV1 into liposomes and to perform patch clamp electrophysiology[17]. We first purified TRPV1 without chasing off the resident lipid and transferred it to liposomes derived entirely from soy extract polar, as a positive control. We then plated those liposomes and pulled patches, giving us access to TRPV1 in the inside-out patch clamp configuration (**Fig 1.3**). We probed currents by applying voltage-steps, from -100 mV to +120 mV, combined with simple pharmacology. We routinely saw robust currents, up to 225 pA in amplitude, when we applied 10 μM capsaicin at our highest magnitude membrane potential of +120 mV (**Fig 1.4A-C**). Those capsaicin-evoked

currents were completely inhibited when co-applying 10 µM inhibitor AMG-9810 (**Fig 1.4A-B**). From crude dose-response curves, we estimated the half maximal effective concentration (EC50) of capsaicin to be about 10 µM, consistent with previous reports in purified systems[17] (data not shown). We also conducted heat ramps, increasing the temperature of the perfused bathing solution from room temperature to over 50°C within about 10 seconds. We saw TRPV1 activity increase with a threshold of roughly ~44°C and a Q10 value of ~19 (**Fig 1.4D-G**), consistent with previous findings[17]. This indicated to us that we were successfully able to reconstitute functional TRPV1 into proteoliposomes.

We used soybean lipid-derived proteoliposomes as a positive control, because previous work indicated that purified TRPV1 was very stable in this environment[17]. However, soy extract polar is a heterogeneous blend that likely contains phosphoinositide lipids, which can interact with the VBP of our purified protein. As a next experiment, we prepared TRPV1, keeping the resident lipid intact, and transferred it to liposomes made from the same defined lipids used in the nanodisc preparation, i.e. DOPC, POPG, and cholesterol. Because there should be no phosphoinositide lipids in this mixture, the VBP should only contain the lipids that came along during purification. (*Of note:* We anticipated that the resident lipid would remain in the VBP. However, there could have been a diluting effect at play – that the resident lipid that comes from endogenous sources might have unbound the VBP and undergone exchanges with the surrounding lipid milieu. There could be partial occupancy of the VBP because of this. Owing to size differences, we presumed that this effect would be more pronounced in a liposome than in a nanodisc.). Probing with pharmacology, we showed that TRPV1 was activated by capsaicin with similar amplitude spreads compared to TRPV1 in soybean lipids, up to about 200 pA, and was completely inhibited by co-application of AMG-9810 (**Fig 1.5A-C**). We then applied heat ramps

to study temperature-dependent activation (**Fig 1.5D-E**). Interestingly, the recordings we observed looked qualitatively unique. TRPV1 heat-evoked currents in defined lipids did not increase as sharply as they did in soy polar extract and did not reach the same high amplitudes (**Fig 1.5F**). Consistent with this, quantification by Arrhenius plots showed a shift in the threshold temperature for activation, to about 39°C, and a decrease in the Q10 value, down to 3.9 (**Fig 1.5G**).

Finally, we wanted to test the consequences of removing the resident lipid altogether. While TRPV1 was immobilized to the affinity resin, we incorporated washes designed to empty the VBP. We then eluted empty-pocket TRPV1 and transferred it to liposomes made up from our defined lipid mixture, i.e. DOPC, POPG, and cholesterol. During patch clamp experiments, we saw capsaicin-evoked currents, which returned to baseline following co-application of AMG-9810 (**Fig 1.6A-B**). However, the spread of the response amplitudes was far more limited in this empty-pocket TRPV1 condition, never exceeding 50 pA in magnitude (**Fig 1.6C**). When compared to the condition of TRPV1 with the resident lipid intact, this amplitude distribution was found to be significantly different ($p < 10^{-4}$). We saw no increased activity in the absence of agonist, suggesting that the channel was not constitutively active either (**Fig 1.6A-B**).

When we probed with heat ramps, though, the data were far more difficult to interpret. Unlike the previous conditions, we very rarely observed macroscopic increases in current – only one out of 104 attempted temperature ramps yielded a large enough current to measure accurately (**Fig 1.6D-E**). Its threshold and Q10 values were estimated to be 39°C and 3.6, respectively (**Fig 1.6F**), consistent with the values reported for the defined lipid condition with the resident lipid kept intact (**Fig 1.5G**). We did obtain many recordings where it appeared as though there were potentially a single channel (or at least a few channels) opening and closing

asynchronously in a way that was temperature-dependent (**Fig 1.7A**). These openings appeared as transient (<1 ms) but large (>12 pA) blips (**Fig 1.7B**), admittedly quite unlike the rectangular pulses that one would expect from single-channel recordings of TRPV1[6]. We rationed that these "mini events" could reflect TRPV1 activity that is not sustained or that is dampened by the noise in the recording setup (since the conditions used were optimized for macroscopic patches, not single channels necessarily). For these particular recordings, the TRPV1 signal compared to the leak of the patch (i.e. signal-to-noise ratio) was too low to simply measure temperature activation as current versus temperature. We could, as a surrogate, plot temperature activation as the frequency of these events happening as a function of temperature. When we compared activation profiles for when the resident lipid was chased off and when it was left intact, we did not notice any differences, as TRPV1 activity began around 40°C in both cases (**Fig 1.7C**). Overall, our functional data did not agree with the observation of an open-state structure with cryo-EM (**Fig 1.2C**).

We worried that removal of the resident lipid led to protein instability that made it difficult to reconstitute TRPV1 efficiently into liposomes. This was corroborated by size exclusion chromatography data from the nanodisc reconstitutions, which showed a higher void peak when the sample had its resident lipid removed compared to when it was left intact (**Fig 1.8**). We therefore opted for an alternative experiment, one where we attempted to chase off the resident lipid *after* TRPV1 was embedded in a liposome environment. We purified TRPV1, keeping the resident lipid intact, and transferred it to defined lipid liposomes of DOPC, POPG, and cholesterol. For at least 15 minutes prior to pulling patches, we immersed our sample in bathing solution containing 5 µM of the reversible antagonist capsazepine. The expectation here was that the resident lipid would be displaced by capsazepine and become so dilute within the

surrounding liposome mass, that it would likely not be around when it came time to pull an excised patch. This would effectively produce a TRPV1 sample where the resident lipid was chased away after liposome reconstitution. We then pulled excised patches and perfused on bathing solution lacking capsazepine, to wash away the inhibitor. (Of note: the internal pipette solution did not contain capsazepine). Over the course of five minutes, we did not observe an increase in channel activity – quite the contrary we saw a tighter seal develop (**Fig 1.9A-B**). To confirm that TRPV1 was indeed in our patches, after 5 minutes of washing, we could apply 10 μM capsaicin to evoke TRPV1 currents (**Fig 1.9A-B**). Furthermore, this TRPV1 activity could be silenced again by moving the electrode tip out of the agonist perfusion path and into the surrounding bathing solution, since it contained capsazepine (**Fig 1.9A-B**). The same result occurred for capsazepine-free washes lasting up to 8 minutes in duration (data not shown), longer exposures than that were not attempted. Assuming that capsazepine was being washed out in this timeframe, this suggested to us that having an empty VBP did not inherently lead to channel activity. Again, these observations disagreed with the gain-of-function phenomenon reported by cryo-EM.

Discussion

The many published ligand-bound structures of TRPV1 have enabled us to piece together how chemical stimuli gate the channel. In contrast, the mechanism by which temperature allows for activation remains far less clearly defined. A lipid normally resides in the VBP of TRPV1 under resting conditions, where it has been hypothesized to play a role in ligand gating. Whether its removal is also a step towards TRPV1 activation by heat has remained unclear. If so, a key assumption would likely need to hold true – that removal of the resident lipid should have a

stimulatory effect on the channel.

We devised a protocol to isolate an empty-pocket TRPV1 sample – by first washing on capsaicin to displace the resident lipid from the VBP, followed by copiously rinsing with capsaicin-free buffer to remove the agonist. We then transferred this empty-pocket TRPV1 to nanodiscs and solved its high-resolution structure at temperatures below the activation threshold. Not only did we confirm that the pocket was indeed empty, but the channel's permeation pathway seemed to closely resemble agonist-bound structures. In parallel, we took the same protein, applied the same wash protocol, and transferred it to proteoliposomes for patch clamp electrophysiology. We expected to see some sort of gain-of-function activity, to be consistent with the cryo-EM, but we did not observe that. Pharmacologically-activated currents were smaller in amplitude and temperature-evoked recordings were borderline impossible to obtain. If anything, this pointed towards a loss-of-function outcome.

Though it would have been ideal if the two methodologies were to agree with one another, electrophysiology and cryo-EM probe very different types of data. For one, there is a difference in the scale of the particles assayed. In cryo-EM, it is possible to probe thousands to millions of particles and to parse them very finely. Our final reconstructions included just ~37,000 of the total ~590,000 particles for the 4°C sample, and ~39,000 of the total ~801,000 particles for the 25°C sample. Therefore, only about 5% of all particles assayed adopted the open-like conformation (*Of note*: This does not mean that the other 95% of particles were closed, but simply did not enter the final reconstruction). With electrophysiology, we can sample just tens of TRPV1 particles, at best. As a back-of-the-envelope calculation… given that the unitary conductance of TRPV1 is about 80 pS[6] and that the maximum current we observed at +120 mV was 225 pA, we could calculate the maximum number of channels engaged at once to be about

25. Assuming that 5% of particles had their resident lipid removed and could adopt an open conformation, that would translate to just one open channel in our recording system, which would be very difficult to detect. In this respect, the electrophysiology data do not invalidate the initial hypothesis, but are perhaps not fine-tuned enough given the marginal population of interest.

Another difference between the two techniques stems from sample preparation. We suspect that removing the resident lipid from the VBP rendered TRPV1 quite prone to aggregation, based on our size exclusion chromatography data. This is consistent with the observation that current amplitudes were lower in the empty-pocket condition relative to the resident lipid intact condition. In the case of nanodiscs, because size exclusion chromatography was feasible, we could somewhat work around this propensity for aggregation, selecting for the most stably folded sample by concentrating the appropriate non-void fractions. However, for liposomes, we had no similar method to isolate well-folded TRPV1. There may have even been a chaperoning effect conferred by MSP proteins that helped to keep TRPV1 in a stable state in nanodiscs, a benefit not available in liposomes. This instability does more damage than simply making electrophysiological recordings more difficult to obtain, rather it favors a type of survivor bias. TRPV1 particles that, despite washing, would maintain their resident lipids would be more stable and thus would more likely be reconstituted into nanodiscs or liposomes, in contrast to their less stable empty-pocket counterparts. In cryo-EM, we can exclude these contaminant particles from the final reconstruction, because it was possible to visualize (by classification) the contents of the VBP on a per-particle basis. However, in electrophysiology, this kind of quality-control is impossible to achieve – we cannot confirm that each VBP is empty and we can only sample activity at the population level. Because of these challenges, it is

possible that the electrophysiology data collected do not actually reflect the true behavior of empty-pocket TRPV1, but rather that of TRPV1 where the resident lipid remained unintentionally intact.

To address this concern of particle instability, we did attempt to generate empty-pocket TRPV1 by chasing away the resident lipid with the inhibitor capsazepine only after reconstitution into liposomes. We then washed away the capsazepine after patch excision, with the rationale that the resident lipid was probably too diluted within the liposome to be carried into the patch. Even in this experiment though, we did not observe gain-of-function activity. However, we do wonder in retrospect if we may have needed longer recording times to fully unbind capsazepine.

For the reasons above, it could be that chasing away the resident lipid from the VBP indeed activates TRPV1, and that the electrophysiology data fail to capture this effect. However, we cannot rule out that the electrophysiology data are actually correct, that the channel simply is not more active in the absence of its resident lipid. It could be that the open-like state that we observe with cryo-EM is not actually conductive or long-enough lived for patch clamp electrophysiology. After all, in the cryo-EM reconstruction, while the lower gate was clearly more opened, the upper gate appeared decidedly shut. To investigate this further, molecular dynamics simulations might be helpful. The open-like state of empty-pocket TRPV1 may even be an artefact of the capsaicin washes designed to remove the resident lipid, or of reconstitution into nanodiscs. Of course, even if the structural and functional data were to agree with one another (which would have been very nice), the next obvious question remains whether this empty-pocket TRPV1 is a true intermediate in the path towards heat activation of TRPV1 at all.

Figures
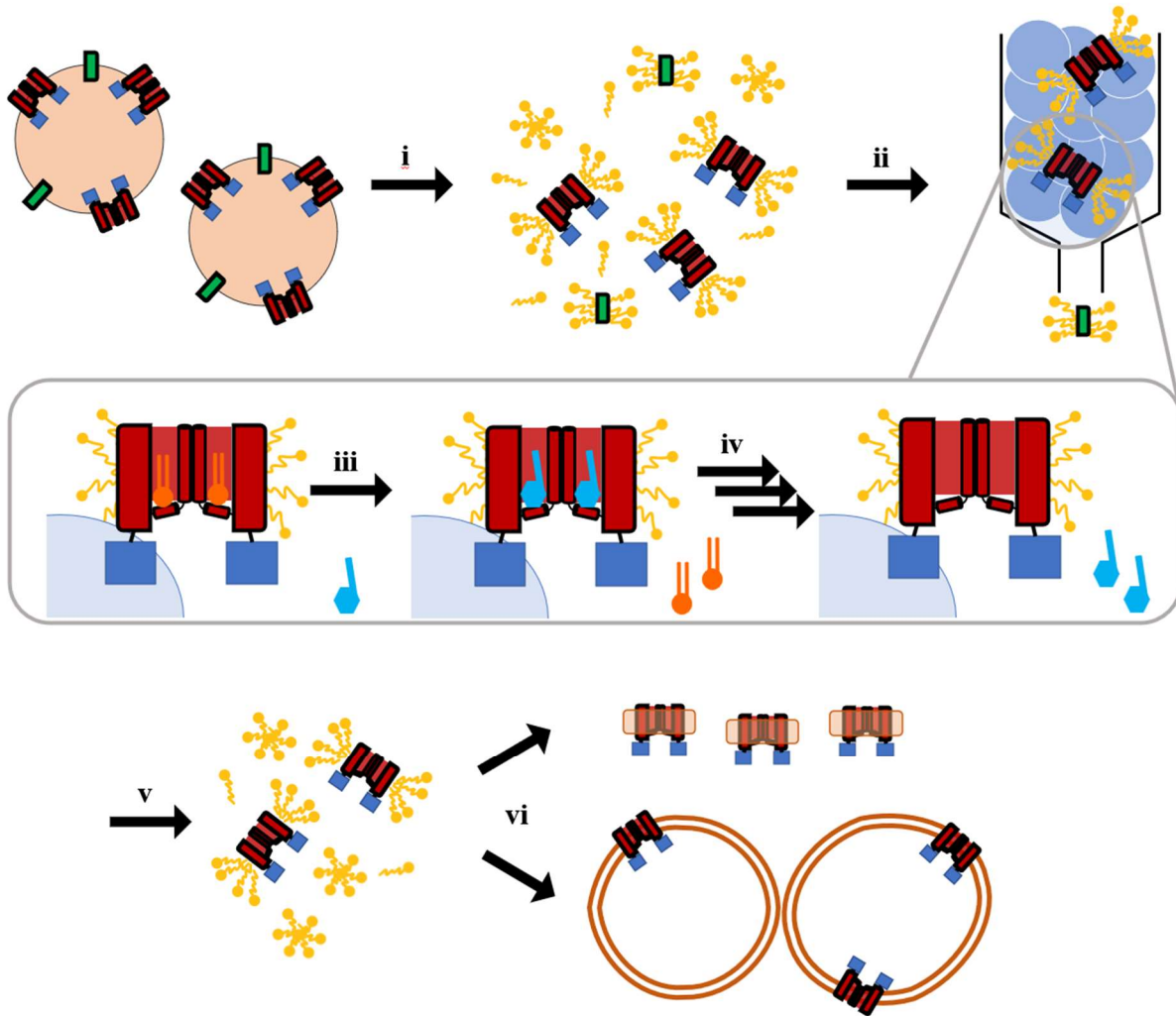
Figure 1.1 | Chasing off the resident lipid before reconstitution, purification overview
(i) TRPV1 was expressed in heterologous cell lines and extracted using the detergent n-dodecyl-β-D-maltopyranoside (DDM). **(ii)** Detergent-solubilized TRPV1 was bound to amylose resin via its maltose-binding protein (MBP) tag. **(iii)** While immobilized to the column, TRPV1's resident lipid (orange) was removed from the VBP by capsaicin (blue) washes. **(iv)** Capsaicin was in turn washed out of the VBP with copious agonist-free buffer washes, resulting in empty-pocket TRPV1. **(v)** Empty-pocket TRPV1 was then eluted from the column by addition of maltose and then **(vi)** transferred to either MSP2N2-derived nanodiscs or liposomes for structural or functional study, respectively.
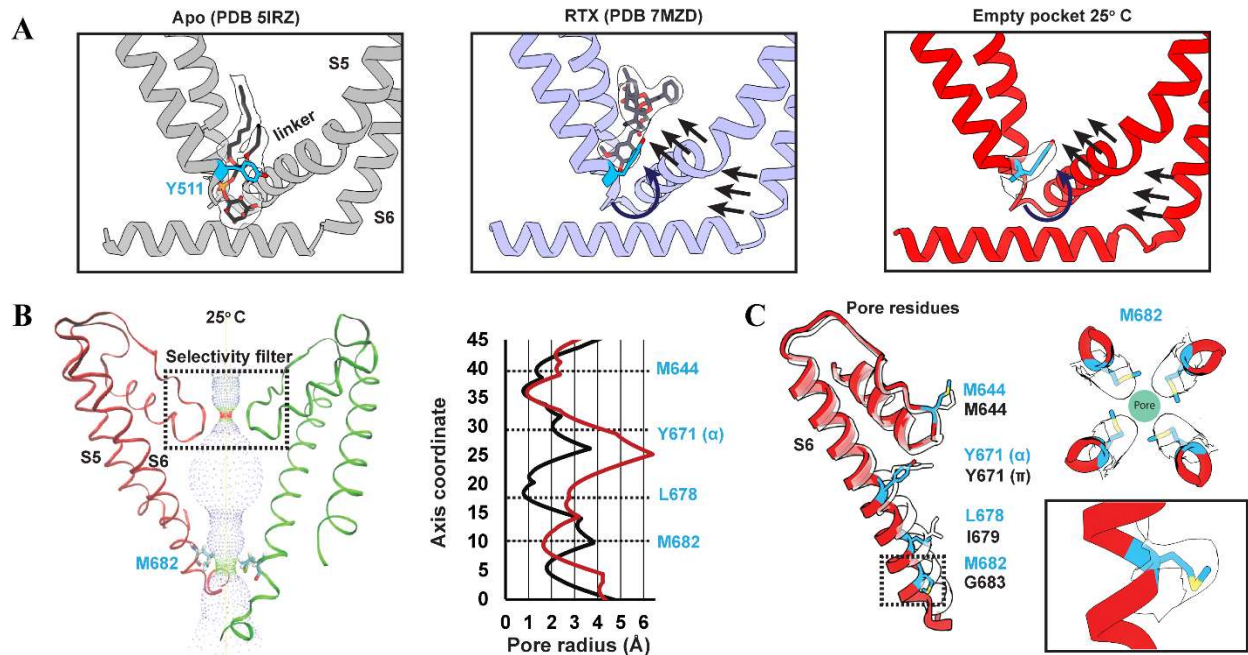
Figure 1.2 | Structural analysis of empty-pocket TRPV1
A) Protein models of the VBP in the unliganded state (from PDB 5IRZ, left), bound with RTX (from PDB 7MZD, center), and in the empty-pocket state at 25°C (from PDB 8U3L, this study, right). **B)** Pore profile analysis of empty-pocket TRPV1 at 25°C. Left shows model ribbon model of two monomers' S5 and S6 helices. Note the constricted selectivity filter and expanded lower gate. Right shows pore radius plots of empty-pocket TRPV1 at 25°C (red) and unliganded TRPV1 (black) as determined using the HOLE program. **C)** Key residues lining the channel pore. Red ribbon with blue labels depicts empty-pocket TRPV1 at 25°C, transparent ribbon represents unliganded TRPV1.
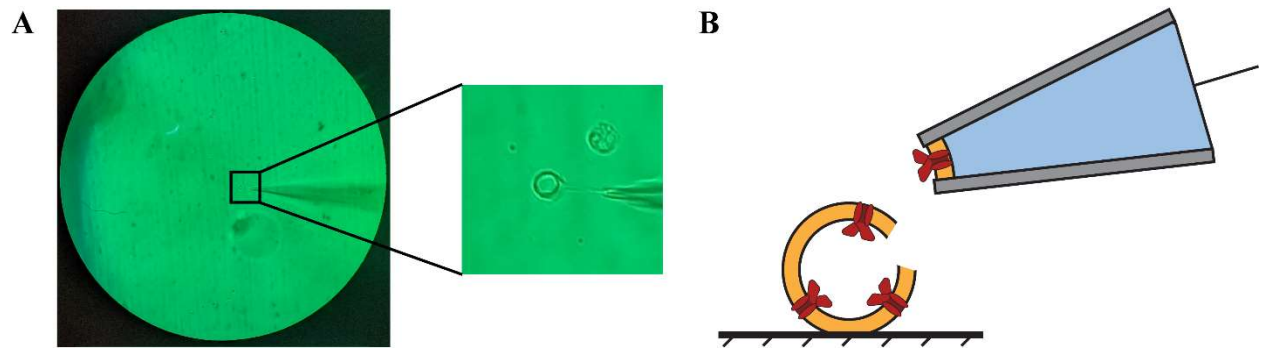
Figure 1.3 | TRPV1 excised from proteoliposomes, in the inside-out configuration
A) Light microscope view showing excised patch being pulled from multilamellar proteoliposome. B) Cartoon of excised patch, highlighting inside-out orientation of particles.
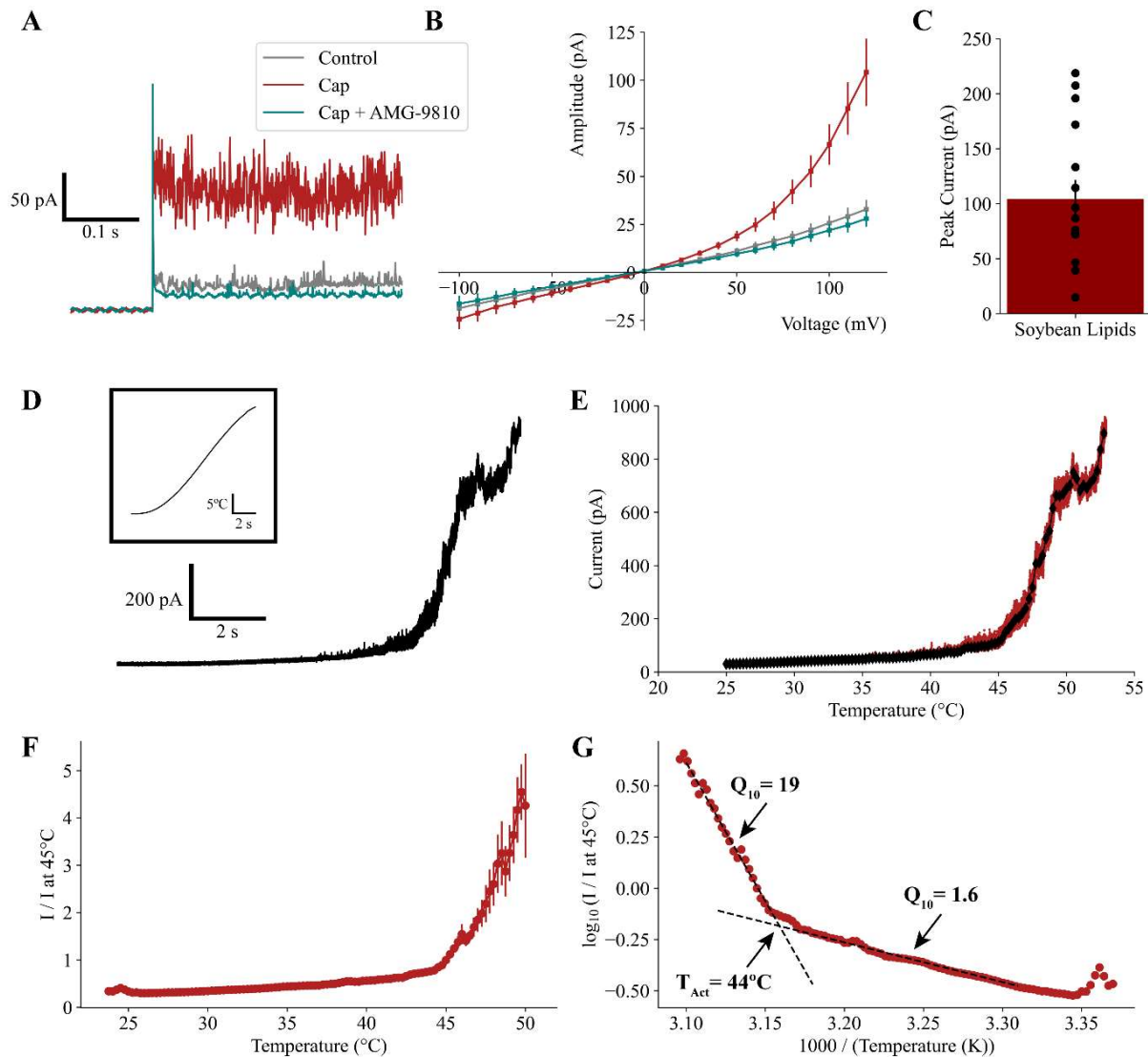
Figure 1.4 | Functional analysis of TRPV1 in soybean proteoliposomes
A) Sample current trace when voltage is stepped from 0 mV to +120 mV, in the presence of bathing solution (grey), 10 µM capsaicin (Cap, red), and co-applied 10 µM capsaicin and 10 µM AMG-9810 (teal). B) Averaged current-voltage relationships obtained in the presence of bathing solution (grey), 10 µM capsaicin (red), and co-applied 10 µM capsaicin and 10 µM AMG-9810 (teal). Data are plotted as mean ± S.E.M, n = 15. C) Distribution of peak currents obtained when applying 10 µM capsaicin at +120 mV. Points are individual data values, bar graph is shown as mean ± S.E.M, n = 15. D) Sample current trace during a heat ramp, with holding potential set to +100 mV. Inset shows corresponding heat ramp temperature versus time. E) Current plotted against temperature for the trace shown in D), to measure temperature-dependent activation. Red reflects data points, black is the rolling average. F) Current vs temperature activation plots averaged across all recordings, normalized such that the current at 45°C is 1 for each recording. Data are plotted as mean ± S.E.M, n = 11. G) Arrhenius plot for averaged data shown in F). Temperature threshold for activation was calculated to be 44°C, Q_{10} values were 1.6 and 19, before and after activation threshold, respectively.

31

Figure 1.5 | Functional analysis of TRPV1 with resident lipid in defined lipid proteoliposomes

A) Sample current trace when voltage is stepped from 0 mV to +120 mV, in the presence of bathing solution (grey), 10 µM capsaicin (Cap, red), and co-applied 10 µM capsaicin and 10 µM AMG-9810 (teal). B) Averaged current-voltage relationship obtained in the presence of bathing solution (grey), 10 µM capsaicin (red), and co-applied 10 µM capsaicin and 10 µM AMG-9810 (teal). Data are plotted as mean ± S.E.M, n = 21. C) Distribution of peak currents obtained when applying 10 µM capsaicin at +120 mV. Points are individual data values, bar graph is shown as mean ± S.E.M, n = 21. D) Sample current trace during heat ramp, holding potential set to +100 mV. Inset shows corresponding heat ramp temperature versus time. E) Current plotted against temperature for the trace shown in D), to measure temperature-dependent activation. Orange reflects data points, black is rolling average. F) Current vs temperature activation plots averaged across all recordings, normalized such that the current at 45°C is 1 for each recording. Data are plotted as mean ± SEM Red shows condition with soybean lipids from Fig 1.4F, orange shows condition with defined lipids from this figure, (Figure caption continued on the next page.)

(Figure caption continued from the previous page.) n = 14. G) Arrhenius plot for averaged data shown in F), condition with defined lipids only. Temperature threshold for activation was calculated to be 39°C, Q_{10} values were 1.5 and 3.9, before and after activation threshold temperature, respectively.
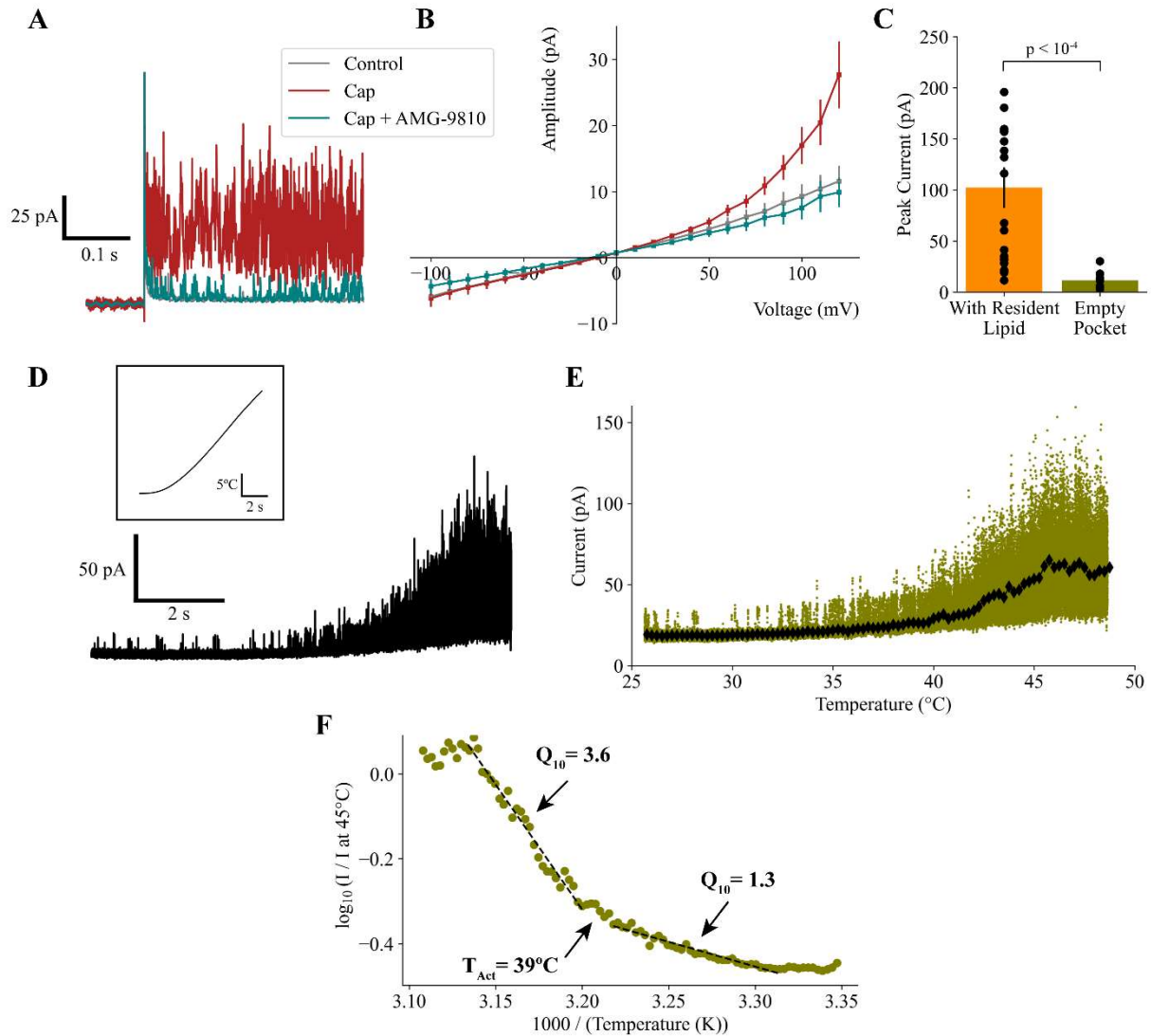
Figure 1.6 | Functional analysis of TRPV1 empty-pocket in defined lipid proteoliposomes
A) Sample current trace when voltage is stepped from 0 mV to +120 mV, in the presence of bathing solution (grey), 10 µM capsaicin (Cap, red), and co-applied 10 µM capsaicin and 10 µM AMG-9810 (teal). B) Averaged current-voltage relationship obtained in the presence of bathing solution (grey), 10 µM capsaicin (red), and co-applied 10 µM capsaicin and 10 µM AMG-9810 (teal). Data are plotted as mean ± S.E.M, n = 11. C) Distribution of peak currents obtained when applying 10 µM capsaicin at +120 mV, comparing conditions with the resident lipid (orange, n = 21) to empty-pocket (green, n = 11). Points are individual data values, bar graph is shown as mean ± SEM Statistical test was Mann-Whitney U, U = 10.0, $p < 10^{-4}$. D) Sample current trace during heat ramp, holding potential set to +100 mV. Inset shows corresponding heat ramp temperature versus time. E) Current plotted against temperature for the trace shown in D), to measure temperature-dependent activation. Green reflects data points, black is rolling average. F) Arrhenius plot for single recording shown in E). Temperature threshold for activation was calculated to be 39°C, Q_{10} values were 1.3 and 3.6, before and after activation threshold temperature, respectively.
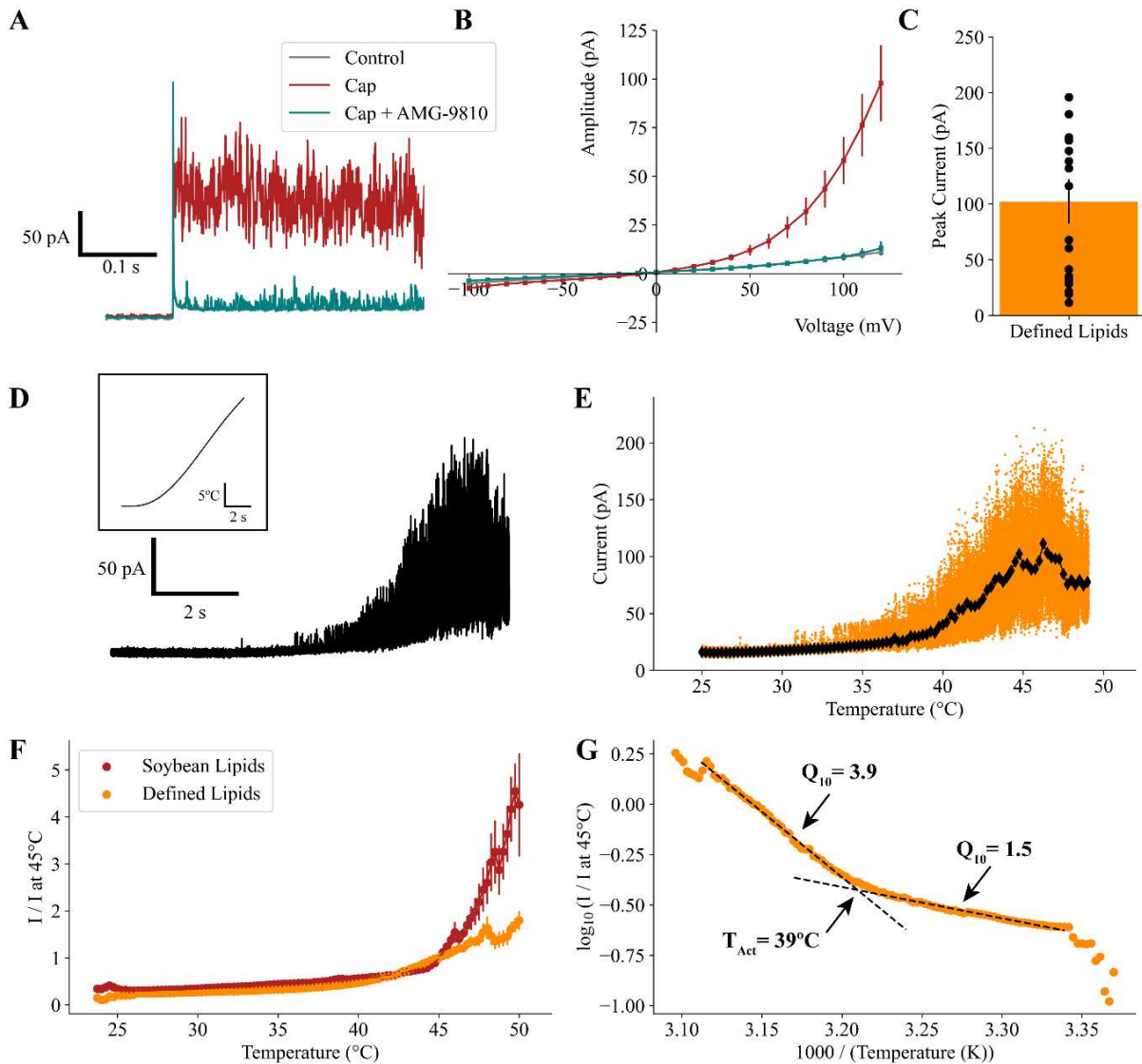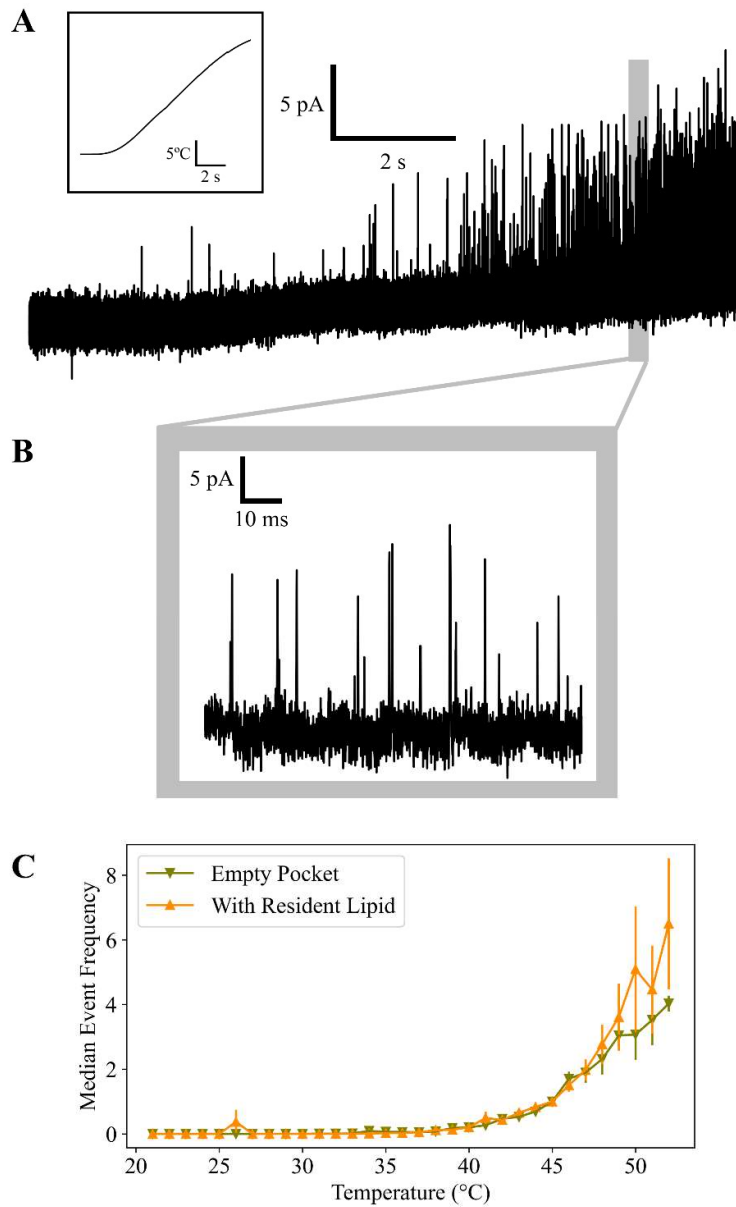
Figure 1.7 | Mini event analysis of TRPV1 with resident lipid and with empty pocket in defined lipid proteoliposomes

A) Sample current trace when applying increasing temperature, holding potential set to +100 mV. Inset shows corresponding heat ramp temperature versus time. Greyed zone is subregion further shown in B). B) Expanded view of current trace from A), showing mini events as very brief (<1 ms) and large (>12 pA) current deflections from baseline. C) Median mini event frequency plotted against temperature, to measure temperature-dependent activation. Data are graphed as mean ± SEM, n = 16 and n = 8 for the resident lipid and empty-pocket conditions, respectively.
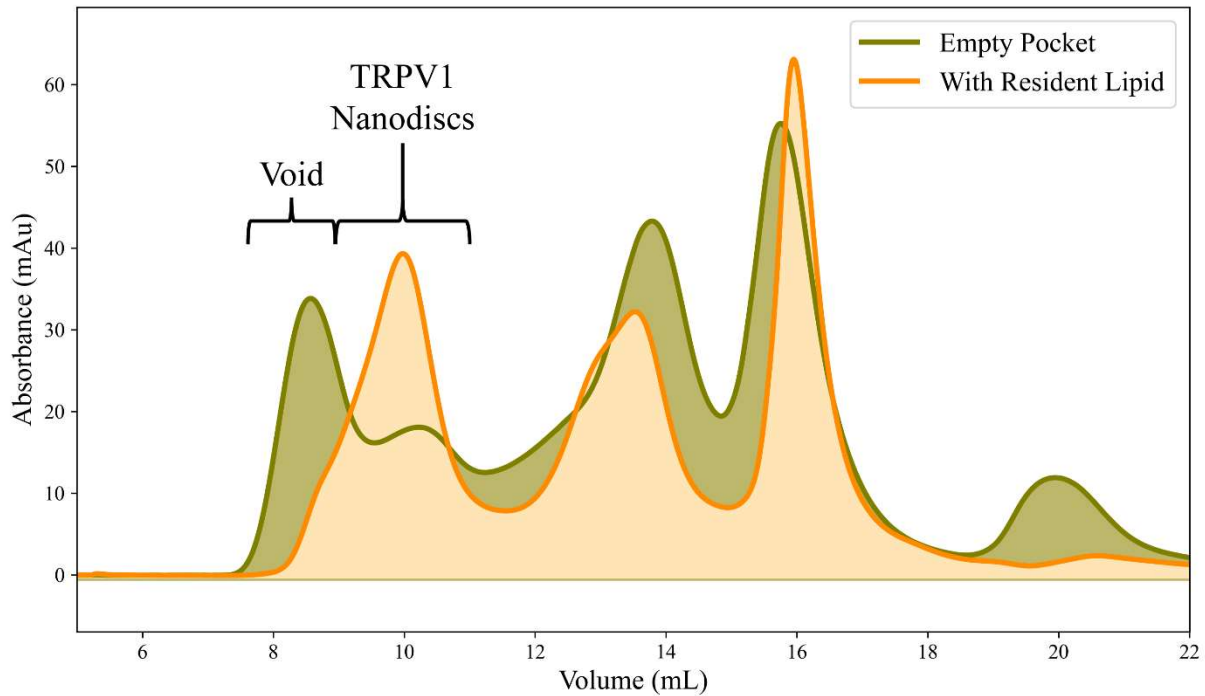
Figure 1.8 | Size exclusion chromatography profiles for TRPV1 with resident lipid and empty pocket nanodisc samples
Overlaid size exclusion chromatography profiles of both empty-pocket TRPV1 (green) and TRPV1 prepared normally with resident lipid intact (orange) prior to nanodisc reconstitution. Notice the larger void peak and smaller TRPV1 nanodisc peak in the empty-pocket condition when compared to the resident lipid intact condition. Sizing was done with Superdex 200 Increase 10/300 GL column.

A

——	0 min
——	1 min
——	2 min
——	3 min
——	4 min
——	5 min
——	10 µM Cap
——	5 µM Cpz

B
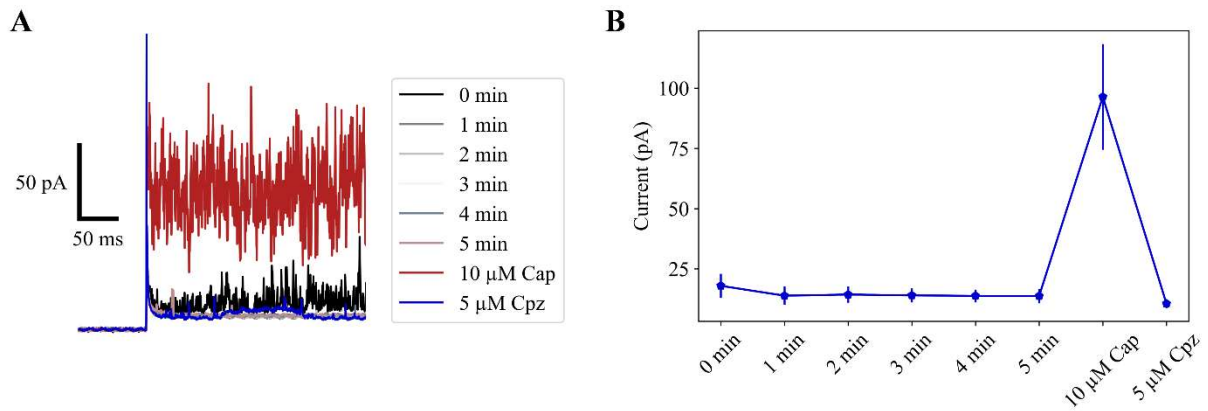
Figure 1.9 | Chasing off the resident lipid after liposome reconstitution with capsazepine
A) Sample current traces when voltage is stepped from 0 mV to +120 mV, across different conditions from a single recording. The patch was first probed in bathing solution containing capsazepine (0 min) and then in the flow of bathing solution lacking capsazepine over time (1 min, 2 min, 3 min, 4 min, and 5 min). After 5 minutes, the patch was exposed to 10 µM capsaicin (Cap) and then returned to the bath solution containing 5 µM capsazepine (Cpz). Color scheme is shown to the right of the traces. B) Quantification of data in A) across all recordings, n = 6. Data are shown as mean ± SEM
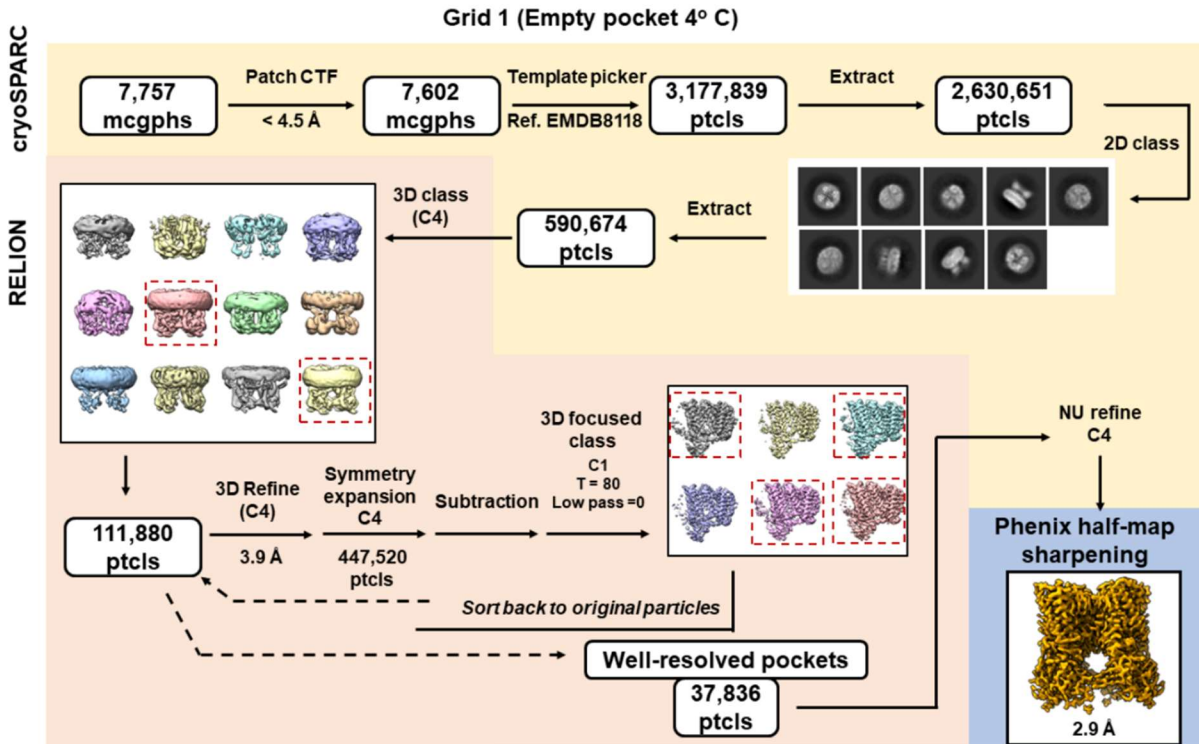
Figure S1.1 | Data processing for empty-pocket TRPV1 frozen at 4°C
Schematic shows data processing workflow, starting with picking and 2D classification in CryoSPARC, followed by 3D classification in Relion, then 3D refinement in CryoSPARC, and finally sharpening in Phenix.
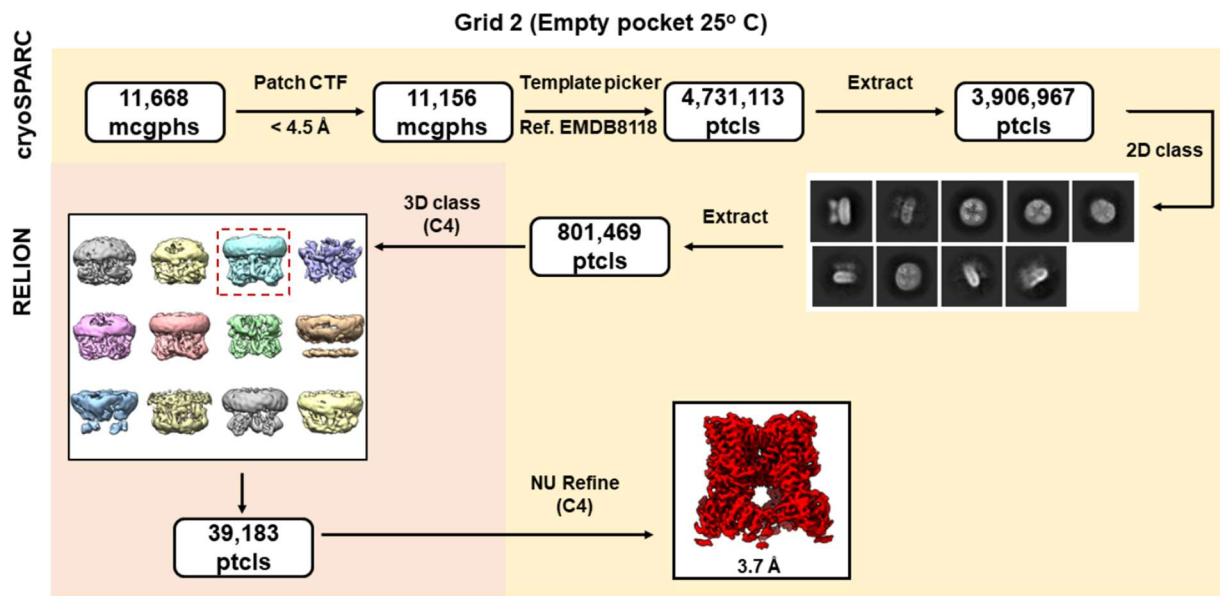
Figure S1.2 | Data processing for empty-pocket TRPV1 frozen at 25°C
Schematic shows data processing workflow, starting with picking and 2D classification in CryoSPARC, followed by 3D classification in Relion, then finally 3D refinement in CryoSPARC.
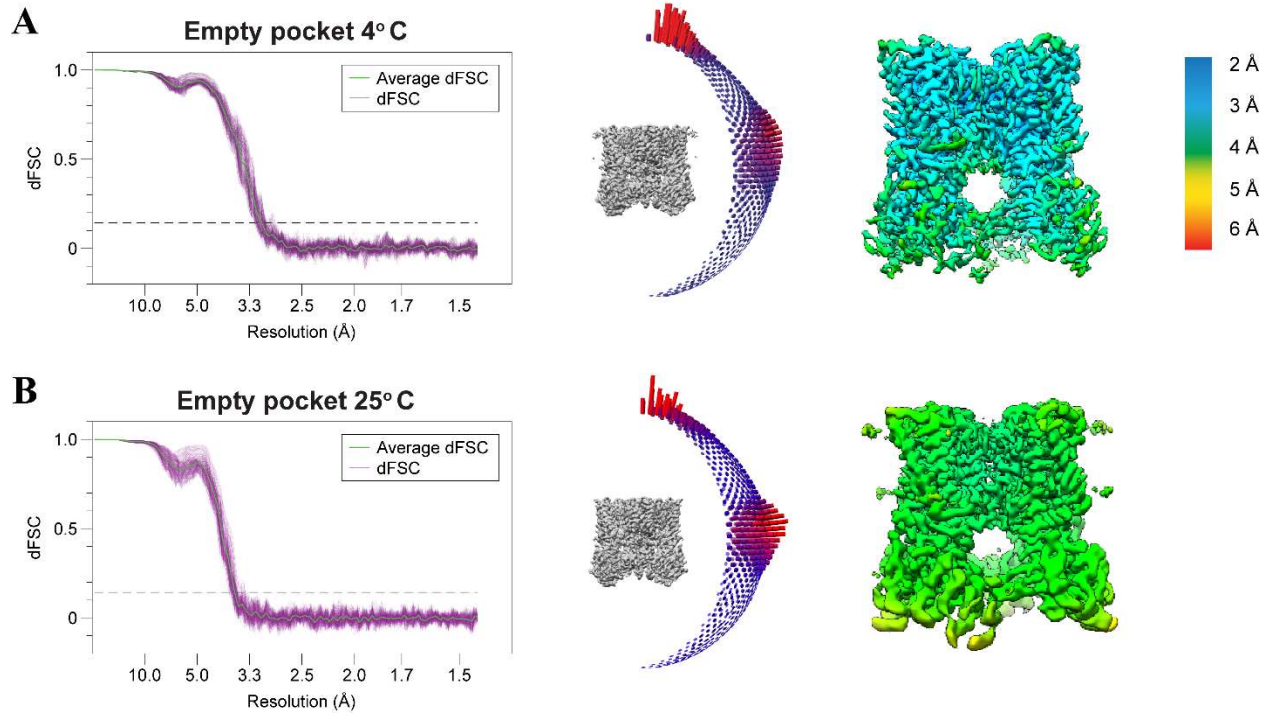
Figure S1.3 | Cryo-EM volume end parameters for empty-pocket TRPV1 samples frozen at 4°C and 25°C
From left to right: plots of directional Fourier shell correlation (dFSC) curves, angular distributions, and local resolution (colored according to key in top right) for conditions of **A)** empty-pocket TRPV1 at 4°C and **B)** empty-pocket TRPV1 at 25°C.

Table S1.1 | Parameters for reconstructions of empty-pocket TRPV1 at 4°C and 25
Microscope data acquisition parameters and model parameters for the two datasets.

		Empty-Pocket 4ºC (Grid 1)	Empty-Pocket 25ºC (Grid 2)
Ascension Codes	PDB	8U3J	8U3L
	EMD	41864	41866
Atoms	All	35,217	35,217
	Hydrogens	17,724	17,724
	Residues	2,136	2,136
Ligands	Na+	1	1
	Phosphatidic acid (3PH)	1	1
RMSZ deviation	bond length (Å)	0.28	0.28
	bond angle (°)	0.50	0.47
Validation	Clash score	5	5
	Poor rotamers (%)	0	0
Ramachandran	Favored (%)	95	94
	Allowed	5	6
	disallowed	0	0
Microscope	Microscope ID	TEM gamma (S^2C^2)	TEM beta (S^2C^2)
	Magnification	130,000 ×	130,000 ×
	Voltage (KeV)	300	300
	Dose (e⁻/pix/frame)	1.02	1.02
	Total dose (e⁻/Å)	60	60
	Defocus range (μm)	0.5-2.0	0.5-2.0
	Pixel size (Å)	0.68	0.68
Data processing	Micrographs	7,757	11,668
	Initial particles	590,647	801,469
	Final particles	37,836	39,183
	Box size (pix)	416	416
	Symmetry	C4	C4
	Map resolution (Å)	2.9	3.7
	FSC threshold	0.143	0.143
	Map sharpening	Phenix Half-Map	CryoSPARC
	B-factor	NA	-152.4
	Final adjusted map surface area	1.98	NA
	Final map kurtosis	128.61	NA

Introduction

Despite making up less than 1% of all phospholipids, phosphatidylinositol 4,5-bisphosphate (i.e. $PI(4,5)P_2$ or PIP_2) governs a multitude of cellular processes, ranging from cytoskeletal dynamics to signal transduction[56]. Most, if not all, TRP channels (let alone ion channels in general) are regulated by PIP_2, with TRPV1 being the first identified and having the most extensive background literature. Despite this, there lacks a consensus on the valence of PIP_2's effect on TRPV1[16,57].

Initial investigation by the Julius lab suggested that PIP_2 had an inhibitory effect on TRPV1. This was because depletion of PIP_2 by exogenous phospholipase C as well as by antibody sequestration appeared to sensitize TRPV1 to agonists in excised patches from HEK-293 cells and Xenopus oocytes[15]. Subsequent work identified a site in the C-terminus that could bind PIP_2, mutation of which was demonstrated to boost channel activity as if released from tonic PIP_2 inhibition[58]. Consistent with this, reconstituting purified TRPV1 into defined-lipid liposomes that contained full-length PIP_2 increased both the half maximal effective concentration (EC50) of capsaicin as well as the activation temperature threshold[17].

Other groups, in contrast, have reported an excitatory effect of PIP_2 on TRPV1. Water-soluble PIP_2 was shown to potentiate capsaicin-mediated TRPV1 currents in excised patches from F-11 neuroblastoma cells and acutely dissociated mouse dorsal root ganglion neurons[59], from Xenopus oocytes[60], as well as from HEK-293 and HeLa cells[61]. Full-length PIP_2 was found to boost capsaicin-evoked TRPV1 currents in excised patches from F-11 neuroblastoma cells[59], and was even reported to evoke TRPV1 currents directly in excised patches from HeLa cells (i.e. without capsaicin pre-incubation)[62]. Furthermore, PIP_2 appears to play a role in receptor

desensitization, as supplementing water-soluble PIP_2 curbed tachyphylaxis in whole-cell recordings from SF21 insect cells[63] and delayed desensitization in whole-cell recordings of HEK-293 cells[60]. Consistent with this, depletion of endogenous PIP_2, whether by blocking kinases involved in PIP_2 synthesis or stimulating lipases involved in PIP_2 hydrolysis, suppressed recovery from desensitization in whole-cell recordings from HEK-293 cells[64,65].

The discrepancy in these outcomes might, at least in part, be explained by the type of PIP_2 compound used in these experiments. Full-length PIP_2 is notoriously difficult to handle, as it is insoluble in most aqueous buffers. That said, a short-chained form of PIP_2, also called DiC8-PIP_2, is commercially available. DiC8-PIP_2 is presumed to have similar pharmacology to full-length PIP_2, with the added benefit that it is more water-soluble on account of its shorter aliphatic chains (8 versus 16 carbons). For this reason, the short-chain form of PIP_2 is regularly used instead of its full-length form. Whether full-length PIP_2 and short-form PIP_2 behave the same, however, is not exactly clear, especially on purified TRPV1. We therefore took a combined structural and functional approach to investigate this.

Results

We first wanted to examine the effects of full-length PIP_2 on TRPV1. We purified TRPV1 and chased away its resident lipid from the VBP to generate an empty-pocket sample, as done in Chapter 1 Part 1 (**Fig 1.1**). We then transferred empty-pocket TRPV1 to nanodiscs, made from a defined lipid mixture of 49.2% molar-ratio DOPC, 32.8% POPG, 8% cholesterol, and 10% PIP_2. The PIP_2 analog used was full-length (with 16-carbon-long aliphatic chains) but had its alkene groups modified by bromination, making it PIP_2-Br_4 (**Fig 1.10A**). We reasoned that the bromines would serve as a fiducial marker that would help to identify PIP_2-Br_4 in the pocket. The sample

43

was then advanced to structure determination by cryo-EM. The final reconstruction showed lipidic density in the VBP (**Fig 1.10B**). At a glance, this was similar to the resident lipid. However, upon closer inspection, there was clearly additional density around the inositol head group, corresponding to the two phosphate moieties of PIP_2 (**Fig 1.10C**). Likewise, there was extra density found around the two bromine atoms of one aliphatic chain (**Fig 1.10C**). Together, these features allowed us to confidently identify the lipidic species as PIP_2-Br_4. Meanwhile, the configuration around the central pore was very similar to previously published unliganded structures (**Fig 1.10D**). This is in keeping with the inhibitory effect of full-length PIP_2 on TRPV1, as reported by the Julius lab.

Next, we aimed to resolve how DiC8-PIP_2 binds to TRPV1. We purified empty-pocket TRPV1 and transferred it into nanodiscs made from 55.2% molar-ratio DOPC, 36.8% POPG, and 8% cholesterol. We then incubated the sample with 50 μM DiC8-PIP_2 (**Fig 1.11A**) just before grid vitrification for cryo-EM. A density the size of DiC8-PIP_2 was found occupying the VBP, yet it appeared to take on slightly different conformations across two classes. In one class, the DiC8-PIP_2 density was closer to the TRP helix of TRPV1 (**Fig 1.11B**), similar to how full-length PIP_2 would bind (**Fig 1.10C**). In the other class, the DiC8-PIP_2 density was lifted into the VBP, further away from the TRP helix (**Fig 1.11C**), mirroring how agonists would normally engage TRPV1. The two DiC8-PIP_2 conformations had distinct impacts on the pore profile of the channel. In the first class, the architecture of the pore was similar to unliganded structures. We therefore assigned this conformation as resting or closed. The other class, however, was unique from agonist-bound structures, in that its S6 helix was more dramatically tilted, allowing for an increase in the opening at the selectivity filter while simultaneously narrowing the lower gate (**Fig 1.11E-G**). We referred to this novel conformation as the "dilated state" of TRPV1.

Interestingly, the two classes differed in abundance. The resting form was far more prevalent, with ~218,000 particles in its final reconstruction. The dilated form was less common, having only ~26,000 particles. In summary, in the presence of DiC8-PIP$_2$, TRPV1 was observed to adopt an open-like conformation, in addition to a closed one.

We next wondered whether DiC8-PIP$_2$ could be combined with purified protein in functional assays to show activity. We reconstituted TRPV1 into liposomes containing the same lipid composition as done with nanodiscs (molar-ratio 55.2% DOPC, 36.8% POPG, and 8% cholesterol), keeping its resident lipid intact. We then pulled inside-out patches and applied voltage steps, both in the presence of DiC8-PIP$_2$ and with the inhibitor AMG-9810 co-applied (**Fig 1.12A**). We did not see any activity at more typical membrane potential steps (-100 mV to +100 mV). By increasing the membrane potential up to +200 mV, we were eventually able to record currents directly evoked by DiC8-PIP$_2$, however small in amplitude they were (**Fig 1.12B-C**). These currents were effectively abolished in the presence of antagonist (**Fig 1.12B-C**). Like other agonists, the activity of DiC8-PIP$_2$ was rectifying, in that we observed currents in the positive half of the voltage spectrum but not the negative half (**Fig 1.12C**). This confirmed that PIP$_2$ could behave as a direct agonist and was consistent with the insights gathered from our structural analysis.

Discussion

While it is clear that the signaling molecule PIP$_2$ interacts with TRPV1, the literature is mired with controversy when it comes to the direction of said effect. Some studies suggest that PIP$_2$ may have direct agonist activity, but at the very least should potentiate the currents evoked by other activators. Others have argued that PIP$_2$ serves an inhibitory role, making it harder for

45

the channel to open. Our work here may offer a way to make sense of this discrepancy.

Most studies, especially those that have reported potentiating effects of PIP_2[59–61], have used short-form PIP_2, or DiC8-PIP_2, as a surrogate for full-length PIP_2. In the present work, we observed that short-form PIP_2 activated TRPV1 in purified proteoliposomes. Not only is this result consistent with heterologous studies, but it goes one step further by demonstrating direct ligand action on the channel. It rules out the possibility that DiC8-PIP_2 may trigger second-messenger or off-target pathways to activate TRPV1, because there simply was no cellular environment involved in the experimental design. Consistent with the function, structural analysis revealed that short-form PIP_2 led to the adoption of a more dilated pore configuration. Furthermore, short-form PIP_2 was seen binding to the VBP in a way that was more akin to other agonists, like capsaicin and RTX, than to lipids. Given this, it is probably better to think of short-form PIP_2 more as a small-molecule activator of TRPV1 and not as an exact replacement for a full-length lipid.

Compared to other agonists though, short-form PIP_2 seems to be relatively weak. The TRPV1 currents it could elicit were at best ~50 pA (recall from Chapter 1 Part 1 that we could measure up to 250 pA responses to capsaicin in the same recording system) and were only present at higher membrane potentials of over 150 mV. This result may be explained by the structures we obtained. Short-form PIP_2 was found to engage TRPV1 in one of two conformations. The majority (90%) of the particles adopted the channel's resting state. Only a minority (10%) of particles were in the dilated state. These proportions suggest that, while the central pore may become larger and more conductive to ions when TRPV1 binds to short-form PIP_2, it may not be the preferred outcome. Of course, we are equating the dilated state with the open state, but even this comparison may not representative. In the dilated state, the selectivity

filter was wider and should accommodate more ions, yet there remained a tight constriction point at its lower gate, which might ultimately serve as a barrier to ion permeation. Perhaps for these reasons short-form PIP_2 is better classified as a positive modulator of TRPV1 function, rather than a full agonist.

Meanwhile, setting aside all those publications that use short-form PIP_2, one finds that few groups have actually examined full-length PIP_2. We did not test full-length PIP_2 with electrophysiology in the present study. However, previous members of the Julius lab have already incorporated full-length PIP_2 into TRPV1 proteoliposomes. They showed a slight increase in capsaicin's EC50 and an increase in the threshold for temperature activation, which together reflect a downregulation of TRPV1 activity. Consistent with this, the structures bound to full-length PIP_2 obtained from this study were captured in the closed conformation. Still, this does not explain why the literature reports potentiating effects of PIP_2 in response to drugs that regulate PIP_2 synthesis and degradation. Since targeting kinases and phospholipases of PIP_2 may have broader repercussions on cell signaling, we wonder whether these drugs are truly selective in modulating PIP_2 levels and whether there may be other off-target effects at play. Further investigation is required to resolve this.

Figures
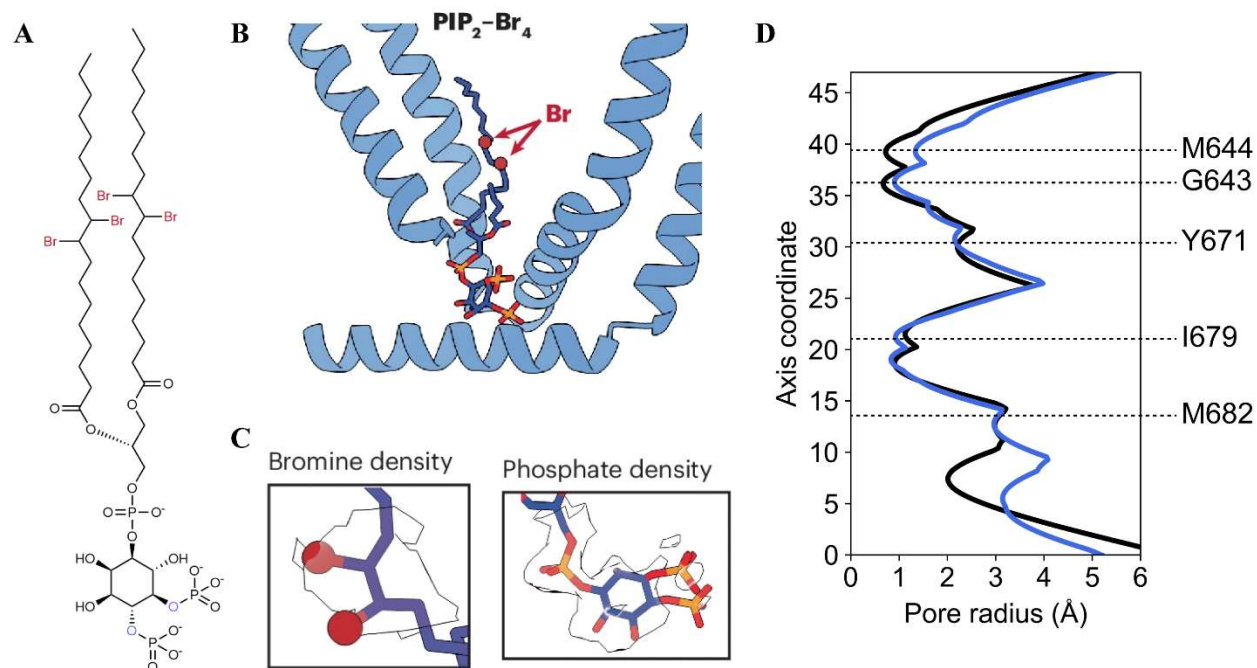
Figure 1.10 | Binding of brominated PIP₂ keeps TRPV1 closed
A) The chemical structure of brominated PIP$_2$ used in this study (generated by ChemDraw). **B)** Model of the VBP, highlighting binding of PIP$_2$-Br$_4$. **C)** Density maps of key functional groups for PIP$_2$-Br$_4$, including bromine densities as a fiducial (left) as well as phosphate densities around the inositol head group (right). **D)** Pore radii for models of unliganded TRPV1 (from PDB 5IRZ, black) and TRPV1 bound to PIP$_2$ (blue), as determined by the HOLE program.
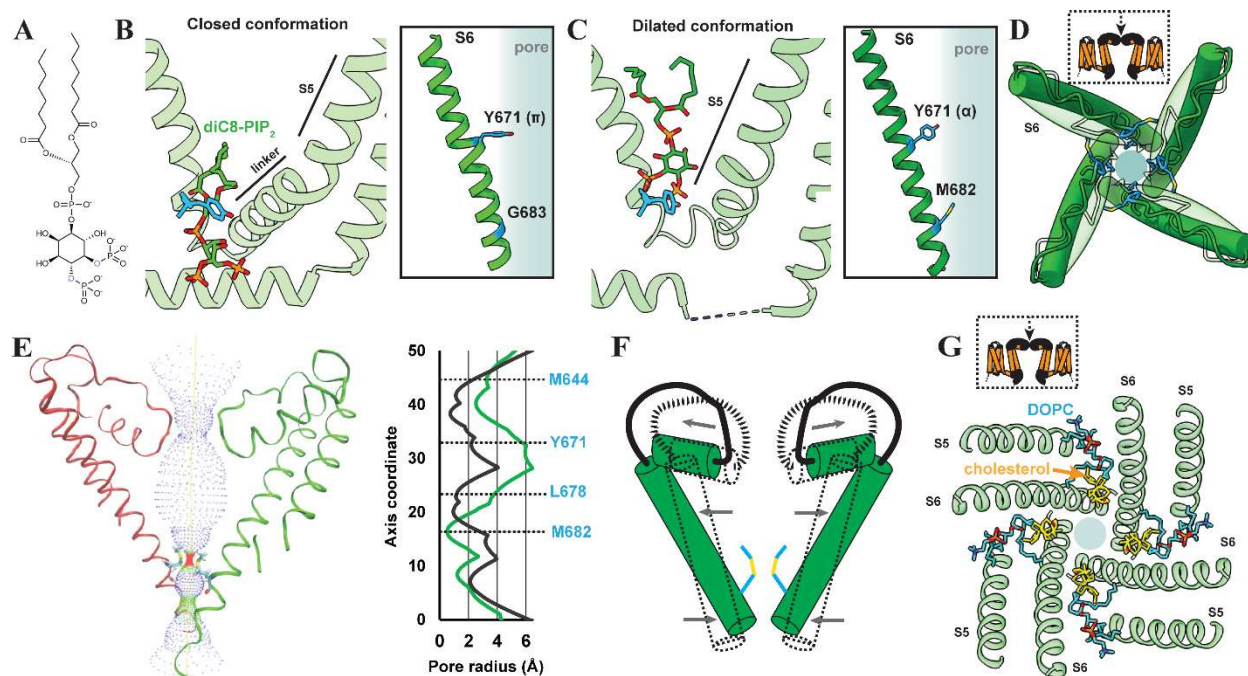
Figure 1.11 | DiC8-PIP₂ is a partial potentiator of TRPV1 activity, structural analysis
A) The chemical structure of DiC8-PIP₂ used in this study (generated by ChemDraw). **B,C)** VBP with diC8-PIP₂ bound in the closed conformation (B) and the dilated conformation (C). **D)** Top-down view of the TRPV1 pore in the closed conformation (transparent green) and the dilated conformation (dark green). M644 (blue) of the selectivity filter is highlighted. **E)** Left: pore profile of TRPV1 in the dilated conformation. Right: pore radii of closed (black) and dilated (green) states, as determined by the HOLE program. **F)** Schematic of the pore movements demonstrating the dilation of the upper portion of the pore and constriction of the lower portion. **G)** Top-down view of TRPV1 showing the binding of DOPC (blue) and cholesterol (yellow).
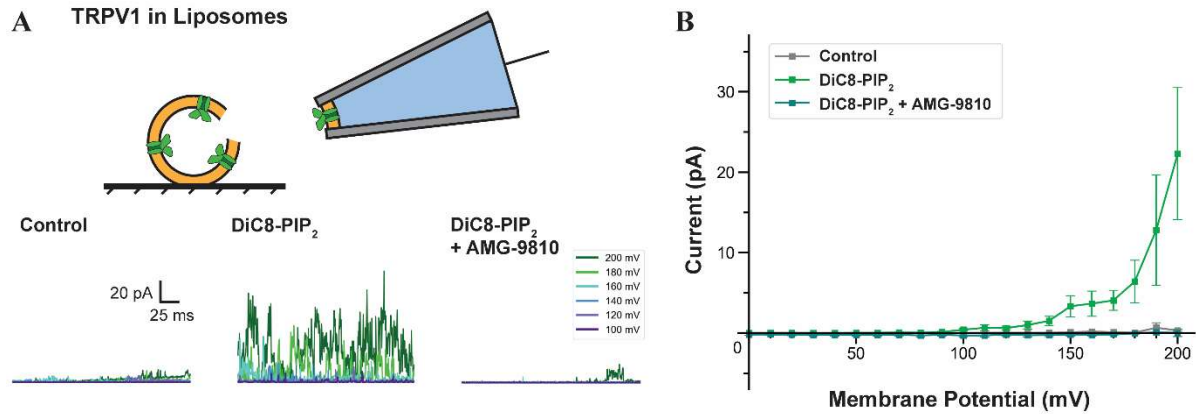
Figure 1.12 | DiC8-PIP₂ is a partial potentiator of TRPV1 activity, functional analysis
A) Top: schematic showing excised inside-out patch clamp recording configuration. Bottom: sample TRPV1 currents evoked by application of control (bathing) solution (left), 100 μM DiC8-PIP$_2$ (center), or 100 μM DiC8-PIP$_2$ plus 10 μM antagonist AMG-9810 (right). Applied membrane potentials varied between 100 mV and 200 mV according to the color key (far right).
B) Summary of current-voltage relationships showing that DiC8-PIP$_2$ reliably activates TRPV1. Data are graphed as mean ± SEM, patch clamp recordings n = 10.
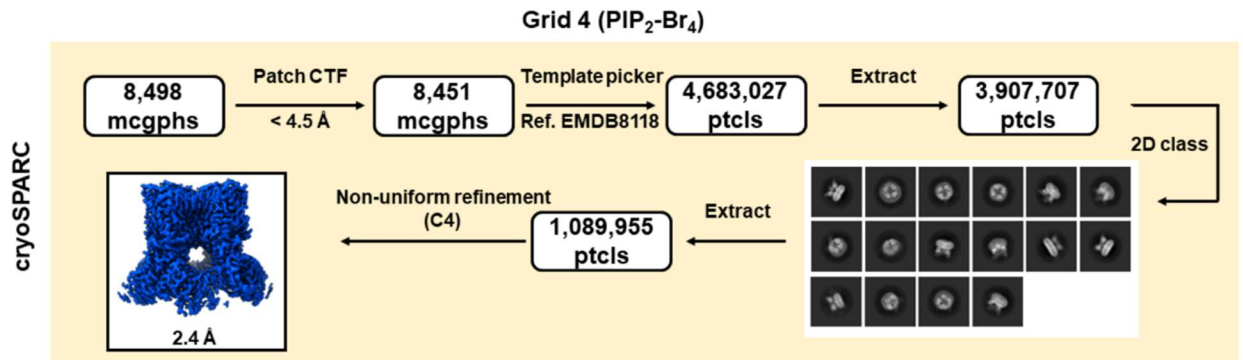
Figure S1.4 | Data processing scheme for TRPV1 with PIP$_2$-Br$_4$
Schematic shows data processing workflow, with picking, 2D classification, and 3D refinement all done in CryoSPARC.
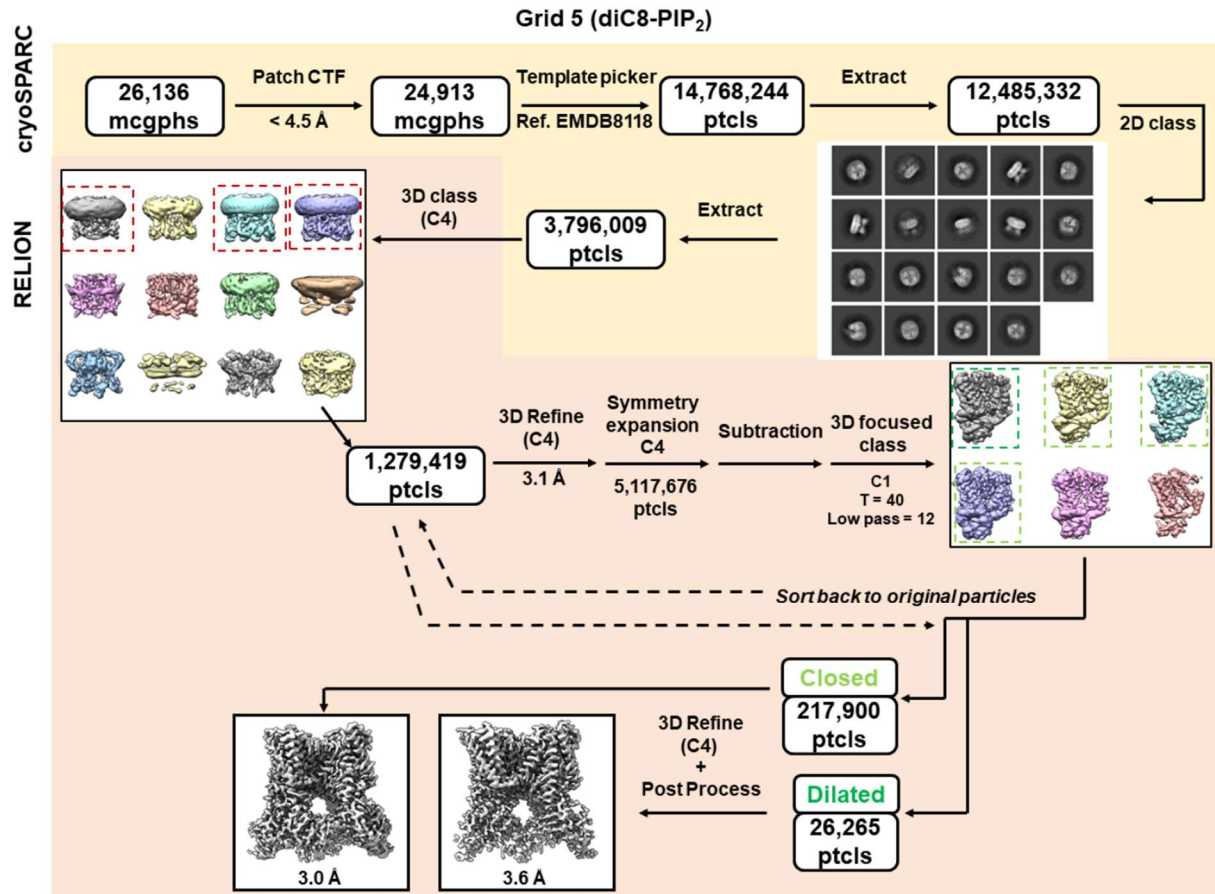
Figure S1.5 | Data processing scheme for TRPV1 with DiC8-PIP$_2$
Schematic shows data processing workflow, starting with picking and 2D classification in CryoSPARC, followed by 3D classification and 3D refinement in Relion.
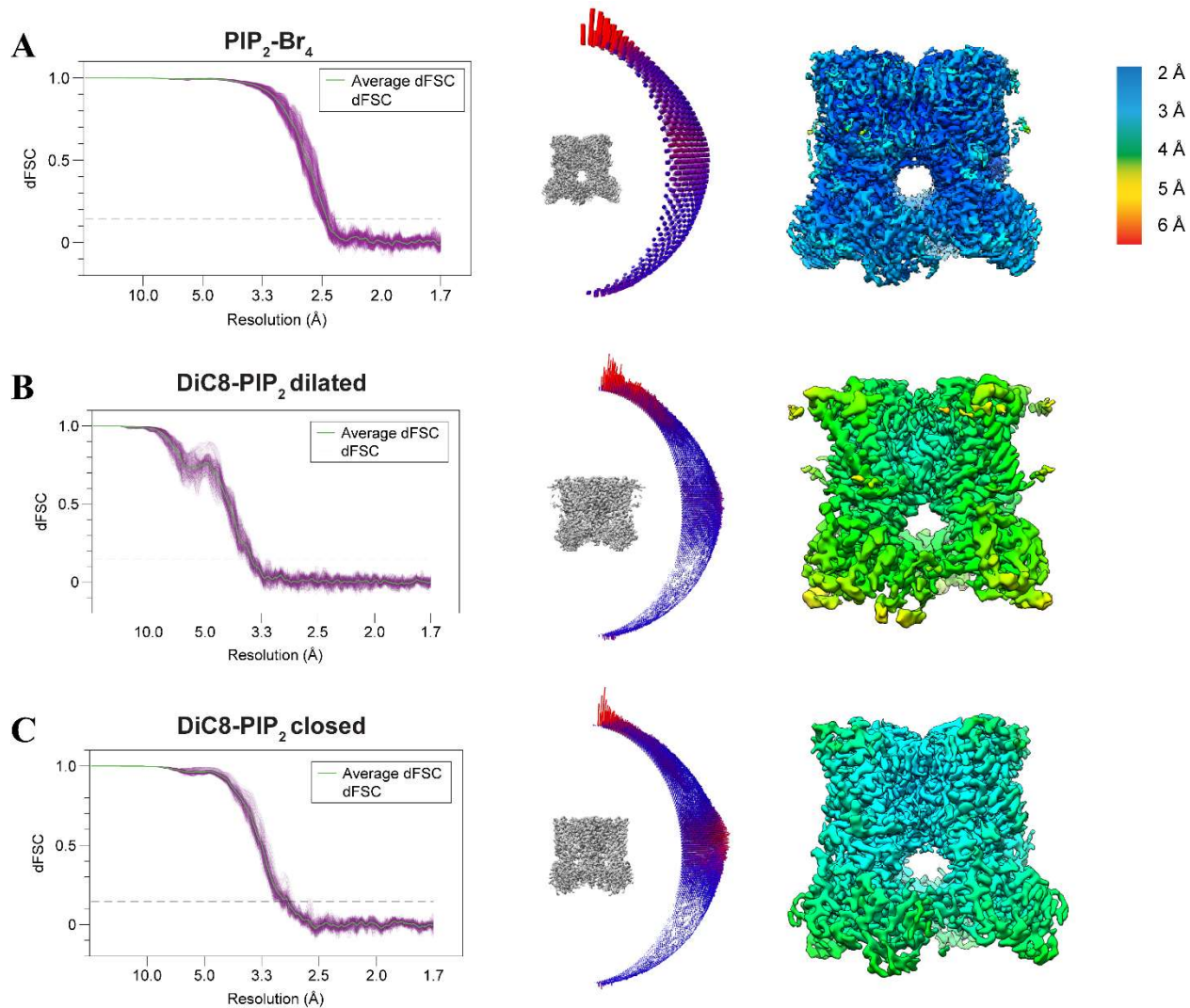
Figure S1.6 | Cryo-EM volume end parameters for TRPV1 bound to PIP₂ and to DiC8-PIP₂ samples, in dilated and closed states
From left to right: plots of dFSC curves, angular distributions, and local resolution (colored according to key in top right corner) for conditions of **A)** TRPV1 PIP₂-Br₄, **B)** TRPV1 DiC8-PIP₂ dilated state, and **C)** TRPV1 DiC8-PIP₂ closed state.

Table S1.2 | Parameters for reconstructions of TRPV1 with PIP2-Br4 and DiC8-PIP2.
Microscope data acquisition parameters and model parameters for the two datasets.

		PIP$_2$-Br$_4$ (Grid 4)	DiC8-PIP$_2$ closed	DiC8-PIP$_2$ dilated
Ascension Codes	PDB	8U43	8U30	8U2Z
	EMD	41873	41848	41847
Atoms	All	37,219	34,793	34,361
	Hydrogens	18,628	17,452	17,316
	Residues	2,224	2,112	2,040
Ligands	Na+	1	1	1
	DiC8-PIP$_2$ (PIO)	0	4	4
	Cholesterol (CLR)	0	0	4
	DOPC (PCW)	4	0	4
	PIP$_2$-Br$_4$ (V5H)	4	0	0
RMSZ deviation	bond length (Å)	0.32	0.28	0.30
	bond angle (°)	0.55	0.48	0.55
Validation	Clash score	4	6	8
	Poor rotamers (%)	4	0	1
Ramachandran	Favored (%)	94	94	92
	Allowed	6	6	8
	disallowed	0	0	0
Microscope	Microscope ID	UCSF		
	Magnification	105,000 ×		
	Voltage (KV)	300		
	Dose rate (e$^-$/pix/s)	16		
	Dose (e$^-$/pix/frame)	0.57		
	Total dose (e$^-$/Å)	45.8		
	Defocus range (μm)	0.5-2.0		
	Pixel size (Å)	0.835		
Data processing	micrographs	8,498	26,136	
	initial particles	1,089,955	3,796,009	
	final particles	1,089,955	217,900	26,265
	Box size (pix)	416	384	
	Symmetry	C4	C4	
	Map resolution (Å)	2.4		3.6
	FSC threshold	0.143	0.143	
	Map sharpening	CryoSPARC	RELION	
	b-factor	-114.7	-112.4	-113.5

Methods

Materials

Reagents were purchased from Sigma-Aldrich unless noted below. 1,2-dioctanoyl-sn-glycero-3-phospho-(1′-myo-inositol-4′,5′-bisphosphate) (DiC8-PIP$_2$), 1,2-dioleoyl-sn-glycero-3-phospho-(1'-myo-inositol-4',5'-bisphosphate) (PI(4,5)P$_2$ or PIP$_2$), soy extract polar, 1,2-dioleoyl-sn-glycero-3-phosphocholine (DOPC), and 1-palmitoyl-2-oleoyl-sn-glycero-3-phospho-(1′-rac-glycerol) (POPG) were purchased from Avanti Polar Lipids. The detergent n-dodecyl-β-D-maltopyranoside (DDM) was purchased from Anatrace. Bio-beads SM2 was purchased from Bio-Rad. Freestyle 293 Expression Medium and Expi293 Expression Medium, along with Expi-293F cells and the ExpiFectamine-293 Transfection Kit, were purchased from Gibco. Sf9 and insect cell culture media were purchased from Expression Systems. Fetal bovine serum was purchased from PEAK, and bovine calf serum was purchased from HyClone. HEK-293 GnT-cells and HEK-293T cells were purchased from ATCC. DH5α competent cells were purchased from New England Biolabs. Quantifoil R1.2/1.3 Au 300 mesh grids were purchased from Quantifoil Micro Tools GmbH.

Brominated Lipid Synthesis

The brominated species (1R,2R,3S,4R,5R,6S)-4-(((3-((9,10-dibromooctadecanoyl)oxy)-2-(((9,10-dibromo-octadecanoyl)oxy)methyl)propoxy)oxidophosphoryl)oxy)-3,5,6-trihydroxycyclohexane-1,2-diyl bis(phosphate) – i.e. PIP$_2$-Br$_4$ – was synthesized from PIP$_2$ using Br$_2$ as previously described[66]. 0.5 mg PIP$_2$ was dissolved in 0.5 ml chloroform and stirred on ice in a glass vial. Br$_2$ (stoichiometric with the number of double bonds in the lipid) was added to the vial with a glass syringe. The vial was flushed with argon and sealed. The reaction was allowed

to continue in the dark with stirring for 1 h. Solvent and any excess bromine was removed by application of vacuum in the dark overnight. Brominated lipids were stored at −80 °C until use.

Protein Purification and Nanodisc Reconstitution

Recombinant minimal functional rat TRPV1 (residues 110-603 and 627-764) with a maltose-binding protein (MBP) tag was expressed in HEK-293 GnTi- cells and purified as previously described[21] with the following general modifications. HEK-293 GnTi- cells were transfected with a baculovirus system for 48 h before collecting and freezing the resulting cell pellet. The cell pellet was suspended in Buffer A containing 150 mM NaCl, 25 mM HEPES pH = 7.5, and 0.4 mM tris(2-carboxyethyl) phosphine (TCEP)·HCl. The suspension was diluted two-fold with Buffer B containing 150 mM NaCl, 80 mM HEPES pH = 7.5, 0.5 mM TCEP·HCl, 20% glycerol and 29.4 mM DDM and allowed to incubate at 4 °C for 2.5 h. The homogenate was centrifuged at 100,000xg in a Beckman LE-80 Ultracentrifuge for 45 min. The supernatant was applied to an amylose column and washed with 5× column volumes of Column Buffer (Buffer B diluted 50-fold with Buffer A). An additional wash step was incorporated where 5 μM capsaicin in column buffer was applied to the TRPV1–MBP-bound amylose column for 30 min, and subsequently the column was washed with Column Buffer ten times with 3× column volume at a time. In the end, TRPV1 was eluted with Column Buffer containing 20 mM maltose. Protein was then concentrated for nanodisc assembly.

The membrane scaffold protein, MSP2N2, for nanodisc reconstitution was expressed in *Escherichia Coli* as previously described[28]. Nanodisc reconstitution of purified minimal TRPV1 with defined lipid composition was performed following the protocol described previously[28] with the following modifications. Nanodiscs were assembled with a 1:20:674 ratio of TRPV1–

MBP:MSP2N2:lipid. Lipids were combined with MSP2N2 for 30 min on ice before adding TRPV1–MBP to this mixture for another 30 min. Bio-Beads SM2 (0.5 g/mL) were added to the mixture and allowed to incubate overnight at 4 °C with gentle rotation. Tobacco etch virus (TEV) protease (27:1 w:w TRPV1–MBP:TEV) was added to the mixture for 3 h before purifying the nanodiscs using size exclusion chromatography (AKTA) using a Superdex 200 column. The TRPV1-nanodisc peak was concentrated to 2.1 mg/mL for cryo-freezing on grids.

For empty-pocket TRPV1 nanodiscs and for DiC8-PIP$_2$-bound TRPV1 nanodiscs, the lipid mixture used was (by mol%) 55.2% DOPC, 36.8% POPG and 8% cholesterol. For brominated PIP$_2$-bound nanodiscs, the lipid mixture was adjusted to 49.2% DOPC, 32.8% POPG, 10% brominated-PIP$_2$, and 8% cholesterol, to accommodate the lipidic species.

Cryo-EM Sample Preparation and Data Acquisition

To prepare cryo-EM grids, 3 µl TRPV1-nanodiscs were applied to glow-discharged Quantifoil R1.2/1.3 Au 300 mesh grids covered in holey carbon film (Quantifoil Micro Tools GmbH) and blotted with Whatman 1 filter paper on a Vitrobot Mark IV (FEI Company) with a 4.5 s blotting time, 4 blot force and 100% humidity, and subsequentially plunge-frozen in liquid ethane cooled by liquid nitrogen. Samples were imaged with a Titan Krios microscope (ThermoFisher FEI) operated at 300 kV and equipped with a post-column Bio Quantum energy filter with zero-loss energy selection slit set to 20 eV and a K3 camera (Gatan) either at the University of California, San Francisco (UCSF) or using the Cryo-EM Consortium at Stanford SLAC (S^{2}C^2) as stated below. Data collection was carried out with SerialEM[67] software. The detailed collecting parameters, including dose rate, total dose, total frames per movie stack and so on, are summarized in **Tables S1.1** and **S1.2**. Specific conditions not stated above for each of

the samples are described below.

Empty-pocket TRPV1 at 4 °C (grid 1). Empty-pocket TRPV1-nanodisc (described above) was kept on ice before applying to grids in a Vitrobot kept at 4 °C during grid preparation. Data were collected at S^2C^2 using TEM Gamma.

Empty-pocket TRPV1 at 25 °C (grid 2). Empty-pocket TRPV1-nanodisc was kept on ice and briefly warmed to room temperature for 5 min before applying to grids in a Vitrobot equilibrated at 25 °C. Data were collected at S^2C^2 using TEM Beta.

PIP$_2$-Br$_4$ (grid 4). TRPV1-nanodisc containing brominated phosphoinositide was kept on ice and applied to grids using a Vitrobot equilibrated at 25° C. Data collected at UCSF.

DiC8-PIP$_2$ (grid 5). DiC8-PIP$_2$ was dissolved in buffer containing 150 mM NaCl, 20 mM HEPES pH = 7.5, and 0.1 mM TCEP·HCl to a stock concentration of 1 mM. DiC8-PIP2 was applied to TRPV1-nanodiscs to a final concentration of 50 µM for 30 min on ice before applying sample to grids using a Vitrobot equilibrated at 15 °C. Data were collected at UCSF.

Image Processing

Cryo-EM data processing is illustrated in **Figures S1.1**, **S1.2**, **S1.4**, and **S1.5**. Directional Fourier shell correlation (dFSC) curves, angular distribution plots, and local resolution maps are provided in **Figures S1.3 and S1.6**. In general, motion correction on movie stacks was processed on-the-fly using MotionCorr2[68] in Scipion and binned 2×2 with Fourier cropping to 0.835 Å per pixel (UCSF Krios) or to 0.68 Å per pixel (S^2C^2). Dose-weighted micrographs were visually inspected to remove bad micrographs before further processing by CryoSPARC[69]. Patch-based CTF estimation was performed in CryoSPARC. Micrographs with estimated CTF fit resolution

poorer than 4.5 Å were discarded. EMD-8118 (apo TRPV1 in nanodisc) was used to make 25 templates for template picking. Picks were extracted and binned 4×4 by Fourier cropping and reference-free two-dimensional (2D) classification was used to remove non-TRPV1-nanodisc picks. Extracted particles were then subjected to reference-based 3D classification (ref. EMD-8118, low-pass filtered 12 Å) in RELION[70] to remove low-resolution and featureless particles. Further processing for each dataset continued as stated below. Resolutions were determined according to the gold-standard Fourier shell correlation of 0.143 criterion[71].

Empty-pocket TRPV1 4 °C. Particles were enriched for high-resolution features using symmetry expansion followed by focused classification as previously described[72]. Specifically, particles were refined using 3D Auto Refine with C4 symmetry in RELION using EMD-8118 as a reference (low-pass filter 12 Å). These refined particles were symmetry-expanded using C4 symmetry, and a mask focused on the VBP was used for background subtraction, followed by 3D classification on the symmetry-expanded particles. Classification parameters: ref. EMD-8118 (no low-pass filter), regularization parameter $T = 80$, symmetry C1, no image alignment. Particles without defined vanilloid pocket features were discarded. Particles containing monomers with four distinguishable pockets were than taken to CryoSPARC for nonuniform refinement (C4 symmetry) and then sharpened in PHENIX[73] using half-map sharpening. Final resolution was 2.9 Å.

Empty-pocket TRPV1 25 °C. Selected particles from 3D classification were refined in CryoSPARC using nonuniform refinement and C4 symmetry. Final resolution was 3.7 Å.

PIP$_2$-Br$_4$. Particles selected from 2D classes were extracted and then refined using CryoSPARC reference-based (EMD-8118) non-uniform refinement. As the sample is very homogenous, 3D classification did not improve data quality, and so was not used in

the final data. Map resolved to 2.4 Å

DiC8-PIP$_2$. Particles were refined in RELION using EMD-8118 as a reference low-pass filtered to 12 Å. Particles were then subjected to the symmetry expansion and focused classification regiment as stated above (regularization parameter T = 40, reference low-pass filtered to 12 Å, no image alignment). Low-resolution particles were excluded and two conformations of diC8-PIP$_2$ emerged, a closed conformation and a dilated-state conformation. Particles containing all four monomers containing either diC8-PIP$_2$ in the closed state or in the dilated state were taken further for refinement in RELION (reference EMD-8118, low-pass filtered 12 Å) and then sharpened using Post Process in RELION. The final resolution for closed was 3.0 Å and for dilated 3.6 Å.

Model Building

Resting TRPV1 (PDB-7L2P) or TRPV1-RTX (PDB-7MZD) was used as the starting model and docked into the sharpened maps using UCSF Chimera[74], followed by manual adjustment based on the resolvable features of the maps. PDB and molecular restraint files for ligands were generated in Phenix[73] using eLBOW, and then manually docked into the ligand densities. For the general 'resident lipid', di-palmitoyl phosphatidylinositol was used as the starting structure and the tails were shortened to fit the resolvable density. Models were refined using several iterations of Phenix Real Space Refine and manual adjustments in COOT[75]. The quality of the refined models was determined using the wwPDB validation server[76].

Pore Radius Determination and Structural Figures

The pore radii were determined using the HOLE[77] program and plotted in Excel. All

other structural figures were made using UCSF ChimeraX[78,79] and Adobe Illustrator.

TRPV1 Proteoliposome Preparation

Defined-lipid liposomes were prepared as reported previously[17]. Minimal functional rat TRPV1 with an N-terminal 8xHis-MBP tag was expressed in Expi-293F cells for 2 days using the ExpiFectamine-293 Transfection Kit. Transfected cells were then collected by centrifugation at 3,000xg for 10 min at 4 °C, with the supernatant decanted and cell pellets flash-frozen in liquid nitrogen and stored at −80 °C until use. To purify TRPV1, pellets were thawed and resuspended with buffer containing 200 mM NaCl, 50 mM HEPES pH = 8, 2 mM TCEP, 10% glycerol and protease inhibitors (Pierce tablet). 20 mM DDM (Anatrace) was added to extract TRPV1, while incubating on a rotator for 2 h at 4 °C. Samples were spun at 20,000xg for 1 h at 4 °C, with the supernatant being collected, filtered at 0.2 µm and combined with ~1 mL amylose resin (New England BioLabs) for at least 1 hour of affinity binding. Beads were poured over a Poly-Prep column (Bio-Rad) and washed with ~20 ml purification buffer (containing 200 mM NaCl, 50 mM HEPES pH = 8, 2 mM TCEP, 10% glycerol, 1 mM DDM and 10 µg mL^{-1} defined lipid mixture) to remove impurities. TRPV1 was eluted with purification buffer plus 20 mM maltose.

Additional defined lipid mixture was dried down under nitrogen gas and stored in a vacuum desiccator one day before the liposome prep. The dried lipid was dissolved in buffer containing 200 mM NaCl, 5 mM MOPS pH = 7 and 2 mM TCEP, to achieve a final concentration of 5 mg mL^{-1}. The lipid stock was left to sit for 30 min, sonicated for 10 min and subjected to ten freeze–thaw cycles with liquid nitrogen and hot water to ensure lipid dispersion. Lipids were further destabilized by addition of 4 mM DDM and left to rotate for 30 min at room temperature. The resulting lipid–detergent stock was combined with eluted TRPV1 to achieve

the desired 1:5 protein-to-lipid mass ratio and left to equilibrate for 1 h at room temperature on a rotator. Bio-Bead SM-2 resin was then added in four doses (60 mg, 60 mg, 150 mg, 300 mg per 10 mg lipid sample) with 1 hour room-temperature rotator incubations in-between. After the last Bio-Bead incubation, the mixture was left overnight (over 15 h) and transferred to a 4 °C rotator. The next day, Bio-Beads were removed by a Poly-Prep column (Bio-Rad) and washed with a small volume of minimal buffer (containing 200 mM NaCl and 5 mM MOPS pH 7). Liposomes were pelleted at 100,000xg for 1 h at 4 °C. Liposome pellets were resuspended in 200 µl of minimal buffer, divided into 13 µl aliquots, flash-frozen in liquid nitrogen and stored at -80 °C until use.

The default composition of defined lipids used in most experiments was (by mol%) 55.2% DOPC, 36.8% POPG and 8% cholesterol, consistent with the nanodisc reconstitution experiments. Sometimes, 100% soy extract polar was used, and those experiments were specifically indicated.

Liposome Electrophysiology

Liposome electrophysiology was performed as previously described[17]. The day before a patch clamp session, one aliquot of frozen liposomes was thawed, supplemented with an equal volume of minimal buffer (containing 200 mM NaCl and 5 mM MOPS pH = 7) plus 40 mM sucrose, plated on a glass coverslip and dehydrated in a vacuum desiccator for at least 50 min. 100 µL of minimal buffer were added to the dried liposomes to rehydrate them overnight. Before patching, 5 µL of rehydrated liposomes were pipetted onto additional coverslips with 100 µL of minimal buffer on them and left still for 2 hours to allow liposomes to adhere to the glass.

Bathing solution was delivered by gravity perfusion and contained 140 mM NaCl, 5 mM

KCl, 20 mM HEPES pH = 7.6, and 2 mM $MgCl_2$. Internal solution was kept identical to bathing solution. Pipette tips were pulled from BF150-86-10 borosilicate capillaries (Sutter Instruments) using a P-97 micropipette puller (Sutter Instruments) and fire-polished using a MF-830 microforge (Narishige), keeping tip resistances between 3 and 10 MΩ. Coverslips with liposomes were transferred to an IX71 inverted microscope setup (Olympus). The electrode tip was pressed up against a liposome using an MP-285 micromanipulator (Sutter Instruments), and pressure was applied orally until a giga-ohm seal was achieved. The tip was then slowly retracted until just a patch of membrane was retained, accessing the inside-out patch configuration. The patch was then placed in front of the SmartSquirt microperfusion system (AutoMate Scientific) to apply chemical ligands, or in front of a Cool Solutions Heat/Cooled Temperature Control system (AutoMate Scientific) to apply temperature ramps. For pharmacology experiments, voltage steps were applied between −120 mV and +120 mV or, if needed, between −200 mV and +200 mV, in 10 mV increments. For temperature ramp experiments, voltage was maintained at +100 mV throughout the recording. Voltages commands were sent and currents were measured via an AxoPatch 200B amplifier (Molecular Devices) and a Digidata 1550B digitizer (Molecular Devices), controlled by pClamp software (Molecular Devices). Signals were acquired at 20 kHz and filtered at 5 kHz. Data were analyzed post hoc in pClamp (Molecular Devices), Excel (Microsoft) and custom-made Python scripts.

Electrophysiology Analysis

Electrophysiological data are presented as mean ± standard error of the mean (SEM) unless otherwise noted.

For pharmacology experiments, current-voltage relationships were obtained by taking the

average current in the last 100 ms of a depolarizing/hyperpolarizing step and plotting it against its membrane potential, across all membrane potentials sampled. For most experiments, passive leaks were not subtracted. For DiC8-PIP$_2$ experiments in particular, TRPV1-specific currents were defined well enough that it was possible to subtract the leak of the patch – we estimated the leak as the lowest magnitude peak in an all-point histogram of current amplitude in a given potential, and subtracted that from the mean current measured over the given potential.

For heat ramp experiments, temperature activation data were collected as current over time and temperature over time. Patch leak was not subtracted. For larger macroscopic currents, data from each experiment were then simply re-plotted as current against temperature. The data were then normalized such that the current at 45°C was set to 1, allowing us to average data across multiple experiments despite differences in absolute current magnitude. Arrhenius plots were generated from averaged data by plotting log base 10 of the normalized current value against the temperature inverse times 1000, i.e. 1000/T, where temperature was in Kelvin. The result was a plot where the data could be approximated by two trendlines (format y = a*x + b). The intersection of those trendlines was taken as the temperature threshold for activation. The Q_{10} value is defined as[80]:

$$Q_{10} = (\frac{k_2}{k_1})^{\frac{10}{T_2 - T_1}}$$

We took the endpoints of each trendline and used those to fill in values for k_2, k_1, T_2, and T_1 to calculate Q_{10}, before and after the threshold for temperature activation.

For smaller amplitude temperature activation – or so called "mini events" – data, it was not possible to simply plot current against temperature for each recording because the signal-to-noise (i.e. TRPV1 current against leak) was too low. Instead, TRPV1 events were identified by adjusting the baseline leak to 0 pA manually and using event detection software to detect all

current spikes exceeding a threshold of 12 pA, all of which was done in pClamp. For each current spike event *n*, its instantaneous frequency was then calculated as the inverse of the average inter-event interval between events *n* + 1 and *n* as well as *n* and *n* − 1, which simplifies to:

$$f = \frac{1}{\frac{(t_{n+1} - t_n) + (t_n - t_{n-1})}{2}} = \frac{2}{t_{n+1} - t_{n-1}}$$

For each current spike event *n*, the average temperature was calculated as the temperature averaged across all point used in the previous equation, that is:

$$T_{avg} = \frac{T_{n+1} + T_n + T_{n-1}}{3}$$

For all current spike events in a recording, the instantaneous frequencies were plotted against their corresponding average temperature, all in a single scatter plot. Events were then binned per 1°C, and the median of all events in each bin was calculated. That way, for each recording, we obtained a plot for the median instantaneous frequency of mini events as a function of temperature. Data from multiple recordings could then be averaged together to give the mean instantaneous frequency against temperature. Because sub-threshold values usually had instantaneous frequencies of 0, which are incompatible with logarithmic transformations, this data could not be converted to Arrhenius plots. Instead, threshold could be determined subjectively by seeing when the frequencies begin to deviate from 0.

Where used, statistical testing was carried out in Python. The applicability of parametric tests was first assessed, examining whether the data followed assumptions about equal variance (Levene's test) and normal distribution (Shapiro–Wilk test). Where either of these assumptions were violated, we used nonparametric tests, particularly a Mann-Whitney U test. For all tests, a priori, we set $\alpha = 0.05$ and represent statistical significance with the P value, as indicated in the

figure legends. We selected sample sizes for all experiments based on our laboratory and others'

experience with similar assays.

CHAPTER 2: DE-NOVO DISCOVERY OF TRPV1 TOXINS ENABLED BY CRYO-EM

Introduction

Pain is an adaptive response designed to protect the body from harm. However, when the experience persists in the absence of its initial stimulus, as in the case of chronic pain, it can be debilitating to one's well-being. There is thus an important need for pain management therapeutics, especially ones with less abuse potential than current opioid drugs[51,52]. Transient receptor potential, or TRP, channels have emerged as promising drug targets in the treatment of pain disorders, with the noxious heat and pain receptor TRPV1 standing out. Its ability to respond to stimuli associated with tissue damage and inflammation make it likely for its antagonists to suppress pain signaling. We may also gain therapeutic value from agonists, as they could activate TRPV1 just enough to desensitize their host sensory neurons and prevent further pain signaling[9,53].

A major source of untapped pharmacology comes from animal venoms. While their composition can be highly heterogeneous, venoms often contain specialized toxin proteins which evolved to target key molecules in physiology, particularly ion channels, usually for the purpose of predation or survival therefrom[81,82]. Over the years, several peptide toxins have been identified that act selectively on TRP channels, including TRPV1[19,20] and TRPA1[83]. These toxins, at their core, are variations of the inhibitory cystine knot (ICK) – a motif where three small β strands are stapled together by three cystine disulfide bonds to create a compact and stable peptide, all just under 5 kDa in size[84]. While there are estimated to be at least 10^5 unique ICK toxin sequences[85], identifying even a single one is not trivial. The typical route to discovery involves identification of positive-hit venoms through functional screening, followed by extensive biochemical separation and mass spectrometry to identify the active subcomponent. Alternatively, if one has access to the glands of the venomous critter, a cDNA library can be

generated and from it one can search for sequences homologous to known toxins. These workflows are time-consuming, resource-intensive, and require an adequate supply of venoms or else access to the glands that produce them[86]. They also do not provide immediate mechanistic insight as to how the discovered toxin can engage its target and how it achieves its functional impact.

Cryogenic electron microscopy (cryo-EM) is becoming the go-to method for high resolution structure determination, particularly for membrane proteins. In more recent years, optimization of grid technologies and data-processing algorithms have enabled analysis of samples that are far more heterogeneous[87]. The workflow is so sophisticated that one can now perform minimal biochemistry and still obtain high-quality structures. For instance, it is possible to apply crude cell lysates directly onto grids, instead of homogeneously purified protein samples, in what is termed "on-grid purification"[88,89]. Inspired by this, we wondered whether we could leverage cryo-EM to facilitate toxin discovery out of crude venoms, using purified TRPV1 as a tool to capture ligands from their heterogeneous source.

We screened a small library of venoms for their activity against TRPV1 and identified a handful of them that had activating effects. We then combined purified TRPV1 with crude venom from one positive-hit tarantula species, *Cyriopagopus lividus* (*C. lividus*), and advanced it to structure determination by cryo-EM. We could readily identify a bivalent ICK toxin, and there was indication of a monovalent one present as well. Both types of toxins were found to bind the extracellular pore loops of TRPV1, where they widen the selectivity filter as part of their activation mechanism. From this study, we demonstrate that cryo-EM can be used as an efficient means to identify 1) the active subcomponent of heterogeneous pharmacological mixtures, like venoms, along with 2) its mechanism of action. This methodology, while already fairly

streamlined, will only improve as cryo-EM hardware and software continue to be refined, hopefully one day allowing for reliable toxin sequence determination directly from the obtained density maps.

Results

We obtained a preliminary panel of twenty venoms from Dr. Volker Herzig's *Arthropod Venom Biobank* and screened them against TRPV1 transiently transfected into HEK-293 cells, using calcium imaging. Given that crude venoms are highly heterogeneous, we suspected that some their contents could act indirectly on our vehicle cells. Therefore, in parallel, we also tested each venom for their effects on another transiently-transfected TRP channel, TRPM8. At the end of each recording, we included either capsaicin or menthol for TRPV1 or TRPM8, respectively, to elicit the maximum calcium response. This allowed us to normalize all venom activity.

Six venoms were shown to activate TRPV1, but not TRPM8. Venom from *C. lividus* (**Fig 2.1A**) had one of the strongest effects on TRPV1, being close to equal in efficacity as capsaicin (**Fig 2.1B-E**, **Fig S2.1**), as did two other venoms, from *Omothymus Violaceopes* and *Lampropelma Spec.* (**Fig S2.2**). Two additional venoms had weaker but still real responses on TRPV1 – these came from *Poecilotheria Rufilata* and *Nebo Yemenensis* (**Fig S2.2**). Interestingly, venom from *Psalmopoeus Cambridgei* was also found to selectively activate TRPV1 (**Fig S2.2**). This was consistent with previous work from the Julius lab which discovered the vanillotoxins from this species[19], and gave us confidence in the results of our screen. (Venoms that did not yield any responses from either TRPV1 or TRPM8 are reported in **Fig S2.3**.)

We chose to focus our structural analysis on the venom from *C. lividus* (also called *Haplopelma lividum*). This species drew our attention because it lacked any documented link to

TRPV1. The literature reports that venom from *C. lividus* does contain μ-TRTX-Hl1a which can inhibit the sodium channel Nav1.8[90], as well as haplotoxin-1 and haplotoxin-2[91] which, according to patents filed by Alomone Preclinical Ltd[92], can also target the sodium channel Nav1.3. There are also anecdotal experiences about how *C. lividus* bites are extremely painful (plenty of them, actually, on online arachnophile forums), potentially implicating TRPV1 as a pharmacological target.

Our purification-amenable construct of TRPV1, which offers higher expression and stability, lacks distal parts of the N-terminus, C-terminus, and outer pore loops[21], which may play a role in toxin binding. We confirmed that our minimal TRPV1 construct was also responsive to *C. lividus* venom by calcium imaging (**Fig S2.4**). We then purified TRPV1, reconstituted it into nanodiscs, and combined it with *C. lividus* venom just before grid vitrification (see **Fig S2.5** for biochemical validation). To this mixture, we also applied protease inhibitor cocktail, as the venom might contain proteases that could interfere with the experiment. There is also a precedence for toxins to act as gating modifiers of TRPV1, in that they seem to stabilize the channel only after it enters the open state (even if only after spontaneous opening)[20]. Therefore, to maximize our odds of capturing a toxin-bound state, we also included the agonist resiniferatoxin (RTX).

Our initial consensus reconstruction suggested that there might be heterogeneity in the sample, so we pursued classification without alignment and without imposed symmetry (**Fig S2.6**). Our best classes were then combined and further refined to generate a structure that was C2 symmetric and reached a global resolution of 3.12 Å (**Fig 2.2A**). A closer examination revealed an ICK-like density sitting above the S6 helix and adjacent to the pore helix, for each monomer. These knot densities were linked in pairs, indicating that the putative toxin in *C.*

lividus was most likely a bivalent toxin, similar to double-knot toxin (DkTx)[20]. Next, we isolated the density for this bivalent toxin, docked the previously-solved model of DkTx into it (PDB ID 5IRX), and refined it – the result was a model that fit well the map and remained similar to DkTx (**Fig 2.2B-C**). By examining the pore profile, the bivalent toxin was observed prying open the selectivity filter of the channel, relieving the constriction points normally caused by glycine-643 and methionine-644 (**Fig 2.2D**). This is consistent with the mechanism of action of DkTx. The lower gate was also found to be open, likely a consequence of including RTX in the preparation (**Fig 2.2D**). (Additional volume parameters are described in **Fig S2.7**.)

While most particles were sorted into this double bivalent toxin class, other particles ended up in two alternative classes. The first class featured extra density for one bivalent toxin and two monovalent toxins, as there was only unambiguous density for one linker (**Fig 2.3A-B**). Meanwhile, in the second class, there appeared to be four monovalent toxins bound to TRPV1, without any discernible linkers between them (**Fig 2.3C-D**). This would suggest that there may exist single-knot toxins in *C. lividus*, in addition to the bivalent toxin. However, these two reconstructions do not reach the same high resolution as does the clear bivalent toxin class (only 3.79 Å and 3.59 Å, with C1 and C4 applied symmetry, for the first and second classes, respectively), especially locally within the toxin density (**Fig S2.8** and **Fig S2.9**). Furthermore, it is possible that these monovalent toxins reflect a bivalent toxin where the linker is not visible due to flexibility or damage. Further analysis is required to make confident statements about the existence of such monovalent toxins.

The bivalent toxin discovered by cryo-EM might very well be identical to DkTx. However, in the absence of information about its sequence, we cannot rule out the existence of other homologous bivalent toxins. We sent a sample of our crude venom for preliminary mass

spectrometry, but could only detect the hainantoxin U3-TRTX-Hhn1r (**Fig S2.10A-B**), which is a monovalent ICK toxin known to target sodium channels[93]. This could potentially be the identity of the monovalent toxin we observed, but it cannot account for the bivalent toxin. We next wondered if our structure was sufficiently high enough in resolution that we could predict the peptide sequence directly from it. After several iterations of DeepTracer[94], we could obtain a single polypeptide chain prediction that followed our density well. However, its sequence identity with DkTx was only ~7% (5 out of 75 residues), and it was missing several critical cysteines responsible for maintaining the ICK fold (**Fig S2.10D**). We took this sequence to AlphaFold[95,96] to predict its structure, but we could only generate a double α-helical peptide that failed to recapitulate the ICK folds we were expecting (**Fig S2.10C**). As a result, the precise identity of the toxins discovered in *C. lividus* remains unknown.

Finally, we wondered whether the same result could be obtained by preparing a sample in the absence of RTX. (That said, we still pre-incubated our crude venom with protease inhibitors to protect our purified TRPV1.) Our consensus reconstruction showed heterogeneity, so we performed classification without alignment and without imposed symmetry (**Fig S2.11**). We took our best classes and refined them together to yield a reconstruction that was C2 symmetric and reached a global resolution of 3.25 Å. In it, we clearly saw additional density near the outer pore loops of TRPV1 that resembled two bivalent toxins (**Fig 2.4A**, **Fig S2.12**). The bivalent toxin model we generated from our previous dataset still fit well within this new bivalent density. Interestingly, we also observed a class of particles in which there was no toxin density at all (**Fig S2.13**), something that did not happen in the sample where RTX was included. This suggested to us that the toxin might not be abundant enough in our crude venoms to saturate TRPV1 without some other ligands around to promote toxin binding. Pore profile analysis revealed that the

bivalent toxin pulled away glycine-643 and methionine-644 to open the upper gate (**Fig S2.4B-C**). The lower gate remained firmly shut by isoleucine-679, which made sense given the absence of a vanilloid compound (**Fig S2.4B-C**). Curiously, given the distances across the central pore and the presence of a π-helical bulge in the middle of the S6 helix, the TRPV1 model we generated for this bivalent toxin class without RTX was most consistent with the previously published pre-open DkTx state (PDB 7L2R), but not the related DkTx open states. In all, we could conclude that it was possible to identify toxins from *C. lividum* by having them bind to purified TRPV1 in cryo-EM, regardless of whether any additional agonist was applied to the sample. That said, adding orthogonal agonist can likely promote toxin engagement in a way that favors our ability to resolve it.

Discussion

As its methodologies continue to evolve, cryo-EM is becoming an increasingly versatile tool. Its ability to handle heterogeneous samples, both at the stages of grid preparation and data processing, has very important ramifications for drug discovery, where using pools of compounds in screening assays is preferred to accelerate throughput. Venoms are a promising source of therapeutics, and some very selective activators and inhibitors of ion channels have been identified from them. However, their availability can be limiting, plus they contain many bioactive molecules, the latter making it difficult to determine their active subcomponent without rigorous biochemistry.

We wondered if we could use cryo-EM as an straightforward tool to identify toxins that could act on ion channels from a crude venom and, in the process, infer their mechanism of action. We used TRPV1 as a model system, because of its therapeutic relevance and amenability

to cryo-EM. Out of a small library of 20 venoms, 6 were found to activate TRPV1 by calcium imaging. We could then take one of those venoms to structure determination and indeed see putative toxin density binding to the vanillotoxin binding site on the extracellular surface of TRPV1. Density from our best reconstruction appeared to suit a bivalent toxin, which was captured widening the channel's selectivity filter. This was comparable to the already identified DkTx. Moreover, some lower resolution structures were obtained that implied the existence of a monovalent toxin, too. This wealth of information could be obtained from very small amounts of venom - under 50 μg per condition, or ~4 μg per grid.

Taking this methodology to the next level, it would be optimal if we could use the structural information gathered here to directly predict the sequence of all identified toxins. While ambitious, in practice, this remains difficult to achieve. We used our best refined map to predict a sequence without any additional information. The result was at most 7% identical to DkTx. While this sequence could be real – after all, there is no need for the toxin found in *C. lividus* to fully match DkTx – its structure prediction by AlphaFold neither follows our density map nor our pre-existing knowledge regarding ICK toxins. DeepTracer probably requires higher resolution features than what was available to accurately discriminate between similarly-sized residues. The local resolution of the bivalent toxin in our sample is not too high after all, ranging from 2.8 Å nearer to TRPV1 up to 4.0 Å in the linker region. Further measures may be required, on both the data collection side as well with data processing, to push the resolution as aggressively as possible to facilitate sequence prediction. Being one day able to reliably capture sequence information of the identified toxins would render this cryo-EM pipeline truly transformative for the field of venomics and would have huge ramifications for the discovery of drugs against ion channels.
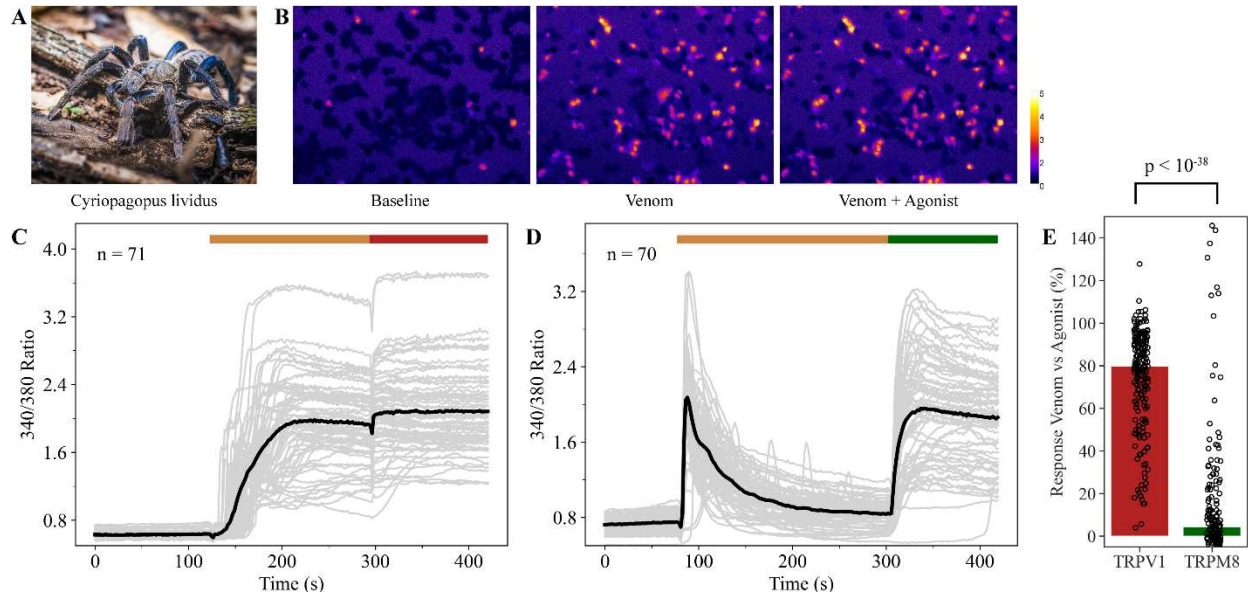
Figures

Figure 2.1 | Venom from *C. lividus* activates TRPV1 selectively
A) Image of *C. lividus*, also called the cobalt blue tarantula (borrowed from Wikimedia Commons[97]). **B)** Sample calcium imaging data for TRPV1-transfected HEK-293 cells. Left shows cells under baseline conditions (loaded with 10 μg/mL Fura-2AM, but no venom or agonist added), middle shows cell response to the addition of 0.2 μg/μL venom, right shows response to further addition of 10 μM capsaicin as a positive control. Data are shown as a heat map, brighter hues reflect higher 340/380 ratios, according to color key on the far right. **C)** Analysis of calcium imaging data for TRPV1-transfected cells, for a single replicate. Regions of interest were selected from the experiment shown in **B)** and the 340/380 ratios were measured as a function of time. Grey traces represent data for all regions of interest in view, the black trace represents the average of all grey traces. Orange bar reflects the period when 0.2 μg/μL venom was added, red bar reflects the period when venom and 10 μM capsaicin were co-applied. **D)** Analysis of calcium imaging data for TRPM8-transfected cells, for a single replicate. Similar to **C)** but using data for TRPM8 instead. Green bar indicates co-application of venom and 100 μM menthol. **E)** Summary plot showing spread of venom-evoked calcium responses normalized to the maximum response obtained by agonists. Data is the sum of three replicate imaging experiments for each condition. Each point is a region of interest, totaling n = 197 and n = 151 for TRPV1 and TRPM8, respectively. Bars show the median of each distribution. Statistical test used was Mann-Whitney U test, $p < 10^{-38}$.
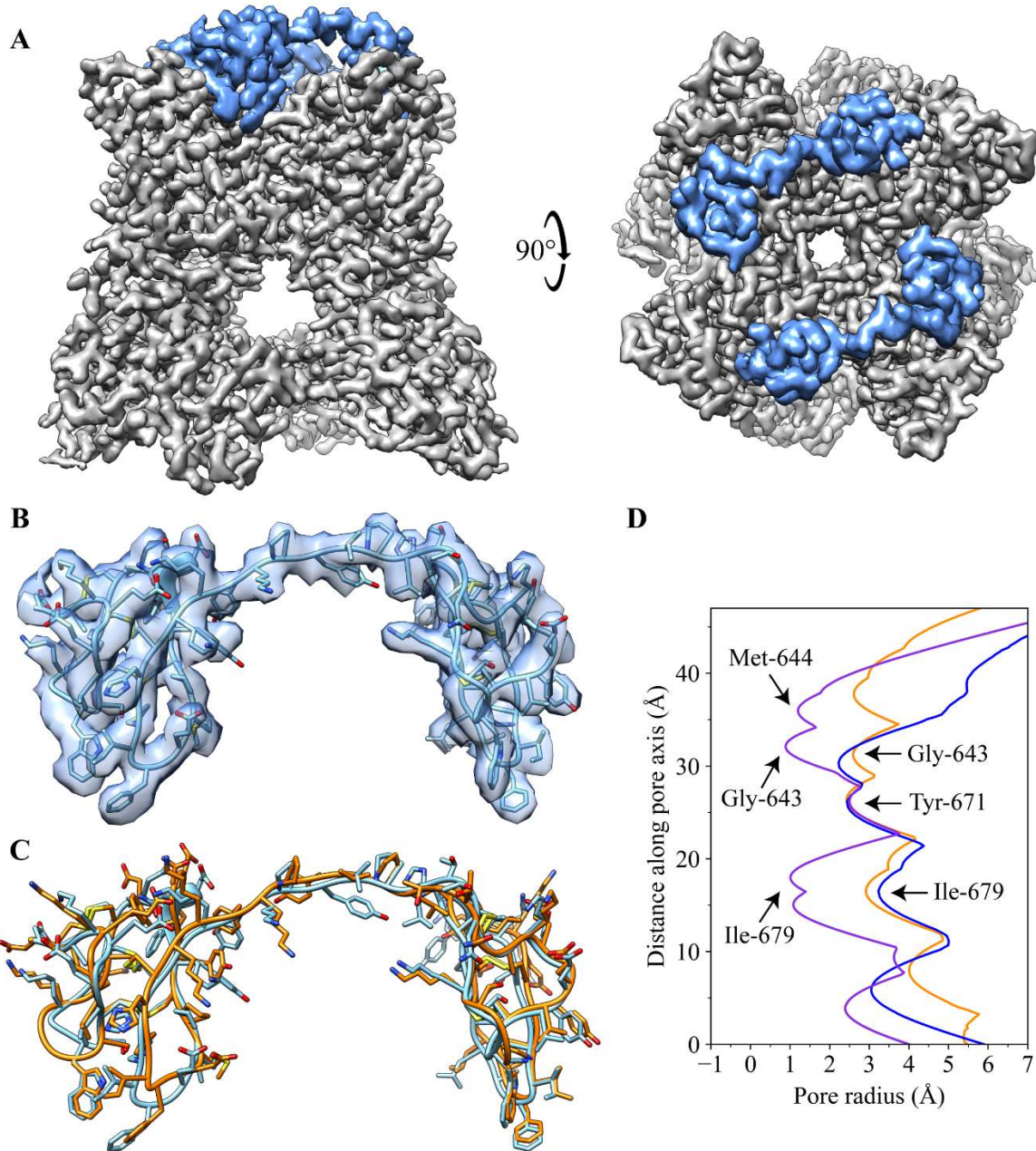
76

Figure 2.2 | Venom from *C. lividus* contains a bivalent toxin that binds to TRPV1

The best classes were refined together to give a final reconstruction featuring two unambiguous bivalent toxins bound to the extracellular face of TRPV1. **A)** Map of TRPV1 (grey) with extra density corresponding to bivalent toxins (blue), shown as a side view (left) and a top view (right). **B)** Isolated density for one bivalent toxin, with the model of DkTx (from PDB 5IRX) refined to fit within. **C)** Overlay of the refined PDB map from **B)** (in blue) and the original model of DkTx (from PDB 5IRX, in orange), showing overall similar architecture with small differences. **D)** Pore profile map determined by HOLE, comparing the pores of TRPV1 in the original DkTx/RTX structure (from PDB 5IRX, orange), the unliganded TRPV1 structure (from PDB 3J5P, violet), and the model refined from our double bivalent toxin reconstruction (blue).
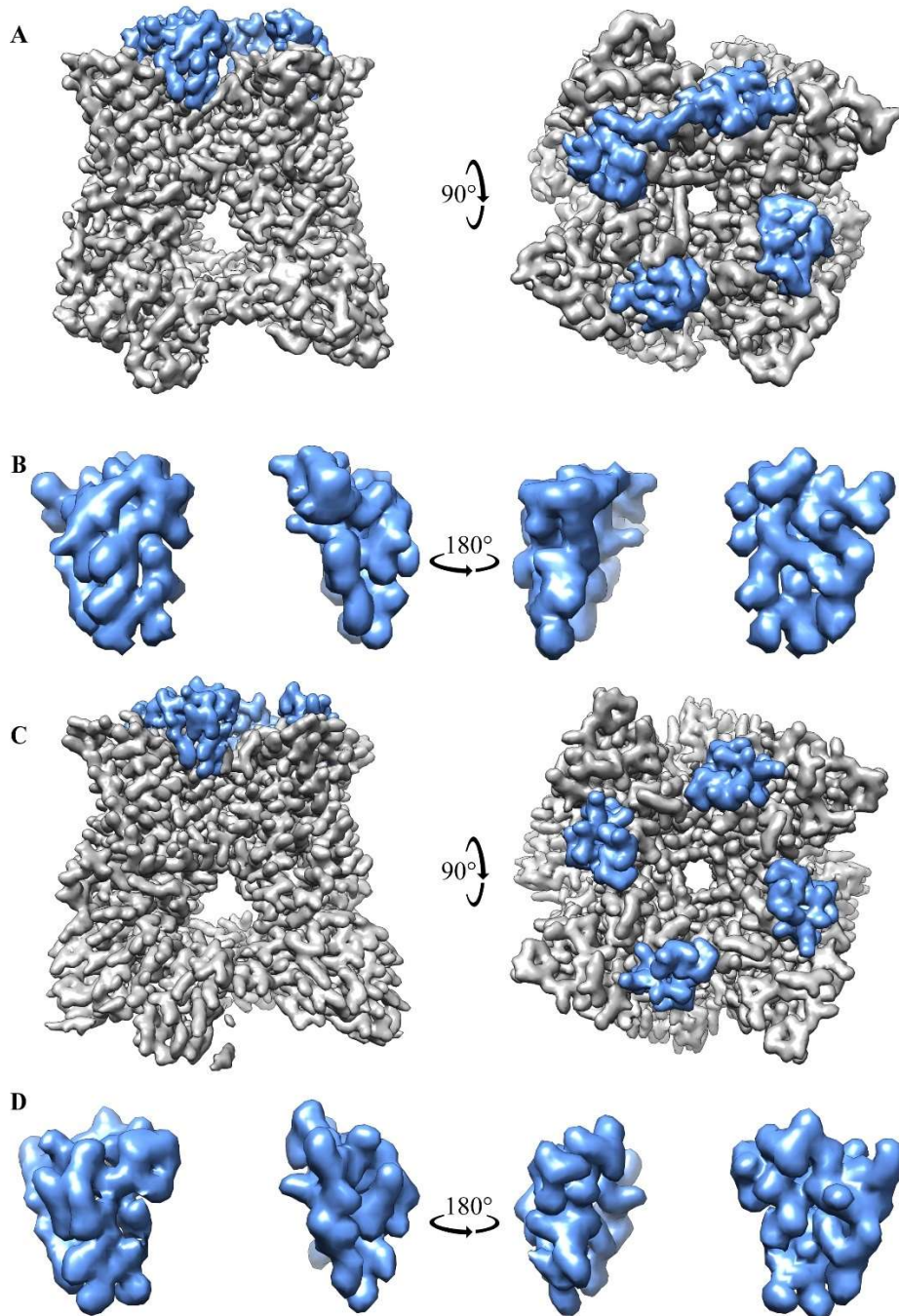
Figure 2.3 | Alternative reconstructions suggest potential existence of monovalent toxin in *C. lividus* venom

Two minor classes from 3D classification showed possible monovalent toxin. Maps in **A)** and **B)** came from the same class (#1) and appeared to have one bivalent toxin and two monovalent toxins. Maps in **C)** and **D)** came from the same class (#3) and appeared to have four monovalent toxins. In **A)** and **C)**, the toxin density is highlighted (blue) and shown on TRPV1 (grey), as a side view (left) and a top view (right). In **B)** and **C)**, only the toxin density is shown, as side views, both front (left) and back (right).
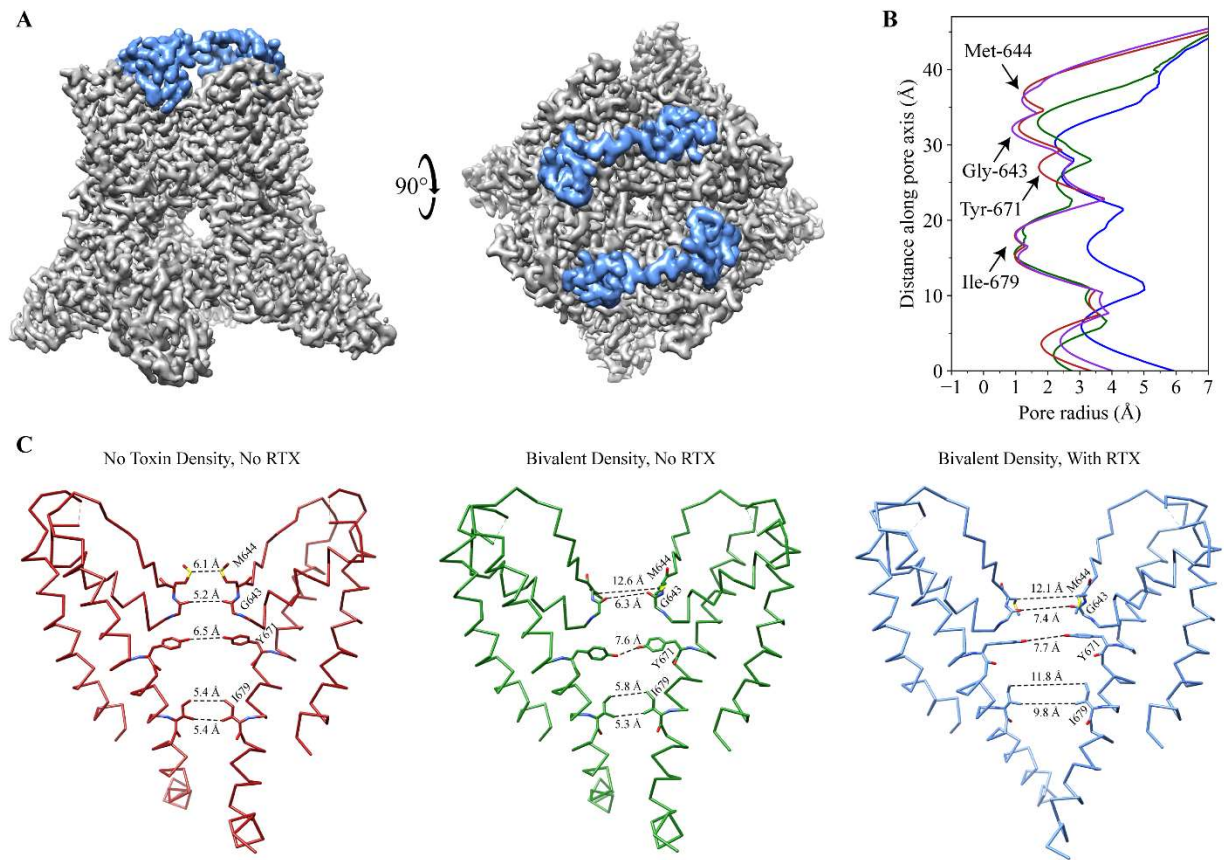
Figure 2.4 | Bivalent toxin from *C. lividus* can still be isolated without RTX incubation
If RTX is omitted from grid preparation, the best reconstructed class still shows two unambiguous bivalent toxins bound to the extracellular face of TRPV1. **A)** Map of TRPV1 (grey) with extra density corresponding to bivalent toxins (blue), shown as a side view (left) and a top view (right). **B)** Pore profile map determined by HOLE, comparing the pores of TRPV1 in the original unliganded structure (from PDB 3J5P, violet), the model refined from our double bivalent toxin reconstruction with RTX (blue), the model refined from our double bivalent toxin reconstruction without RTX (green), and the model refined from our reconstruction without RTX or observable ligand density (red). **C)** Modelling of the pore helices fit to our reconstructions of TRPV1 without toxin and RTX density (red, left), with bivalent toxin density but no RTX (green, middle), and with bivalent toxin density and RTX (blue, right).
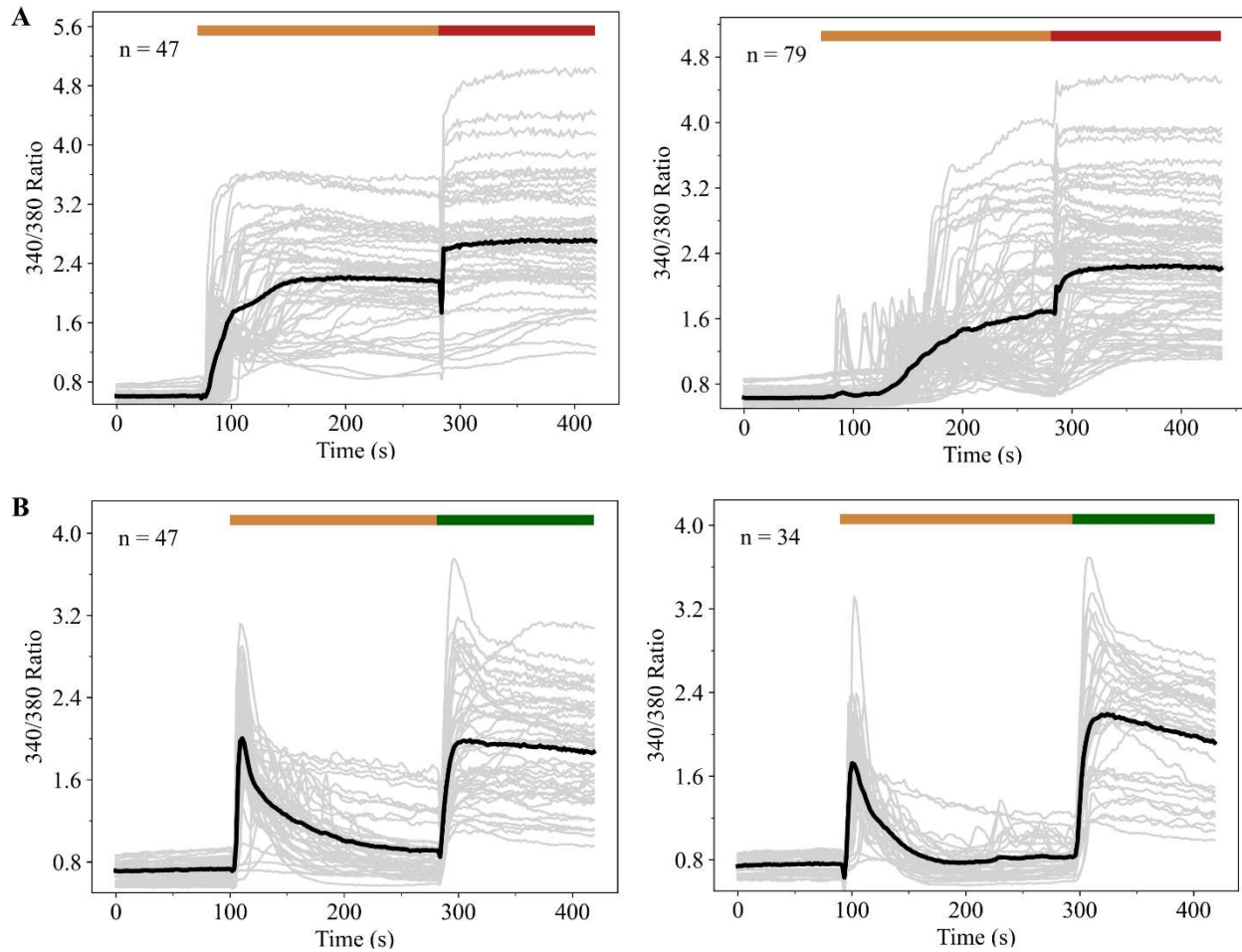
Figure S2.1 | Venom from *C. lividus* activates TRPV1 selectively, additional replicates
A) Analysis of calcium imaging data for TRPV1-transfected HEK-293 cells, for two additional replicates over what was show in **Figure 2.1C**. Regions of interest were selected, and the 340/380 ratios were measured as a function of time. Grey traces represent data for all regions of interest in view, the black trace represents the average of all grey traces. Orange bar reflects the period when 0.2 µg/µL venom was added, red bar reflects the period when venom and 10 µM capsaicin were co-applied. **B)** Analysis of calcium imaging data for TRPM8-transfected cells, for two additional replicates over what was show in **Figure 2.1D**. Similar to **A)** but using data for TRPM8 instead. Green bar indicates co-application of venom and 100 µM menthol.
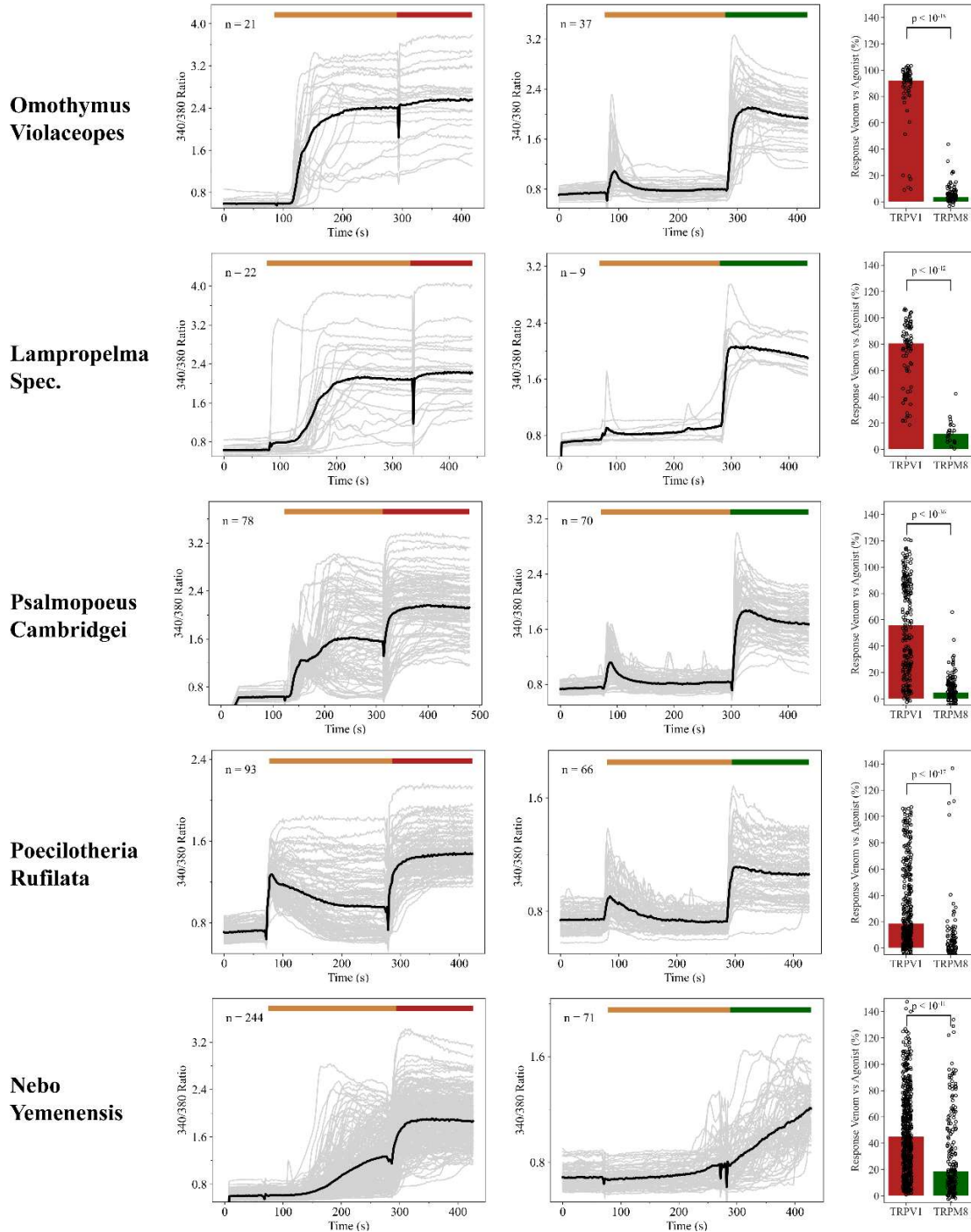
Figure S2.2 | Five other venoms from preliminary screen were found to activate TRPV1 selectively

Calcium imaging data analysis for other venoms where there was found to be an activating effect on TRPV1. Venom's source species is written on the far left of each row. Center-left panels show data for TRPV1-transfected cells, center-right panels show data for TRPM8-transfected cells. Regions of interest were selected, and the 340/380 ratios were measured as a function of time. Grey traces represent data for all regions of (Figure caption continued on the next page.)

(Figure caption continued from the previous page.) interest in view, the black trace represents the average of all grey traces. Orange bar reflects the period when 0.2 µg/µL venom was added, red bar reflects the period when venom and 10 µM capsaicin were co-applied, green bar indicates co-application of venom and 100 µM menthol. One replicate is shown per construct per venom. Far right panels show summary plot with spread of venom-evoked calcium responses normalized to the maximum response obtained by agonist. Data is the sum of all replicate imaging experiments. Each point is a region of interest. Bars show the median of each distribution. Statistical test used was Mann-Whitney U test, p-values are indicated on graphs.
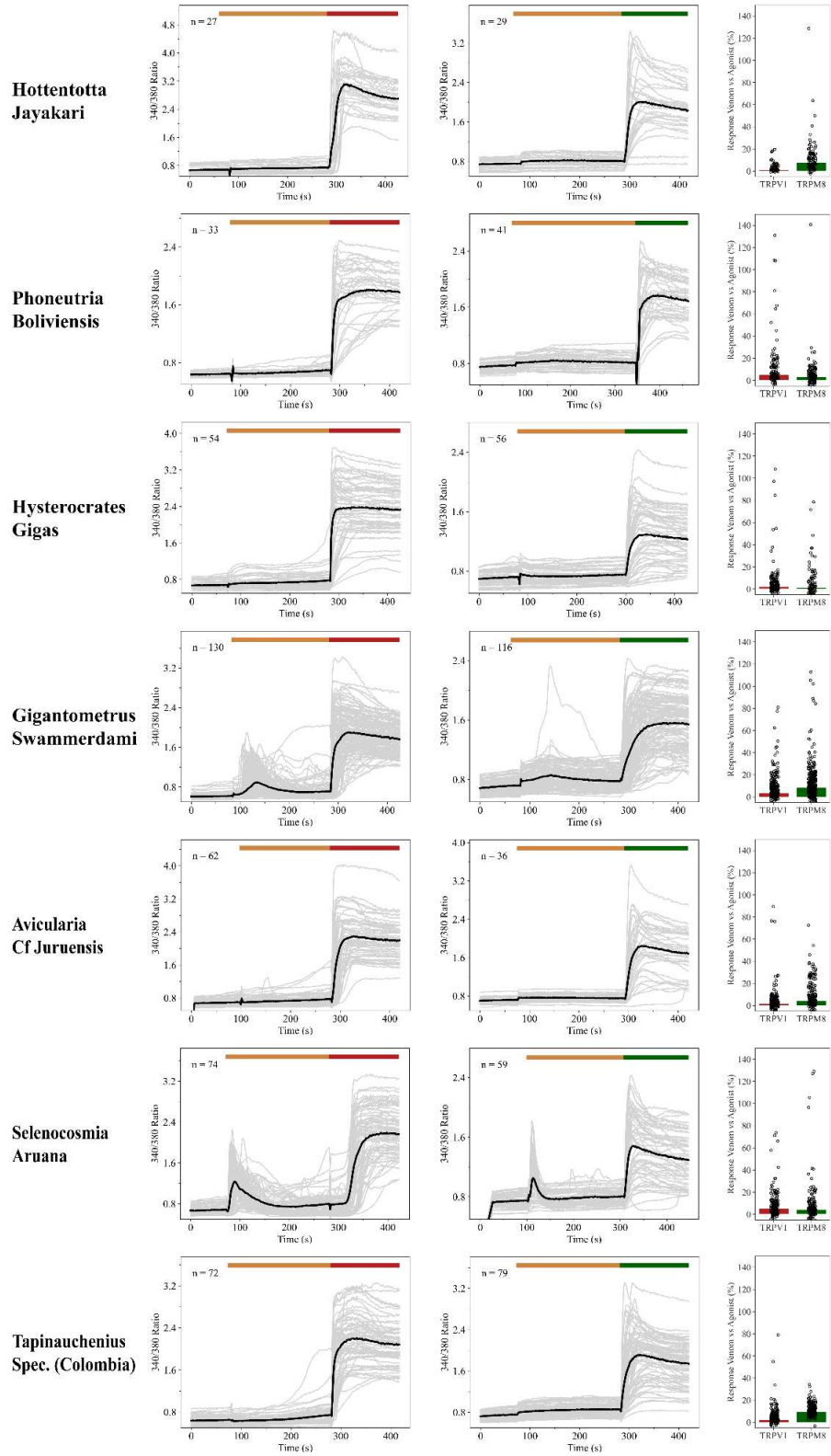
Figure S2.3 | Most other venoms from preliminary screen produce no activating response for either TRPV1 or TRPM8
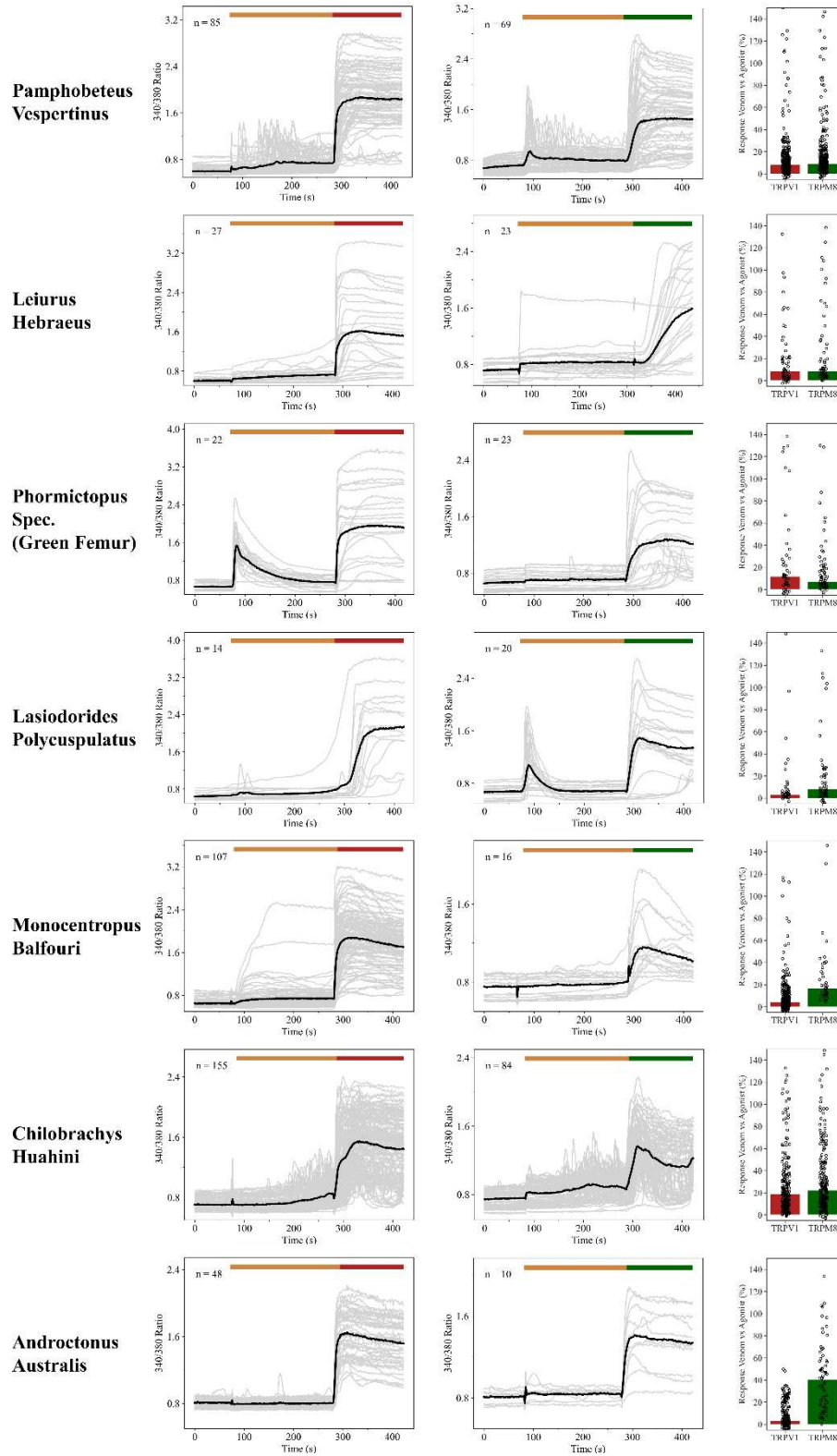(Figure continued on the next page.)

83

Figure S2.3 (continued) | Most other venoms from preliminary screen produce no activating response for either TRPV1 or TRPM8
(Figure continued from previous page, figure caption continued on the next page.)

(Figure caption continued from the previous page.) Calcium imaging data analysis for other venoms where there was not found to be an activating response either TRPV1 or TRPM8. Venom's source species is written on the far left of each row. Center-left panels show data for TRPV1-transfected cells, center-right panels show data for TRPM8-transfected cells. Regions of interest were selected, and the 340/380 ratios were measured as a function of time. Grey traces represent data for all regions of interest in view, the black trace represents the average of all grey traces. Orange bar reflects the period when 0.2 µg/µL venom was added, red bar reflects the period when venom and 10 µM capsaicin were co-applied, green bar indicates co-application of venom and 100 µM menthol. One replicate is shown per construct per venom. Far right panels show summary plot with spread of venom-evoked calcium responses normalized to the maximum response obtained by agonist. Data is the sum of all replicate imaging experiments. Each point is a region of interest. Bars show the median of each distribution.

Figure S2.4 | Venom from *C. lividus* activates minimal construct of TRPV1
Calcium imaging data analysis for cells transfected with the purification-amenable minimal construct of TRPV1, used for cryo-EM sample preparation. **A)** Shown are two independent replicates. Regions of interest were selected, and the 340/380 ratio were measured as a function of time. Grey traces represent data for all regions of interest in view, the black trace represents the average of all grey traces. Orange bar reflects the period when 0.2 µg/µL venom was added, red bar reflects the period when venom and 10 µM capsaicin were co-applied. **B)** Summary plot showing spread of venom-evoked calcium responses normalized to the maximum response obtained by agonist. Data is the sum of the two replicate imaging experiments shown in **A)**. Each point is a region of interest, totaling n = 218. Bar shows the median of the distribution.
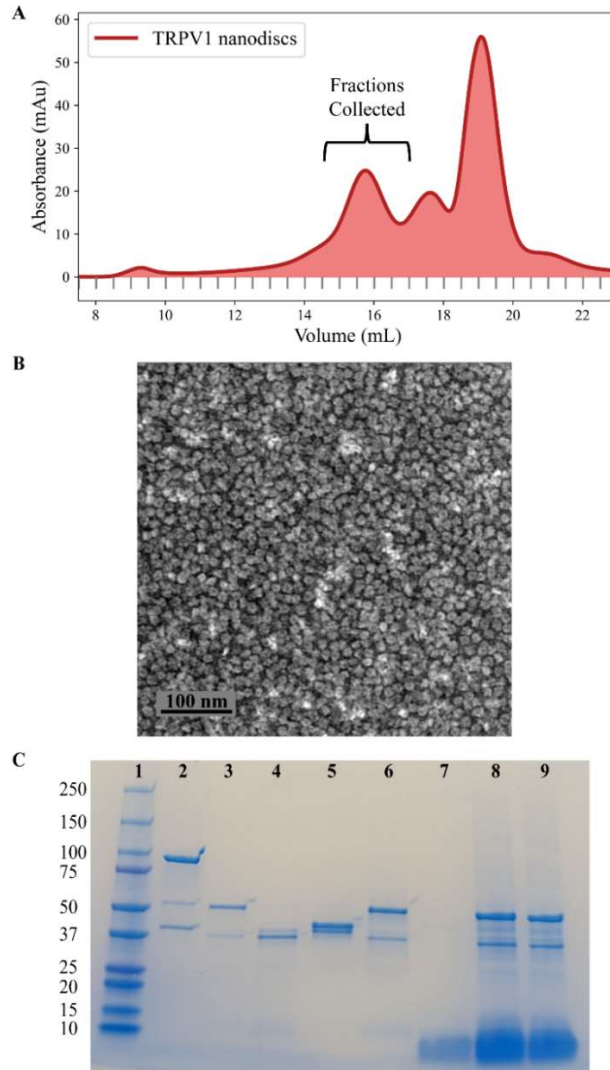
Figure S2.5 | Biochemical preparation and validation of TRPV1 nanodiscs to be combined with *C. lividus* crude venom

A) Size exclusion chromatography trace of TRPV1 nanodiscs, using a Superose 6 Increase 10/300 GL column. The protein peak occurred at 15.7 mL and fractions collected were between 14.5 and 17 mL, range shown by brace. **B)** Negative stain electron micrograph, confirming proper nanodisc assembly. **C)** Protein gel run from samples collected at different stages of TRPV1 nanodisc reconstitution prep. Sample in lane 1 came from the protein ladder, with sizes corresponding to each rung annotated to the left (in kDa). Sample in lane 2 came from the elution of maltose binding protein (MBP)-tagged TRPV1 in detergent, prior to Tobacco Etch Virus (TEV) removal of tag and nanodisc reconstitution. Sample in lane 3 came from sizing peak at 15.7 mL, corresponding to properly assembled nanodiscs of TRPV1 where the MBP tag was removed. Sample in lanes 4 and 5 came from sizing peaks at 17.6 mL and 19 mL, respectively, showing bands for excess MSP2N2 and/or leftover MBP. Sample in lane 6 came from TRPV1 nanodiscs concentrated from all collected fractions. Sample in lane 7 came from ~1.3 μg of *C. lividus* crude venom. Sample in lanes 8 and 9 came from mixture of TRPV1 nanodiscs and *C. lividus* venom, left over after grid preparation. Sample in lane 9 also had RTX.

87
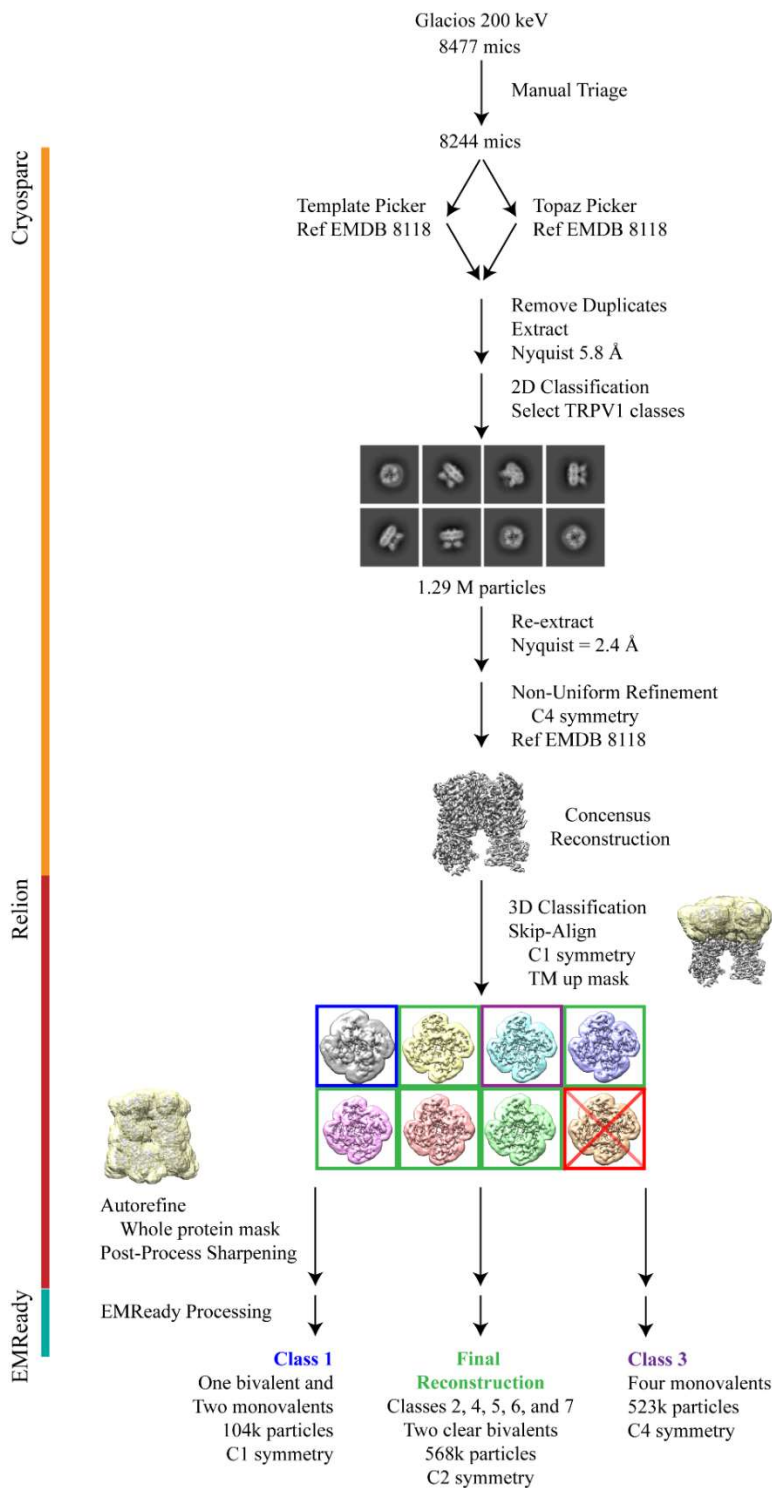
Figure S2.6 | Data processing scheme for TRPV1 combined with *C. lividus* venom, with RTX condition
Schematic shows data processing workflow, starting with picking and 2D classification in CryoSPARC, followed by 3D classification and 3D refinement in Relion, and then finally post-processing in EMReady.

88

Figure S2.7 | Resolution and angular distribution plots for final reconstruction of TRPV1 bound to two bivalent toxins from *C. lividus*, with RTX
A) Directional Fourier shell correlation (dFSC) curves (in purple) overlaid with the average FSC (Fourier shell correlation) curve (in green). Dashed line reflects 0.143 criterion used to estimate resolution, which in this case is 3.12 Å. **B)** Distribution of particle angular alignments used in final reconstruction, red reflects more views, blue reflects less. **C)** Local resolution estimates of the TRPV1 and toxin complex, shown as a side view (left) and a top view (right). **D)** Local resolution estimates of just a single bivalent toxin. Two side views are shown, one away from the pore (left) and one towards the pore (right). Both **C)** and **D)** follow the color key shown to their far right, blue and red reflecting higher and lower resolutions, respectively. Scale is in Å.
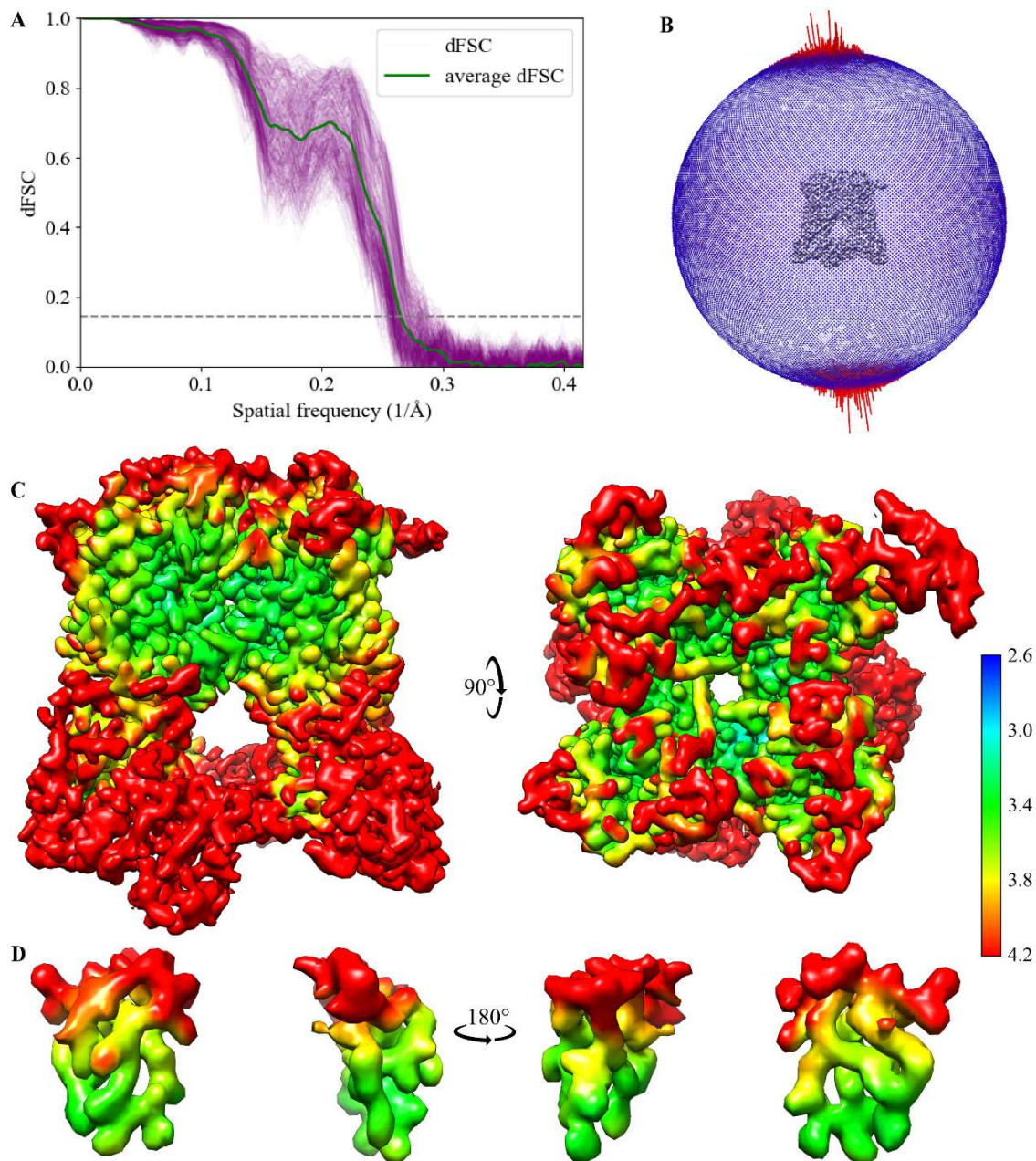
Figure S2.8 | Resolution and angular distribution plots for alternative reconstruction of TRPV1 bound to one bivalent and two monovalent toxins from *C. lividus*, with RTX
A) dFSC curves (in purple) overlaid with the average FSC curve (in green). Dashed line reflects 0.143 criterion used to estimate resolution, which in this case is 3.79 Å. **B)** Distribution of particle angular alignments used in final reconstruction, red reflects more views, blue reflects less. **C)** Local resolution estimates of the TRPV1 and toxins complex, shown as a side view (left) and a top view (right). **D)** Local resolution estimates of just the two monovalent toxin densities, ignoring the bivalent toxin. Two side views are shown, one away from the pore (left) and one towards the pore (right). Both **C)** and **D)** follow the color key shown to their far right, blue and red reflecting higher and lower resolutions, respectively. Scale is in Å.
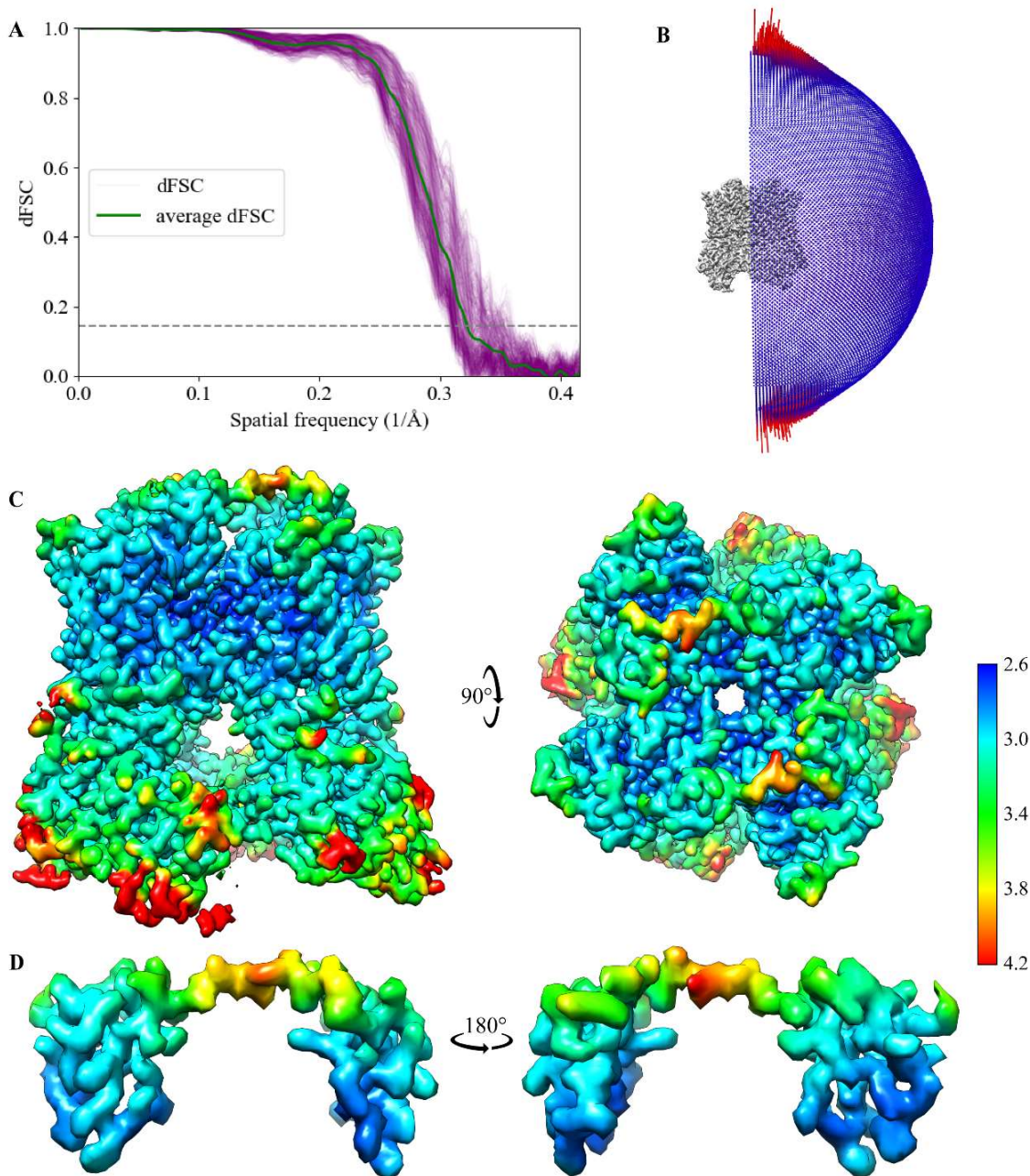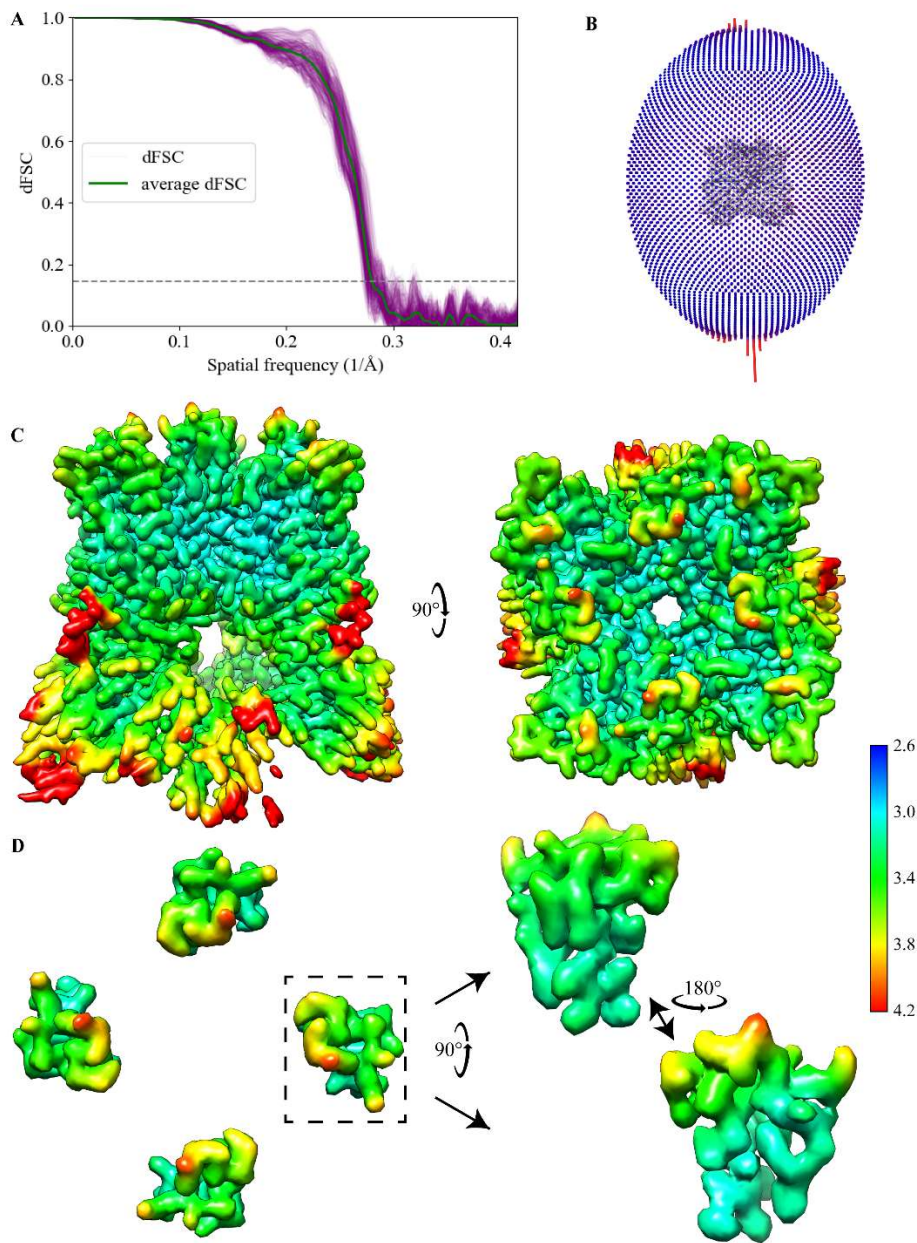
Figure S2.9 | Resolution and angular distribution plots for alternative reconstruction of TRPV1 bound to four monovalent toxins from *C. lividus*, with RTX

A) dFSC curves (in purple) overlaid with the average FSC curve (in green). Dashed line reflects 0.143 criterion used to estimate resolution, which in this case is 3.59 Å. **B)** Distribution of particle angular alignments used in final reconstruction, red reflects more views, blue reflects less. **C)** Local resolution estimates of the TRPV1 and toxins complex, shown as a side view (left) and a top view (right). **D)** Local resolution estimates of just the monovalent toxin densities, left showing a top view of all four toxins, right showing side views towards and away from the pore for a single toxin. All toxins were equivalent due to imposed four-fold symmetry. Both **C)** and **D)** follow the color key shown to their far right, blue and red reflecting higher and lower resolutions, respectively. Scale is in Å.

A

Accession Number	P0CH72
Number of Unique Peptides	1
Peptide Count	1
Percent Coverage	21.9
Best Discriminant Score	5.57
Best Expectation Value	5.4e-14
Protein Length	32
Molecular Weight	3673.4
Species	CYRHA Cyriopagopus hainanus (Chinese Bird Spider)
Protein Name	U3-theraphotoxin-Hhn1r U3-TRTX-Hhn1r

B

C

D

DkTx Sequence
```
DCAKEGEVCSWGKKCCDLDNFYPPMEFIPHCKKYKPYVPVTTNCAKEGEVCGWGSKCCHGLDCPLAFIPYCEKYR
...................................|.......|..|...............|..........|.....
```
Predicted Sequence
```
XXXPWAHHNNPWPHWRNHNDNRYNNRWNTYCNRWNEHNPNNDNRSRHAHNRKPAHRCNYHNNTNNSYNNYKREGN
```

Figure S2.10 | Attempted sequence prediction from structure for bivalent toxin from *C. lividus*

A) Mass spectrometry done on *C. lividus* crude venom identified the toxin U3-TRTX-Hhn1r as a potential candidate for the monovalent toxin observed. Parameters from ProteinProspector are tabulated. **B)** Structure of U3-TRTX-Hhn1r, predicted by AlphaFold, adopting a single ICK fold. **C)** AlphaFold model of the DeepTracer prediction generated from the bivalent toxin density, which does not form an ICK motif. **D)** Sequence alignment of the DeepTracer prediction generated from the bivalent toxin density against the actual sequence of DkTx. Green boxes represent identity. Only 5 residues are predicted to be identical to DkTx.
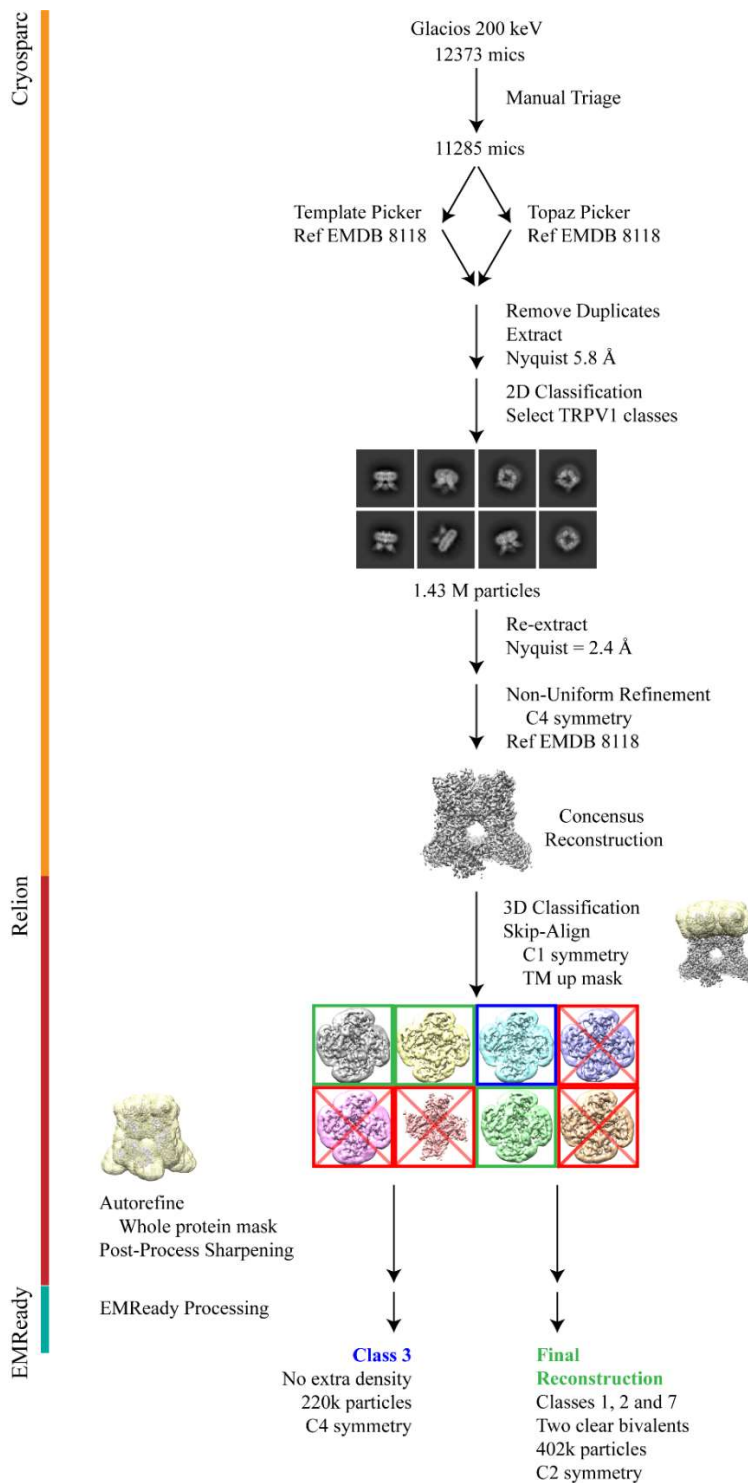
Figure S2.11 | Data processing scheme for TRPV1 combined with *C. lividus* venom, no RTX condition
Schematic shows data processing workflow, starting with picking and 2D classification in CryoSPARC, followed by 3D classification and 3D refinement in Relion, and then finally post-processing in EMReady.
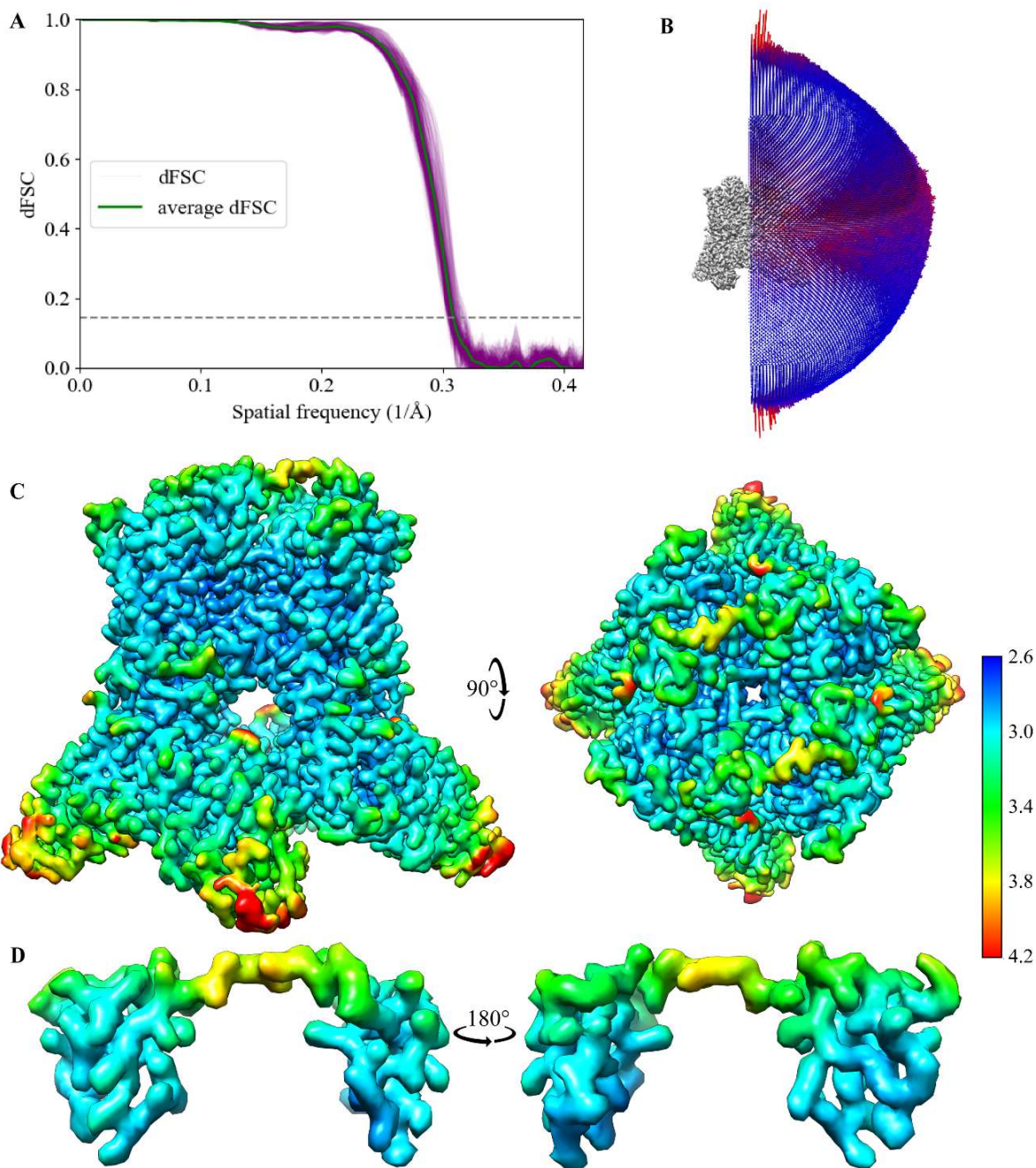
Figure S2.12 | Resolution and angular distribution plots for final reconstruction of TRPV1 bound to two bivalent toxins from *C. lividus*, without RTX
A) dFSC curves (in purple) overlaid with the average FSC curve (in green). Dashed line reflects 0.143 criterion used to estimate resolution, which in this case is 3.25 Å. **B)** Distribution of particle angular alignments used in final reconstruction, red reflects more views, blue reflects less. **C)** Local resolution estimates of the TRPV1 and toxin complex, shown as a side view (left) and a top view (right). **D)** Local resolution estimates of just a single bivalent toxin. Two side views are shown, one away from the pore (left) and one towards the pore (right). Both **C)** and **D)** follow the color key shown to their far right, blue and red reflecting higher and lower resolutions, respectively. Scale is in Å.
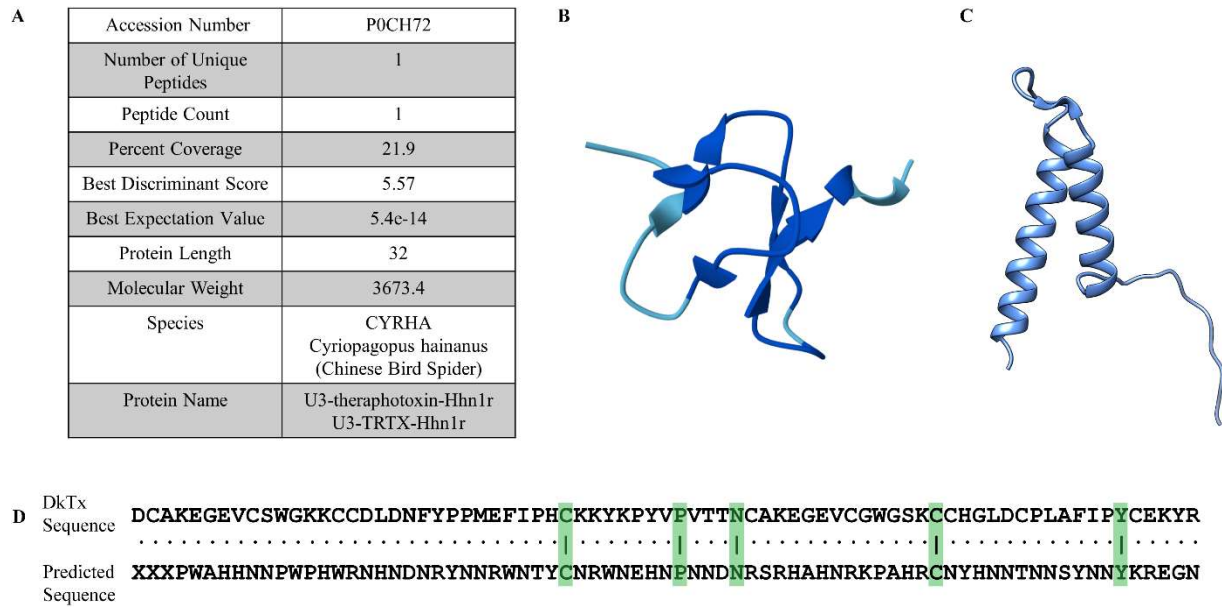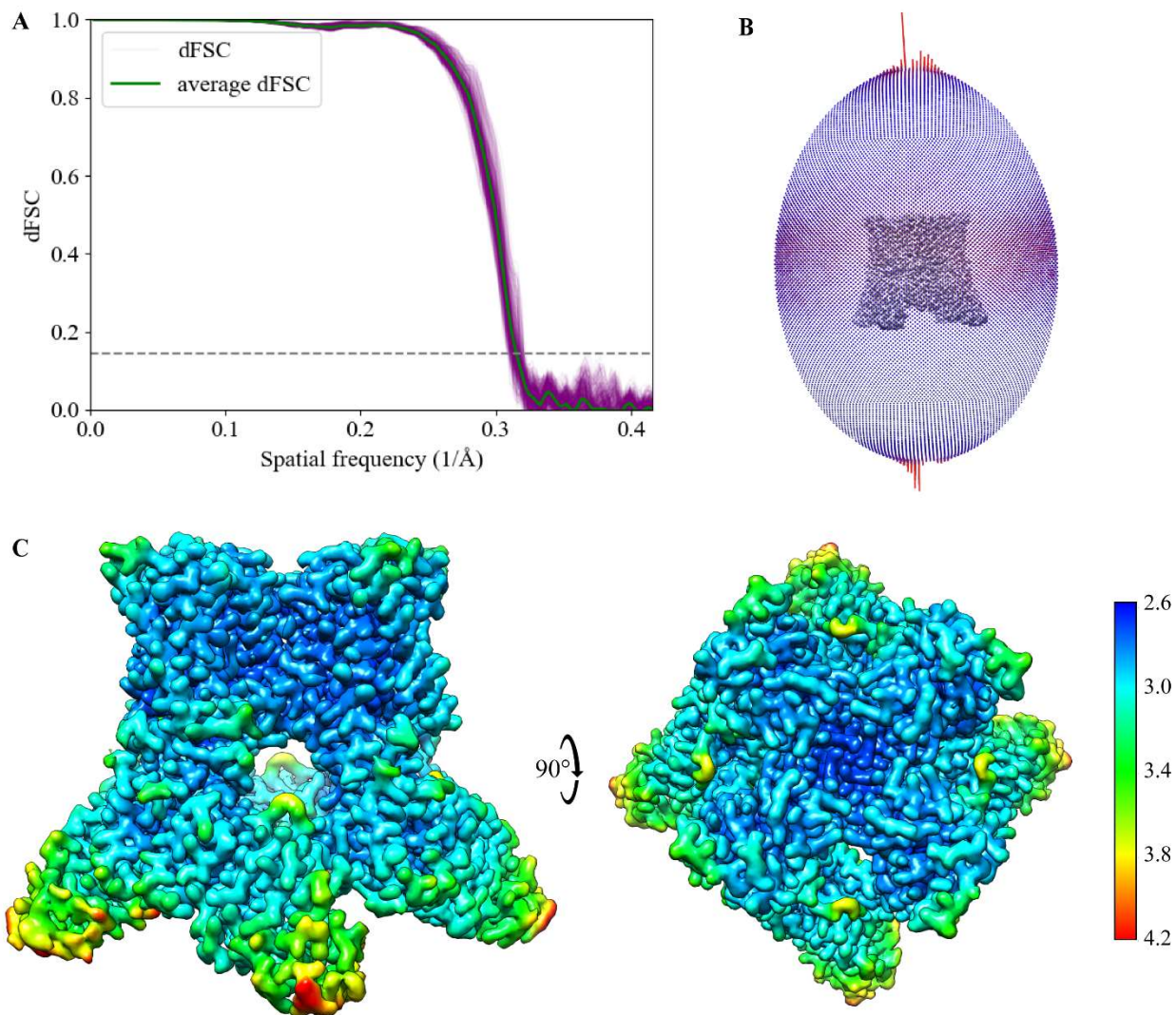
Figure S2.13 | Resolution and angular distribution plots for alternative reconstruction lacking additional toxin density, without RTX
A) dFSC curves (in purple) overlaid with the average FSC curve (in green). Dashed line reflects 0.143 criterion used to estimate resolution, which in this case is 3.19 Å. **B)** Distribution of particle angular alignments used in final reconstruction, red reflects more views, blue reflects less. **C)** Local resolution estimates of the TRPV1 map, shown as a side view (left) and a top view (right). Map is colored according to color key shown on the far right, blue and red reflecting higher and lower resolutions, respectively. Scale is in Å.

Table S2.1 | Data acquisition parameters for TRPV1 samples combined with P183 and RTX and combined with P183 without RTX
Microscope data acquisition parameters for the two datasets.

Sample Grid ID	TRPV1 + C. Lividus Venom + RTX Neo23 grid 1	TRPV1 + C. Lividus Venom No RTX Neo21 grid 4
Microscope ID	UCSF Glacios	UCSF Glacios
Magnification	54,000	54,000
Voltage (keV)	200	200
Dose rate (e⁻/pix/s)	16	16
Dose (e⁻/pix/frame)	0.60	0.60
Total dose (e⁻/Å)	60	60
Defocus range (µm)	-1.2 to -2.4	-1.2 to -2.4
Pixel size (Å)	0.73	0.73

Methods

Materials

All reagents were procured from Sigma-Aldrich unless mentioned otherwise.

Venom Extraction

Crude venoms were harvested from specimens in one of two ways. For spiders, 12V electrical stimulations were applied to the basal parts of the chelicerae, and venom was extracted from the tips of the fangs (for details see reference[98]). For scorpions, the organisms were aggravated to the point they would sting a parafilm membrane, from which venom was subsequently collected using a pipette. All venoms were dried down by lyophilization or vacuum centrifugation. These were then maintained in Dr. Herzig Volker's *Arthropod Venom Biobank*.

Calcium Imaging Screening

Full-length human TRPV1 and full-length human TRPM8 constructs were transiently transfected into adherent HEK-293T cells (ATCC) overnight, using Lipofectamine 3000 transfection reagent (Invitrogen). The next day, cells were dissociated with StemPro Accutase cell dissociation reagent (Gibco) and plated in the wells of a Press-to-Seal Silicone Isolator (Invitrogen, O.D. x Depth, 2.5 × 2.0 mm) mounted on a Superfrost Plus microscope slide (Fisher Scientific) treated with 0.1 mg/mL poly-D-lysine. After a minimum four-hour settling period, cells were loaded with a 10 µg/mL cell-permeant Fura-2AM (Invitrogen) dissolved in Ringer's solution (140 mM NaCl, 5 mM KCl, 10 mM HEPES pH = 7.6, 2 mM $MgCl_2$, 2 mM $CaCl_2$, 10 mM D-glucose, final solution pH-adjusted to 7.4) with 0.2% (v/v) Pluronic F-127 (Invitrogen) for 30 minutes in the dark, and subsequently rinsed three times with and left in Ringer's solution.

97

Cells were then taken to an IX71 inverted microscope setup (Olympus) equipped with a Lambda LS Illuminator (Sutter) and Lambda 10-2 optical filter changer (Sutter). Fluorescent emissions data was collected at 340 and 380 nm at a frequency of about 1 Hz, and imaging data were digitized with MetaFluor software (Molecular Devices).

Initially dried-down venoms were rehydrated in UltraPure Distilled Water (Invitrogen), combined with 2X stock solution to reach Ringer's solution final concentrations, and then spin-filtered through a 50 kDa MWCO ultra centrifugal filter (Amicon) for 10 minutes at 10,000xg to remove larger enzymes. During a typical recording session, imaging was first done in the absence of any ligand to establish a baseline, then in the presence of venom at a final concentration of roughly 0.2 µg/µL, and finally in the presence of a known channel agonist (final concentration of 10 µM capsaicin for TRPV1 or 100 µM menthol for TRPM8) to obtain a maximum calcium response. Each venom was tested against TRPV1 and TRPM8 in immediate succession, different venoms were tested across different days.

The experimenter handled each venom blinded to its species identity until after analysis was done, to avoid bias. For any positive-hit venoms, the above calcium imaging experiment was repeated using the rat TRPV1 minimal construct that was amenable to protein purification.

Calcium Imaging Analysis

The output from each calcium imaging recording, i.e. the individual 340 and 380 nm wavelength stacks, were imported into a custom Python script that then generated a single stack containing 340/380 ratios. This was taken to Fiji software, where regions of interest were manually picked from the last frame of the recording and the average signal for each region of interest was subsequently measured across all frames. The final output, 340/380 ratio as a

function of time across a population of cells, was then analyzed using a custom Python script. The baseline 340/380 ratio was constrained to a range of 0.5 to 0.9 to isolate cells that were not activated at baseline.

Calcium imaging data were plotted in two ways. One was the 340/380 ratio over time, for which we included both the individual traces and the averaged trace. The other was the venom response normalized to the agonist response (i.e. capsaicin response for TRPV1 and menthol response for TRPM8), for which individual values were plotted as a scatter plot and the distribution median was plotted as a bar graph. We chose the median due to the high variability in the data collected. Graphs showed only responses between -5 and 150% for clarity, but all values were included when calculating the median.

Where used, statistical testing was carried out in Python. The applicability of parametric tests was first assessed, examining whether the data followed assumptions about equal variance (Levene's test) and normal distribution (Shapiro–Wilk test). Where either of these assumptions were violated, we used nonparametric tests, particularly a Mann-Whitney U test. For all tests, a priori, we set $\alpha = 0.05$ and represent statistical significance with the P value, as indicated in the figure legends. We selected sample sizes for all experiments based on our laboratory and others' experience with similar assays.

TRPV1 Purification

Recombinant minimal functional rat TRPV1 (residues 110-603 and 627-764, lacking 110 residues in the N-terminus, 23 residues in the pore helices, and 74 residues in the C-terminus) with a maltose-binding protein (MBP) tag was purified similar to previous studies[21] with some modification. Expi-293F cells (Gibco) were transfected using the ExpiFectamine 293

Transfection Kit (Gibco). Cells were left to express protein for 48 hours, after which they were pelleted, flash-frozen in liquid nitrogen, and stored at -80°C until use.

The cell pellet was resuspended in buffer containing 150 mM NaCl, 20 mM HEPES pH = 7.6, 0.4 mM TCEP, and dissolved protease inhibitor tablets (cat #A32965, Pierce). TRPV1 was then extracted over 2.5 hours following the addition of 14.7 mM (0.75%) n-dodecyl-β-D-maltopyranoside (DDM, Anatrace). Insoluble cell debris was removed by ultracentrifugation at 46,000xg for 1 hour at 4°C, while the supernatant was vacuum-filtered at 0.2 μm (Steritop, Millipore) and combined with amylose resin (New England Biolabs) for 2 hours to bind MBP-tagged protein. The sample was then poured over a Poly-Prep chromatography column (Bio-Rad) and washed with at least 8 column volumes of buffer containing 150 mM NaCl, 20 mM HEPES pH = 7.6, 0.5 mM (0.0256%) DDM, and 0.4 mM TCEP to remove impurities. TRPV1 was then eluted with buffer containing 150 mM NaCl, 20 mM HEPES pH = 7.6, 0.5 mM (0.0256%) DDM, and 20 mM maltose (TCEP was removed so as not to interfere with disulfides bonds in ICK toxins).

TRPV1 nanodiscs were generated according to established protocols[28]. One day earlier, soy extract polar lipids (Avanti) dissolved in chloroform were dried down and left in a vacuum desiccator overnight. The day of a protein prep, soybean lipids were resuspended in buffer containing 150 mM NaCl, 20 mM HEPES pH = 7.6, and 30 mM (1.54%) DDM. Lipids were first left to sit in buffer for 30 minutes, then vortexed for 30 seconds, and finally bath sonicated for 10 minutes to ensure dispersion.

Eluted TRPV1 was then transferred to nanodiscs. MBP-tagged TRPV1, dissolved soybean lipids, and MSP2N2 (purified in-house, see next methods section) were all combined in a mass ratio of 1:0.667:0.7 in a final volume of ~750 μL. The mixture was left to incubate for 30

minutes at 4°C on a rotator. Then, 70 mg of Bio-Beads SM-2 Resin (Bio-Rad) was added and left for one hour to start the detergent removal process. Finally, another 70 mg of Bio-Beads, along with 50 µg of Tobacco Etch virus (TEV) protease (purified in-house, similar to MSP2N2 protocol) to remove the MBP tag, were added to the mixture and left overnight. The resulting nanodisc mixture was filtered at 0.2 µm and further cleaned up by size exclusion chromatography (AKTA) over a Superose 6 Increase 10/300 GL column (Cytiva) using sizing buffer containing 150 mM NaCl and 20 mM HEPES pH = 7.6. Peak fractions were then concentrated in a 100 kDa MWCO ultra centrifugal filter (Amicon) at 10,000xg to a final concentration over 1.5 mg/mL, amenable to Cryo-EM.

TRPV1 nanodisc assembly was further validated by negative stain electron microscopy. Formvar/carbon 400 mesh copper grids (Ted Pella) were glow-discharged by a Pelco easiGlow (Ted Pella), with settings of 15 mA current, 30 seconds hold time, 30 seconds glow time. TRPV1 sample was diluted to 0.1 mg/mL, applied to grids, and then coated with 0.75% uranyl formate stain. Excess solution was wicked away by Whatman filter paper. Sample was taken to a Tecnai T12 microscope (FEI), operating at 120 kV, with a LaB6 filament, and equipped with an UltraScan 895 4k CCD camera (Gatan), available at the Electron Microscopy core facility at the University of California, San Francisco (UCSF). Magnification was set to 52,000x and exposure time to 2 seconds. Motion-correction was done on-the-fly using scripts built into DigitalMicrograph (Gatan).

MSP2N2 Purification

The membrane scaffold protein, MSP2N2, for nanodisc reconstitution was expressed in *Escherichia Coli* as previously described[28,99]. His-tagged MSP2N2 was transformed into BL21

competent E. Coli (New England Biolabs) and grown in 6 L cultures at 37°C and 220 rpm. After reaching an O.D. of 0.8 to 1.0, cultures were induced with 1 mM IPTG. Cells were harvested 3 hours later at 3,500xg and 4°C for 15 minutes. Pellets were flash-frozen in liquid nitrogen and stored at -80°C until use.

On the day of a prep, pellets were thawed and resuspended in PBS containing Sigmafast protease inhibitor cocktail and 5 µg/mL DNase1. Bacterial cell walls were broken by an Emulsiflex C3 (Avestin) at 4°C and pelleted by centrifugation at 46,000xg and 4°C for 1 hour. The supernatant was filtered at 0.2 µm and then combined with Ni-NTA agarose resin (Qiagen), to bind His-tagged proteins, for 2 hours. The sample was then poured over a Poly-Prep chromatography column (Bio-Rad) and washed with 1) buffer containing 300 mM NaCl, 40 mM Tris-HCl pH = 8, and 1% triton, then 2) buffer containing 300 mM NaCl, 40 mM Tris-HCl pH = 8, 50 mM Na-Cholate, and 20 mM imidazole, then 3) buffer containing 300 mM NaCl, 40 mM Tris-HCl pH = 8, 50 mM imidazole. Protein was then eluted with buffer containing 150 mM NaCl, 40 mM Tris-HCl, and 300 mM imidazole. MSP2N2 was dialyzed overnight (to remove imidazole) in excess buffer containing 150 mM NaCl, 20 mM Tris-HCl pH = 8, and 0.5 mM Na-EGTA, then concentrated in a 3.5K MWCO ultra centrifugal filter (Amicon) at 10,000xg to reach a stock concentration of ~5 mg/mL. MSP2N2 was aliquoted, flash frozen in liquid nitrogen, then stored at -80°C until use.

Note that TEV protease was also purified following a very similar protocol.

Cryo-EM Grid Sample Preparation

Dried venoms were first resuspended in buffer containing 150 mM NaCl and 20 mM HEPES pH = 7.6 to a final concentration of ~3 µg/µL. Protease inhibitors (cat #A32965, Pierce)

were then added to our venom at a final concentration of 2X the recommended dose. Venom, with protease inhibitors, and TRPV1 were then mixed in equal volume to achieve final concentrations of ~1.5 µg/µL, 1X the recommended dose, and ~1 mg/mL, respectively. In some cases, the agonist resiniferatoxin (RTX, AdipoGen) was also added to a final concentration of 50 µM. Our sample was left to incubate on ice for 20 minutes prior to vitrification.

Quantifoil R1.2/1.3 gold 300 mesh or 400 mesh grids covered in holey carbon film (Quantifoil Micro Tools GmbH) were glow-discharged by a Pelco easiGlow (Ted Pella), with settings of 15 mA current, 30 seconds hold time, 30 seconds glow time. Grids were frozen using a Vitrobot Mark IV (FEI Company). 2.0-2.5 µL of TRPV1-venom mixture was applied to grids with excess blotted away with Whatman filter paper. Blotting parameters included a 5 second wait time, 6-8 second blotting time, 0-1 blot force, 4°C and 100% humidity. Sample was then plunge-frozen in liquid ethane cooled by liquid nitrogen.

Cryo-EM Data Acquisition

Samples were screened and collections were run on a Glacios Cryo-Transmission Electron Microscope (ThermoFisher FEI) operated at 200 keV and equipped with a K3 camera (Gatan). Follow up data was obtained on the Titan Krios microscope (ThermoFisher FEI) operated at 300 kV and equipped with a post-column Bio Quantum energy filter with zero-loss energy selection slit set to 20 eV and a K3 camera (Gatan) – but data was not shown in this dissertation. Both microscopes were part of the Electron Microscopy core facility at the University of California, San Francisco (UCSF). Data collection was carried out with SerialEM[67] software. Collection parameters are reported in Table S2.1.

Cryo-EM Image Processing

Motion correction on movie stacks was processed on-the-fly using MotionCorr2[68] in Scipion, final pixel sizes were 0.73 Å per pixel (Glacios) or 0.8189 Å per pixel (Titan Krios). Dose-weighted micrographs were visually inspected to remove bad micrographs. The first stages of processing, from CTF estimation to the initial refinements, were done in CryoSPARC[69] installed on local workstations. Patch CTF estimation was done to estimate CTF parameters. Particles were picked in two independent streams, using template-based particle picking and Topaz-based picking[100] using a subset of vetted template-based picks. The volume used as the template was EMD-8118, unliganded TRPV1 in a nanodisc[28]. Particles were then extracted and down-sampled 4 times by Fourier cropping and taken to reference-free 2D classification to remove non-TRPV1 picks. After ensuring duplicates were removed (discarding picks within 45 Å), final particles were extracted to a box size of ~1.20 Å per pixel and then taken to non-uniform refinement with C4 symmetry applied. From there, particle alignments were transferred to Relion[70] on UCSF's Wynton high-performance compute cluster. Particles underwent skip-align 3D classification, where the reference and initial alignments came from CryoSPARC's non-uniform refinement, using 8 classes, a T parameter of 30, 75 iterations, and no (i.e. C1) applied symmetry. Classes were subsequently taken to auto-refine with global searches and local searches enabled. Final reconstructions were then subject to post-processing in Relion, with automatic B-factor sharpening, followed by additional processing in EMReady[101]. Resolutions were determined according to the gold-standard Fourier shell correlation (FSC) of 0.143 criterion[71] and with a mask applied around the proteinaceous density. Volumes were manually inspected in UCSF Chimera[74].

Model Building

Existing published models were used as starting points for modelling, including 7L2R, TRPV1 bound to DkTx in the pre-open state[29], and 3J5P, for unliganded TRPV1[21]. Molecular restraint files for the RTX ligand were generated in Phenix[73] using eLBOW. Models and ligands were then refined in our cryo-EM reconstructions using several back-and-forth iterations of Phenix Real Space Refine and follow-up manual adjustments in Coot[75]. Pore profile analysis was done using the HOLE[77] plug-in in Coot.

Toxin Structure Prediction

Bivalent toxin density was isolated from the final cryo-EM reconstruction using color zone and segger functions in Chimera[74]. This density map was then given as input to DeepTracer[94], without any sequence provided. Prediction was repeated until the result was a single polypeptide chain, as it was common to obtain a series of 3-4 separate fragments. The sequence alignment between predicted sequence and DkTx sequence was done via custom Python scripts. Validation of sequence prediction by structure prediction was carried out using AlphaFold[95,96].

Mass Spectroscopy

An estimated 3 µg of crude venom was run on a 4-15% Mini-PROTEAN protein gel (Bio-Rad) and stained with InstantBlue Coomassie Protein Stain (Abcam). A band was observed below the 10 kDa mark. It was cut, cleaned with multiple treatments of ammonium bicarbonate and acetonitrile, then digested in-gel with trypsin. Peptides were then extracted from the gel, eluted off a C18 ZIP-tip (Millipore), dried down, and stored at -80°C until use.

Samples were submitted to UCSF's Mass Spectrometry core facility, implementing LC-MS analysis. Peptides were analyzed on a QExactive Plus (Thermo Scientific), connected to a NanoAcquityUltraPerformance UPLC system (Waters). A 15-cm EasySpray C18 column (Thermo Scientific) was used to resolve peptides (60-min 2–30% gradient with 0.1% formic acid in water as mobile phase A and 0.1% formic acid in acetonitrile as mobile phase B). Mass spectrometer was operated in positive ion mode and in data-dependent mode to automatically switch between MS and MS/MS. MS spectra were acquired between 350 and 1500 m/z with a resolution of 70,000.

After spectrometric data acquisition, peaklists generated using PAVA in-house software were searched against all species in the SwissProt.2022.05.26 random.concat database (containing 567,483 entries) using ProteinProspector[102] with the following parameters: 1) enzyme specificity was set as trypsin, 2) one missed cleavage per peptide was allowed, 3) N-acetylation of the N-terminus of the protein, loss of protein N-terminal methionine, pyroglutamate formation from peptide N-terminal glutamines, and oxidation of methionine were allowed as variable modifications, 4) mass tolerance was set to 10 ppm in MS and 30 ppm in MS/MS. The false positive rate was estimated by searching the data using a concatenated database which contains the original SwissProt database, as well as a version of each original entry where the sequence has been randomized. A 1% false discovery rate was permitted at the protein and peptide levels.

REFERENCES

1. Purves, D. ed. (2008). Neuroscience 4th ed. (Sinauer).

2. Kandel, E.R. ed. (2013). Principles of neural science 5th ed. (McGraw-Hill).

3. Yu, F.H., Yarov-Yarovoy, V., Gutman, G.A., and Catterall, W.A. (2005). Overview of Molecular Relationships in the Voltage-Gated Ion Channel Superfamily. Pharmacol. Rev. *57*, 387–395. https://doi.org/10.1124/pr.57.4.13.

4. Hille, B. (2001). Ion channels of excitable membranes 3rd ed. (Sinauer).

5. Diver, M.M., Lin King, J.V., Julius, D., and Cheng, Y. (2022). Sensory TRP Channels in Three Dimensions. Annu. Rev. Biochem. *91*, 629–649. https://doi.org/10.1146/annurev-biochem-032620-105738.

6. Caterina, M.J., Schumacher, M.A., Tominaga, M., Rosen, T.A., Levine, J.D., and Julius, D. (1997). The capsaicin receptor: a heat-activated ion channel in the pain pathway. Nature *389*, 816–824. https://doi.org/10.1038/39807.

7. Tominaga, M., Caterina, M.J., Malmberg, A.B., Rosen, T.A., Gilbert, H., Skinner, K., Raumann, B.E., Basbaum, A.I., and Julius, D. (1998). The Cloned Capsaicin Receptor Integrates Multiple Pain-Producing Stimuli. Neuron *21*, 531–543. https://doi.org/10.1016/S0896-6273(00)80564-4.

8. Kobayashi, K., Fukuoka, T., Obata, K., Yamanaka, H., Dai, Y., Tokunaga, A., and Noguchi, K. (2005). Distinct expression of TRPM8, TRPA1, and TRPV1 mRNAs in rat primary afferent neurons with aδ/c-fibers and colocalization with trk receptors. J. Comp. Neurol. *493*, 596–606. https://doi.org/10.1002/cne.20794.

9. Julius, D. (2013). TRP Channels and Pain. Annu. Rev. Cell Dev. Biol. *29*, 355–384. https://doi.org/10.1146/annurev-cellbio-101011-155833.

10. Caterina, M.J., Leffler, A., Malmberg, A.B., Martin, W.J., Trafton, J., Petersen-Zeitz, K.R., Koltzenburg, M., Basbaum, A.I., and Julius, D. (2000). Impaired Nociception and Pain Sensation in Mice Lacking the Capsaicin Receptor. Science *288*, 306–313. https://doi.org/10.1126/science.288.5464.306.

11. Davis, J.B., Gray, J., Gunthorpe, M.J., Hatcher, J.P., Davey, P.T., Overend, P., Harries, M.H., Latcham, J., Clapham, C., Atkinson, K., et al. (2000). Vanilloid receptor-1 is essential for inflammatory thermal hyperalgesia. Nature *405*, 183–187. https://doi.org/10.1038/35012076.

12. Zygmunt, P.M., Petersson, J., Andersson, D.A., Chuang, H., Sørgård, M., Di Marzo, V., Julius, D., and Högestätt, E.D. (1999). Vanilloid receptors on sensory nerves mediate the vasodilator action of anandamide. Nature *400*, 452–457. https://doi.org/10.1038/22761.

13. Huang, S.M., Bisogno, T., Trevisani, M., Al-Hayani, A., De Petrocellis, L., Fezza, F., Tognetto, M., Petros, T.J., Krey, J.F., Chu, C.J., et al. (2002). An endogenous capsaicin-like substance with high potency at recombinant and native vanilloid VR1 receptors. Proc. Natl. Acad. Sci. *99*, 8400–8405. https://doi.org/10.1073/pnas.122196999.

14. Hwang, S.W., Cho, H., Kwak, J., Lee, S.-Y., Kang, C.-J., Jung, J., Cho, S., Min, K.H., Suh, Y.-G., Kim, D., et al. (2000). Direct activation of capsaicin receptors by products of lipoxygenases: Endogenous capsaicin-like substances. Proc. Natl. Acad. Sci. *97*, 6155–6160. https://doi.org/10.1073/pnas.97.11.6155.

15. Chuang, H., Prescott, E.D., Kong, H., Shields, S., Jordt, S.-E., Basbaum, A.I., Chao, M.V., and Julius, D. (2001). Bradykinin and nerve growth factor release the capsaicin receptor from PtdIns(4,5)P2-mediated inhibition. Nature *411*, 957–962. https://doi.org/10.1038/35082088.

16. Rohacs, T. (2014). Phosphoinositide Regulation of TRP Channels. In Mammalian Transient Receptor Potential (TRP) Cation Channels Handbook of Experimental Pharmacology., B. Nilius and V. Flockerzi, eds. (Springer International Publishing), pp. 1143–1176. https://doi.org/10.1007/978-3-319-05161-1_18.

17. Cao, E., Cordero-Morales, J.F., Liu, B., Qin, F., and Julius, D. (2013). TRPV1 Channels Are Intrinsically Heat Sensitive and Negatively Regulated by Phosphoinositide Lipids. Neuron *77*, 667–679. https://doi.org/10.1016/j.neuron.2012.12.016.

18. Nieto-Posadas, A., Picazo-Juárez, G., Llorente, I., Jara-Oseguera, A., Morales-Lázaro, S., Escalante-Alcalde, D., Islas, L.D., and Rosenbaum, T. (2012). Lysophosphatidic acid directly activates TRPV1 through a C-terminal binding site. Nat. Chem. Biol. *8*, 78–85. https://doi.org/10.1038/nchembio.712.

19. Siemens, J., Zhou, S., Piskorowski, R., Nikai, T., Lumpkin, E.A., Basbaum, A.I., King, D., and Julius, D. (2006). Spider toxins activate the capsaicin receptor to produce inflammatory pain. Nature *444*, 208–212. https://doi.org/10.1038/nature05285.

20. Bohlen, C.J., Priel, A., Zhou, S., King, D., Siemens, J., and Julius, D. (2010). A Bivalent Tarantula Toxin Activates the Capsaicin Receptor, TRPV1, by Targeting the Outer Pore Domain. Cell *141*, 834–845. https://doi.org/10.1016/j.cell.2010.03.052.

21. Liao, M., Cao, E., Julius, D., and Cheng, Y. (2013). Structure of the TRPV1 ion channel determined by electron cryo-microscopy. Nature *504*, 107–112. https://doi.org/10.1038/nature12822.

22. Jordt, S.-E., and Julius, D. (2002). Molecular Basis for Species-Specific Sensitivity to "Hot" Chili Peppers. Cell *108*, 421–430. https://doi.org/10.1016/S0092-8674(02)00637-2.

23. Gavva, N.R., Klionsky, L., Qu, Y., Shi, L., Tamir, R., Edenson, S., Zhang, T.J., Viswanadhan, V.N., Toth, A., Pearce, L.V., et al. (2004). Molecular Determinants of Vanilloid Sensitivity in TRPV1. J. Biol. Chem. *279*, 20283–20295. https://doi.org/10.1074/jbc.M312577200.

24. Chou, M.Z., Mtui, T., Gao, Y.-D., Kohler, M., and Middleton, R.E. (2004). Resiniferatoxin Binds to the Capsaicin Receptor (TRPV1) near the Extracellular Side of the S4 Transmembrane Domain. Biochemistry *43*, 2501–2511. https://doi.org/10.1021/bi035981h.

25. Jordt, S.-E., Tominaga, M., and Julius, D. (2000). Acid potentiation of the capsaicin receptor determined by a key extracellular site. Proc. Natl. Acad. Sci. *97*, 8134–8139. https://doi.org/10.1073/pnas.100129497.

26. Cheng, Y. (2018). Membrane protein structural biology in the era of single particle cryo-EM. Curr. Opin. Struct. Biol. *52*, 58–63. https://doi.org/10.1016/j.sbi.2018.08.008.

27. Cao, E., Liao, M., Cheng, Y., and Julius, D. (2013). TRPV1 structures in distinct conformations reveal activation mechanisms. Nature *504*, 113–118. https://doi.org/10.1038/nature12823.

28. Gao, Y., Cao, E., Julius, D., and Cheng, Y. (2016). TRPV1 structures in nanodiscs reveal mechanisms of ligand and lipid action. Nature *534*, 347–351. https://doi.org/10.1038/nature17964.

29. Zhang, K., Julius, D., and Cheng, Y. (2021). Structural snapshots of TRPV1 reveal mechanism of polymodal functionality. Cell *184*, 5138-5150.e12. https://doi.org/10.1016/j.cell.2021.08.012.

30. Arnold, W.R., Mancino, A., Moss, F.R., Frost, A., Julius, D., and Cheng, Y. (2024). Structural basis of TRPV1 modulation by endogenous bioactive lipids. Nat. Struct. Mol. Biol. https://doi.org/10.1038/s41594-024-01299-2.

31. Ladrón-de-Guevara, E., Dominguez, L., Rangel-Yescas, G.E., Fernández-Velasco, D.A., Torres-Larios, A., Rosenbaum, T., and Islas, L.D. (2020). The Contribution of the Ankyrin Repeat Domain of TRPV1 as a Thermal Module. Biophys. J. *118*, 836–845. https://doi.org/10.1016/j.bpj.2019.10.041.

32. Yao, J., Liu, B., and Qin, F. (2011). Modular thermal sensors in temperature-gated transient receptor potential (TRP) channels. Proc. Natl. Acad. Sci. *108*, 11109–11114. https://doi.org/10.1073/pnas.1105196108.

33. Brauchi, S., Orta, G., Salazar, M., Rosenmann, E., and Latorre, R. (2006). A Hot-Sensing Cold Receptor: C-Terminal Domain Determines Thermosensation in Transient Receptor Potential Channels. J. Neurosci. *26*, 4835–4840. https://doi.org/10.1523/JNEUROSCI.5080-05.2006.

34. Brauchi, S., Orta, G., Mascayano, C., Salazar, M., Raddatz, N., Urbina, H., Rosenmann, E., Gonzalez-Nilo, F., and Latorre, R. (2007). Dissection of the components for PIP $_2$ activation and thermosensation in TRP channels. Proc. Natl. Acad. Sci. *104*, 10246–10251. https://doi.org/10.1073/pnas.0703420104.

35. Vlachová, V., Teisinger, J., Sušánková, K., Lyfenko, A., Ettrich, R., and Vyklický, L. (2003). Functional Role of C-Terminal Cytoplasmic Tail of Rat Vanilloid Receptor 1. J. Neurosci. *23*, 1340–1350. https://doi.org/10.1523/JNEUROSCI.23-04-01340.2003.

36. Grandl, J., Kim, S.E., Uzzell, V., Bursulaya, B., Petrus, M., Bandell, M., and Patapoutian, A. (2010). Temperature-induced opening of TRPV1 ion channel is stabilized by the pore domain. Nat. Neurosci. *13*, 708–714. https://doi.org/10.1038/nn.2552.

37. Kim, S.E., Patapoutian, A., and Grandl, J. (2013). Single Residues in the Outer Pore of TRPV1 and TRPV3 Have Temperature-Dependent Conformations. PLoS ONE *8*, e59593. https://doi.org/10.1371/journal.pone.0059593.

38. Cui, Y., Yang, F., Cao, X., Yarov-Yarovoy, V., Wang, K., and Zheng, J. (2012). Selective disruption of high sensitivity heat activation but not capsaicin activation of TRPV1 channels by pore turret mutations. J. Gen. Physiol. *139*, 273–283. https://doi.org/10.1085/jgp.201110724.

39. Yang, F., Cui, Y., Wang, K., and Zheng, J. (2010). Thermosensitive TRP channel pore turret is part of the temperature activation pathway. Proc. Natl. Acad. Sci. *107*, 7083–7088. https://doi.org/10.1073/pnas.1000357107.

40. Clapham, D.E., and Miller, C. (2011). A thermodynamic framework for understanding temperature sensing by transient receptor potential (TRP) channels. Proc. Natl. Acad. Sci. *108*, 19492–19497. https://doi.org/10.1073/pnas.1117485108.

41. Chowdhury, S., Jarecki, B.W., and Chanda, B. (2014). A Molecular Framework for Temperature-Dependent Gating of Ion Channels. Cell *158*, 1148–1158. https://doi.org/10.1016/j.cell.2014.07.026.

42. Sosa-Pagán, J.O., Iversen, E.S., and Grandl, J. (2017). TRPV1 temperature activation is specifically sensitive to strong decreases in amino acid hydrophobicity. Sci. Rep. *7*, 549. https://doi.org/10.1038/s41598-017-00636-4.

43. Wen, H., and Zheng, W. (2018). Decrypting the Heat Activation Mechanism of TRPV1 Channel by Molecular Dynamics Simulation. Biophys. J. *114*, 40–52. https://doi.org/10.1016/j.bpj.2017.10.034.

44. Kwon, D.H., Zhang, F., Suo, Y., Bouvette, J., Borgnia, M.J., and Lee, S.-Y. (2021). Heat-dependent opening of TRPV1 in the presence of capsaicin. Nat. Struct. Mol. Biol. *28*, 554–563. https://doi.org/10.1038/s41594-021-00616-3.

45. Xiao, T., Sun, M., Zhao, C., and Kang, J. (2023). TRPV1: A promising therapeutic target for skin aging and inflammatory skin diseases. Front. Pharmacol. *14*, 1037925. https://doi.org/10.3389/fphar.2023.1037925.

46. Liao, Z., Umar, M., Huang, X., Qin, L., Xiao, G., Chen, Y., Tong, L., and Chen, D. (2024). Transient receptor potential vanilloid 1: A potential therapeutic target for the treatment of osteoarthritis and rheumatoid arthritis. Cell Prolif. *57*, e13569. https://doi.org/10.1111/cpr.13569.

47. Chen, Y., Mu, J., Zhu, M., Mukherjee, A., and Zhang, H. (2020). Transient Receptor Potential Channels and Inflammatory Bowel Disease. Front. Immunol. *11*, 180. https://doi.org/10.3389/fimmu.2020.00180.

48. Finnerup, N.B., Kuner, R., and Jensen, T.S. (2021). Neuropathic Pain: From Mechanisms to Treatment. Physiol. Rev. *101*, 259–301. https://doi.org/10.1152/physrev.00045.2019.

49. Szallasi, A. (2024). Targeting TRPV1 for Cancer Pain Relief: Can It Work? Cancers *16*, 648. https://doi.org/10.3390/cancers16030648.

50. Judd, D., King, C.R., and Galke, C. (2023). The Opioid Epidemic: A Review of the Contributing Factors, Negative Consequences, and Best Practices. Cureus. https://doi.org/10.7759/cureus.41621.

51. Harbaugh, C.M., and Suwanabol, P.A. (2019). Optimizing Pain Control During the Opioid Epidemic. Surg. Clin. North Am. *99*, 867–883. https://doi.org/10.1016/j.suc.2019.06.002.

52. Basbaum, A.I., and Julius, D. (2006). Toward Better Pain Control. Sci. Am. *294*, 60–67. https://doi.org/10.1038/scientificamerican0606-60.

53. Bamps, D., Vriens, J., De Hoon, J., and Voets, T. (2021). TRP Channel Cooperation for Nociception: Therapeutic Opportunities. Annu. Rev. Pharmacol. Toxicol. *61*, 655–677. https://doi.org/10.1146/annurev-pharmtox-010919-023238.

54. Heiss, J., Iadarola, M., Cantor, F., Oughourli, A., Smith, R., and Mannes, A. (2014). (364) A Phase I study of the intrathecal administration of resiniferatoxin for treating severe refractory pain associated with advanced cancer. J. Pain *15*, S67. https://doi.org/10.1016/j.jpain.2014.01.275.

55. Nadezhdin, K.D., Neuberger, A., Trofimov, Y.A., Krylov, N.A., Sinica, V., Kupko, N., Vlachova, V., Zakharian, E., Efremov, R.G., and Sobolevsky, A.I. (2021). Structural mechanism of heat-induced opening of a temperature-sensitive TRP channel. Nat. Struct. Mol. Biol. *28*, 564–572. https://doi.org/10.1038/s41594-021-00615-4.

56. Mandal, K. (2020). Review of PIP2 in Cellular Signaling, Functions and Diseases. Int. J. Mol. Sci. *21*, 8342. https://doi.org/10.3390/ijms21218342.

57. Gamper, N., and Rohacs, T. (2012). Phosphoinositide Sensitivity of Ion Channels, a Functional Perspective. In Phosphoinositides II: The Diverse Biological Functions Subcellular Biochemistry., T. Balla, M. Wymann, and J. D. York, eds. (Springer Netherlands), pp. 289–333. https://doi.org/10.1007/978-94-007-3015-1_10.

58. Prescott, E.D., and Julius, D. (2003). A Modular PIP $_2$ Binding Site as a Determinant of Capsaicin Receptor Sensitivity. Science *300*, 1284–1288. https://doi.org/10.1126/science.1083646.

59. Stein, A.T., Ufret-Vincenty, C.A., Hua, L., Santana, L.F., and Gordon, S.E. (2006). Phosphoinositide 3-Kinase Binds to TRPV1 and Mediates NGF-stimulated TRPV1 Trafficking to the Plasma Membrane. J. Gen. Physiol. *128*, 509–522. https://doi.org/10.1085/jgp.200609576.

60. Lukacs, V., Thyagarajan, B., Varnai, P., Balla, A., Balla, T., and Rohacs, T. (2007). Dual Regulation of TRPV1 by Phosphoinositides. J. Neurosci. *27*, 7070–7080. https://doi.org/10.1523/JNEUROSCI.1866-07.2007.

61. Poblete, H., Oyarzún, I., Olivero, P., Comer, J., Zuñiga, M., Sepulveda, R.V., Báez-Nieto, D., González Leon, C., González-Nilo, F., and Latorre, R. (2015). Molecular Determinants of Phosphatidylinositol 4,5-Bisphosphate (PI(4,5)P2) Binding to Transient Receptor Potential V1 (TRPV1) Channels. J. Biol. Chem. *290*, 2086–2098. https://doi.org/10.1074/jbc.M114.613620.

62. Kim, D., Cavanaugh, E.J., and Simkin, D. (2008). Inhibition of transient receptor potential A1 channel by phosphatidylinositol-4,5-bisphosphate. Am. J. Physiol.-Cell Physiol. *295*, C92–C99. https://doi.org/10.1152/ajpcell.00023.2008.

63. Lishko, P.V., Procko, E., Jin, X., Phelps, C.B., and Gaudet, R. (2007). The Ankyrin Repeats of TRPV1 Bind Multiple Ligands and Modulate Channel Sensitivity. Neuron *54*, 905–918. https://doi.org/10.1016/j.neuron.2007.05.027.

64. Liu, B., Zhang, C., and Qin, F. (2005). Functional Recovery from Desensitization of Vanilloid Receptor TRPV1 Requires Resynthesis of Phosphatidylinositol 4,5-Bisphosphate. J. Neurosci. *25*, 4835–4843. https://doi.org/10.1523/JNEUROSCI.1296-05.2005.

65. Yao, J., and Qin, F. (2009). Interaction with Phosphoinositides Confers Adaptation onto the TRPV1 Pain Receptor. PLoS Biol. *7*, e1000046. https://doi.org/10.1371/journal.pbio.1000046.

66. Moss, F.R., Lincoff, J., Tucker, M., Mohammed, A., Grabe, M., and Frost, A. (2023). Brominated lipid probes expose structural asymmetries in constricted membranes. Nat. Struct. Mol. Biol. *30*, 167–175. https://doi.org/10.1038/s41594-022-00898-1.

67. Mastronarde, D.N. (2005). Automated electron microscope tomography using robust prediction of specimen movements. J. Struct. Biol. *152*, 36–51. https://doi.org/10.1016/j.jsb.2005.07.007.

68. Zheng, S.Q., Palovcak, E., Armache, J.-P., Verba, K.A., Cheng, Y., and Agard, D.A. (2017). MotionCor2: anisotropic correction of beam-induced motion for improved cryo-electron microscopy. Nat. Methods *14*, 331–332. https://doi.org/10.1038/nmeth.4193.

69. Punjani, A., Rubinstein, J.L., Fleet, D.J., and Brubaker, M.A. (2017). cryoSPARC: algorithms for rapid unsupervised cryo-EM structure determination. Nat. Methods *14*, 290–296. https://doi.org/10.1038/nmeth.4169.

70. Scheres, S.H.W. (2012). RELION: Implementation of a Bayesian approach to cryo-EM structure determination. J. Struct. Biol. *180*, 519–530. https://doi.org/10.1016/j.jsb.2012.09.006.

71. Rosenthal, P.B., and Henderson, R. (2003). Optimal Determination of Particle Orientation, Absolute Hand, and Contrast Loss in Single-particle Electron Cryomicroscopy. J. Mol. Biol. *333*, 721–745. https://doi.org/10.1016/j.jmb.2003.07.013.

72. Arnold, W.R., Asarnow, D., and Cheng, Y. (2022). Classifying liganded states in heterogeneous single-particle cryo-EM datasets. Microscopy *71*, i23–i29. https://doi.org/10.1093/jmicro/dfab044.

73. Liebschner, D., Afonine, P.V., Baker, M.L., Bunkóczi, G., Chen, V.B., Croll, T.I., Hintze, B., Hung, L.-W., Jain, S., McCoy, A.J., et al. (2019). Macromolecular structure determination using X-rays, neutrons and electrons: recent developments in *Phenix*. Acta Crystallogr. Sect. Struct. Biol. *75*, 861–877. https://doi.org/10.1107/S2059798319011471.

74. Pettersen, E.F., Goddard, T.D., Huang, C.C., Couch, G.S., Greenblatt, D.M., Meng, E.C., and Ferrin, T.E. (2004). UCSF Chimera—A visualization system for exploratory research and analysis. J. Comput. Chem. *25*, 1605–1612. https://doi.org/10.1002/jcc.20084.

75. Emsley, P., Lohkamp, B., Scott, W.G., and Cowtan, K. (2010). Features and development of *Coot*. Acta Crystallogr. D Biol. Crystallogr. *66*, 486–501. https://doi.org/10.1107/S0907444910007493.

76. Berman, H., Henrick, K., and Nakamura, H. (2003). Announcing the worldwide Protein Data Bank. Nat. Struct. Mol. Biol. *10*, 980–980. https://doi.org/10.1038/nsb1203-980.

77. Smart, O.S., Neduvelil, J.G., Wang, X., Wallace, B.A., and Sansom, M.S.P. (1996). HOLE: A program for the analysis of the pore dimensions of ion channel structural models. J. Mol. Graph. *14*, 354–360. https://doi.org/10.1016/S0263-7855(97)00009-X.

78. Goddard, T.D., Huang, C.C., Meng, E.C., Pettersen, E.F., Couch, G.S., Morris, J.H., and Ferrin, T.E. (2018). UCSF ChimeraX: Meeting modern challenges in visualization and analysis. Protein Sci. *27*, 14–25. https://doi.org/10.1002/pro.3235.

79. Pettersen, E.F., Goddard, T.D., Huang, C.C., Meng, E.C., Couch, G.S., Croll, T.I., Morris, J.H., and Ferrin, T.E. (2021). UCSF CHIMERAX : Structure visualization for researchers, educators, and developers. Protein Sci. *30*, 70–82. https://doi.org/10.1002/pro.3943.

80. Liedtke, W.B., and Heller, S. eds. (2007). TRP ion channel function in sensory transduction and cellular signaling cascades (CRC/Taylor & Francis).

81. Kalia, J., Milescu, M., Salvatierra, J., Wagner, J., Klint, J.K., King, G.F., Olivera, B.M., and Bosmans, F. (2015). From Foe to Friend: Using Animal Toxins to Investigate Ion Channel Function. J. Mol. Biol. *427*, 158–175. https://doi.org/10.1016/j.jmb.2014.07.027.

82. Bohlen, C.J., and Julius, D. (2012). Receptor-targeting mechanisms of pain-causing toxins: How ow? Toxicon *60*, 254–264. https://doi.org/10.1016/j.toxicon.2012.04.336.

83. Lin King, J.V., Emrick, J.J., Kelly, M.J.S., Herzig, V., King, G.F., Medzihradszky, K.F., and Julius, D. (2019). A Cell-Penetrating Scorpion Toxin Enables Mode-Specific Modulation of TRPA1 and Pain. Cell *178*, 1362-1374.e16. https://doi.org/10.1016/j.cell.2019.07.014.

84. Craik, D.J., Daly, N.L., and Waine, C. (2001). The cystine knot motif in toxins and implications for drug design. Toxicon *39*, 43–60. https://doi.org/10.1016/S0041-0101(00)00160-4.

85. Zhu, S., Darbon, H., Dyason, K., Verdonck, F., and Tytgat, J. (2003). Evolutionary origin of inhibitor cystine knot peptides. FASEB J. *17*, 1765–1767. https://doi.org/10.1096/fj.02-1044fje.

86. Abd El-Aziz, T.M., Soares, A.G., and Stockand, J.D. (2020). Advances in venomics: Modern separation techniques and mass spectrometry. J. Chromatogr. B *1160*, 122352. https://doi.org/10.1016/j.jchromb.2020.122352.

87. Cheng, Y. (2018). Single-particle cryo-EM—How did it get here and where will it go. Science *361*, 876–880. https://doi.org/10.1126/science.aat4346.

88. Wang, F., Liu, Y., Yu, Z., Li, S., Feng, S., Cheng, Y., and Agard, D.A. (2020). General and robust covalently linked graphene oxide affinity grids for high-resolution cryo-EM. Proc. Natl. Acad. Sci. *117*, 24269–24273. https://doi.org/10.1073/pnas.2009707117.

89. Ramlaul, K., Feng, Z., Canavan, C., De Martín Garrido, N., Carreño, D., Crone, M., Jensen, K.E., Li, B., Barnett, H., Riglar, D.T., et al. (2023). A 3D-printed flow-cell for on-grid purification of electron microscopy samples directly from lysate. J. Struct. Biol. *215*, 107999. https://doi.org/10.1016/j.jsb.2023.107999.

90. Meng, P., Huang, H., Wang, G., Yang, S., Lu, Q., Liu, J., Lai, R., and Rong, M. (2016). A Novel Toxin from Haplopelma lividum Selectively Inhibits the NaV1.8 Channel and Possesses Potent Analgesic Efficacy. Toxins *9*, 7. https://doi.org/10.3390/toxins9010007.

91. Zhang, Y.-Y., Huang, Y., He, Q.-Z., Luo, J., Zhu, L., Lu, S.-S., Liu, J.-Y., Huang, P.-F., Zeng, X.-Z., and Liang, S.-P. (2015). Structural and Functional Diversity of Peptide Toxins from Tarantula Haplopelma hainanum (Ornithoctonus hainana) Venom Revealed by Transcriptomic, Peptidomic, and Patch Clamp Approaches. J. Biol. Chem. *290*, 14192–14207. https://doi.org/10.1074/jbc.M114.635458.

92. Meir, A., Simcha Cherki, R., Kolb, E., Langut, Y., and Bajayo, N. (2013). Novel peptides isolated from spider venom, and uses thereof.

93. Xun, C., Wang, L., Yang, H., Xiao, Z., Deng, M., Xu, R., Zhou, X., Chen, P., and Liu, Z. (2021). Origin and Characterization of Extracellular Vesicles Present in the Spider Venom of Ornithoctonus hainana. Toxins *13*, 579. https://doi.org/10.3390/toxins13080579.

94. Chen, J., Zia, A., Luo, A., Meng, H., Wang, F., Hou, J., Cao, R., and Si, D. (2024). Enhancing cryo-EM structure prediction with DeepTracer and AlphaFold2 integration. Brief. Bioinform. *25*, bbae118. https://doi.org/10.1093/bib/bbae118.

95. Jumper, J., Evans, R., Pritzel, A., Green, T., Figurnov, M., Ronneberger, O., Tunyasuvunakool, K., Bates, R., Žídek, A., Potapenko, A., et al. (2021). Highly accurate protein structure prediction with AlphaFold. Nature *596*, 583–589. https://doi.org/10.1038/s41586-021-03819-2.

96. Varadi, M., Bertoni, D., Magana, P., Paramval, U., Pidruchna, I., Radhakrishnan, M., Tsenkov, M., Nair, S., Mirdita, M., Yeo, J., et al. (2024). AlphaFold Protein Structure Database in 2024: providing structure coverage for over 214 million protein sequences. Nucleic Acids Res. *52*, D368–D375. https://doi.org/10.1093/nar/gkad1011.

97. Rushenb (Original Author) and Coxhead, P (Derived Author). Haplopelma lividum, Cobalt blue tarantula cropped. (2016). Wikimedia Commons. Creative Commons Attribution-Share Alike 4.0 International. Accessed July 2024 at: https://commons.wikimedia.org/wiki/File:Haplopelma_lividum,_Cobalt_blue_tarantula_cropp ed.jpg#filelinks

98. Herzig, V., and Hodgson, W.C. (2008). Neurotoxic and insecticidal properties of venom from the Australian theraphosid spider Selenotholus foelschei. NeuroToxicology *29*, 471–475. https://doi.org/10.1016/j.neuro.2008.03.002.

99. Ritchie, T.K., Grinkova, Y.V., Bayburt, T.H., Denisov, I.G., Zolnerciks, J.K., Atkins, W.M., and Sligar, S.G. (2009). Reconstitution of Membrane Proteins in Phospholipid Bilayer Nanodiscs. In Methods in Enzymology (Elsevier), pp. 211–231. https://doi.org/10.1016/S0076-6879(09)64011-8.

100. Bepler, T., Morin, A., Rapp, M., Brasch, J., Shapiro, L., Noble, A.J., and Berger, B. (2019). Positive-unlabeled convolutional neural networks for particle picking in cryo-electron micrographs. Nat. Methods *16*, 1153–1160. https://doi.org/10.1038/s41592-019-0575-8.

101. He, J., Li, T., and Huang, S.-Y. (2023). Improvement of cryo-EM maps by simultaneous local and non-local deep learning. Nat. Commun. *14*, 3217. https://doi.org/10.1038/s41467-023-39031-1.

102. Clauser, K.R., Baker, P., and Burlingame, A.L. (1999). Role of Accurate Mass Measurement (±10 ppm) in Protein Identification Strategies Employing MS or MS/MS and Database Searching. Anal. Chem. *71*, 2871–2882. https://doi.org/10.1021/ac9810516.

Publishing Agreement

It is the policy of the University to encourage open access and broad distribution of all theses, dissertations, and manuscripts. The Graduate Division will facilitate the distribution of UCSF theses, dissertations, and manuscripts to the UCSF Library for open access and distribution. UCSF will make such theses, dissertations, and manuscripts accessible to the public and will take reasonable steps to preserve these works in perpetuity.

I hereby grant the non-exclusive, perpetual right to The Regents of the University of California to reproduce, publicly display, distribute, preserve, and publish copies of my thesis, dissertation, or manuscript in any form or media, now existing or later derived, including access online for teaching, research, and public service purposes.

        Author Signature

8/12/2024

        Date